SPECTRAL-TEMPORAL CORRELATIONS IN THE X-RAY EMISSION OF CYGNUS X-1

DIPLOMA THESIS OF
MORITZ BÖCK

SUPERVISOR:
PROF. DR. JÖRN WILMS

OCTOBER, 2008

PERFORMED AT THE
DR. KARL REMEIS-STERNWARTE BAMBERG

The cover picture is an artist's impression of the black hole Cygnus X-1 and its companion star. Stellar wind from the supergiant is pulled toward the black hole and forms an extremly hot disk around it.

Spectral-Temporal Correlations in the X-ray Emission of Cygnus X-1

Diploma Thesis of
Moritz Böck

October, 2008

Supervisor:
Prof. Dr. Jörn Wilms

performed at the
Dr. Karl Remeis-Sternwarte Bamberg
(Astronomical Institute of the University of Erlangen-Nuremberg)
Sternwartstr. 7,   96049 Bamberg

Erweiterte deutsche Zusammenfassung

Moritz Böck

Spektrale und zeitliche Korrelationen in der Röntgenemission von Cygnus X-1

In dieser Arbeit wird die Röntgenstrahlung des Galaktischen Schwarzen Lochs Cygnus X-1 analysiert. Da gemäß der Definition eines Schwarzen Lochs keine Informationen aus seinem Inneren nach außen gelangen können, können Schwarze Löcher nicht direkt beobachtet werden. Aufgrund ihrer großen Masse und ihrer enormen Dichte haben sie jedoch einen starken Einluss auf ihre Umgebung. Befindet sich Materie in ihrer Nähe, welche angezogen werden kann, so können sie zu den hellsten Objekten im Universum werden.

Cygnus X-1 bildet zusammen mit seinem Begleitstern ein Röntgen-Doppelsystem. Das Schwarze Loch akkretiert Materie seines Begleitsterns, insbesondere dessen Sternwind. Diese erhitzt sich dabei so stark, dass unter anderem Röntgenstrahlung emittiert wird. Es hat sich gezeigt, dass solche Systeme verschiedene Emissionszustände annehmen können und dass auch Übergänge zwischen diesen Zuständen möglich sind. Die charakteristischen Eigenschaften dieser Zustände deuten darauf hin, dass die Emission von Energie auf einem komplizierten Zusammenspiel verschiedener Prozesse beruht. Neben thermischer Strahlung der Akkretionsscheibe tragen nach aktuellem Wissensstand auch weitere Mechanismen, wie Comptonisierung und Synchrotronstrahlung eines relativistischen Jets, zur Emission dieser Quelle bei.

Basierend auf Röntgen- und Radio-Daten von Cygnus X-1, die 10 Tage im Februar 2005 abdecken, wird das Verhalten dieser Quelle untersucht. Die Daten wurden mit dem Rossi X-ray Timing Explorer (*RXTE*), einem Röntgen Satelliten, und dem Ryle Radio Teleskop gemessen.

Zunächst werden in dieser Arbeit Röntgen-Doppelsysteme, ihre Eigenschaften und typischen Zustände, sowie grundlegende Emissionsprozesse erläutert. Anschließend wird dargelegt, wie die erhaltenen Daten analysiert werden können. Dabei werden *RXTE* und das Ryle Teleskop näher beschrieben.

Die spektrale Analyse der Daten ist ein bedeutender Teil der Arbeit. In Kapitel 4 werden die Methoden und Ergebnisse präsentiert. Es zeigte sich, dass innerhalb des untersuchten Zeitraums ein Übergang zwischen zwei spektralen Zuständen stattfand. Nach dem Übergang wurden deutlich mehr weiche Röntgenstrahlen emittiert als zuvor und das Spektrum wurde deutlich weicher. Aus diesem Grund werden diese beiden Zustände als "hard" und "soft state" bezeichnet. Um weitere Veränderungen der Spektren herauszufinden, wurden diese mit verschieden Modellen gefittet, und zwar mit einem phänomenologischen Potenzgesetz mit exponentiellem Abbruch, einem Comptonisierungsmodell, welches die Hochstreuung von thermischen Photonen aus der Akkretionsscheibe durch inverse Comptonstreuung beschreibt, sowie einem Jet-Modell bei dem auch Synchrotronstrahlung berücksichtigt wird. Das Verhalten der Parameter stimmt mit dem überein, welches im Rahmen einer Untersuchung des Langzeitverhaltens von Cygnus X-1 zwischen 1999 und 2004 gefunden wurde.

In Kapitel 5 wird die zeitliche Analyse der Daten zusammengefasst. Die Röntgenstrahlung der Quelle wurde mit Fouriermethoden untersucht, um die Variabilität auf Zeitskalen zwischen Millisekunden und Stunden zu charakterisieren. Die spektral Leistungsdichte wurde in dieser Arbeit in einem Energieband von 4.5–5.8 keV, sowie in einem Band von 9.5–15 keV berechnet. Dabei fielen zwei Komponenten auf, welche jeweils mit einer breiten Lorentz-Kurve modelliert werden können. Es zeigte sich eine Abhängigkeit der Peak-Frequenzen von spektralen Parametern. Die Peak-Frequenzen sind in beiden Energiebändern identisch, jedoch ist die Lorentzkomponente bei kleineren Frequenzen im hohen Energieband deutlich schwächer ausgeprägt, während die zweite unverändert bleibt. Dies deutet darauf hin, dass die entsprechenden Frequenzen durch verschiedene Prozesse erzeugt werden, oder zumindest aus verschiedenen Regionen stammen. Eine mögliche Ursache für diese Frequenzen ist die Akkretionsscheibe. Bereits die zeitliche Variation der Emission in beiden Energiebändern selbst zeigt interessante Eigenschaften. Es gibt eine starke lineare Korrela-

tion der Bänder, sowie eine Zeitverzögerung von mehreren Millisekunden von Ereignissen im hohen Energieband gegenüber den entsprechenden im niedrigen Energieband. Auch die Zeitverzögerung hängt von spektralen Parametern ab und zeigt ein charakteristisches Verhalten.

Die Kombination von spektraler und zeitlicher Analyse der Röntgenemission ist von wesentlicher Bedeutung, um zu ergründen welche physikalische Prozesse diese Emission verursachen. Es wurden bisher noch keine Modelle gefunden, die die Funktionsweise von Röntgen-Doppelsysteme detaillert beschreiben und dabei mit allen beobachteten spektralen und zeitlichen Eigenschaften vereinbar sind.

Extended Abstract

Moritz Böck

Spectral-Temporal Correlations in the X-ray Emission of Cygnus X-1

In this work the X-ray emission of the galactic black hole Cygnus X-1 is analyzed. As no information of the interior of a black hole can reach the outside by definition, they cannot be observed directly. Due to their high mass and enormous density, they have strong influence on their surrounding. If matter, which can be gravitationally attracted, is located in their vicinity, they can become the brightest objects in the universe.

Together with its companion star Cygnus X-1 forms an X-ray binary. The black hole accrets matter from its companion, in particular the stellar wind. Thereby the matter heats up such that X-rays are emitted among other things. It turned out that these systems can obtain different emission states and that transitions between the states are possible. The characteristic properties of these states indicate that the emission of energy is based on a complicated interaction of different processes. According to the current standard of knowledge, besides thermal radiation of the accretion disk other mechanisms, such as Comptonization and synchrotron radiation of a relativistic jet, contribute to the emission of the source.

Based on X-ray and radio data of Cygnus X-1, which cover 10 days in February 2005, the behavior of this source is analyzed. The data were obtained with an X-ray satellite, the Rossi X-ray Timing Explorer (*RXTE*), and the Ryle Telescope.

At first X-ray binaries, their properties and typical states, as well as the essential emission processes are explained in this work. Afterwards it is expounded how the obtained data can be analyzed. At the same time *RXTE* and the Ryle Telescope are described in detail.

The spectral analysis of the data is an important part of this work. In Chapter 4 the methods and results are presented. It turned out that a transition between two spectral states occurred during the analyzed period of time. After the transition significantly more soft X-rays were emitted than before and the spectrum became much softer. For that reason these states are called hard and soft state. In order to figure out further changes of the spectra, they were fitted with different models, namely a phenomenological power law with exponential cutoff, a Comptonization model, which describes the up-scattering of thermal photons from the accretion disk by inverse Compton scattering, and a jet model taking synchrotron radiation into account. The behavior of the parameters coincides with that, which was found in the scope of a long-term analysis of the behavior of Cygnus X-1 between 1999 and 2004.

In Chapter 5 the timing analysis of the data is summarized. The X-ray emission of the source was investigated with Fourier methods in order to characterize the variability in time scales between milliseconds and hours. In this work the power spectral density was computed in an energy band from 4.5–5.8 keV and in one from 9.5–15 keV. Two components attracted attention, each of them can be modelled with a broad Lorentzian profile. A dependence of the peak frequencies on the spectral parameters was found. The peak frequencies are identical in both energy bands, but the Lorentzian at lower frequencies is significantly less marked in the high energy band, whereas the second one remains constant. This indicates that the corresponding frequencies are caused

by different processes, or at least originate from different regions. A possible reason for these frequencies is the accretion disk. Already the temporal variation of the emission in both energy bands itself shows interesting properties. There is a strong linear correlation between both bands, as well as a time lag of several milliseconds of events in the high energy band to the corresponding ones in the low energy band. Also the time lag depends on spectral parameters and shows a characteristic behavior.

The combination of spectral and timing analysis of the X-ray emission is essential to figure out the physical processes causing the emission. Up to now no models have been found, which describe the radiation of X-ray binaries in detail and are consistent with all observed spectral and temporal properties at the same time.

Contents

Chapter 1

Introduction

Astronomy is one of the oldest sciences. Already several thousand years ago humans observed objects on the sky, analyzed their behavior, searched for explanations and made use of these phenomena. For example the exact determination of time and date was based on astronomical observations of the Sun, stars and the Moon. This could be done due to the fact that characteristic time scales on Earth, such as days and years, but also other effects like the tides, are caused by a periodic and thus more or less easily predictable movements of Earth, Sun and Moon.

The same principle of observing, analyzing and finding models holds also for modern astronomy. Of course the means of observations and analyses are now on a completely different level, also is the increasing basis of knowledge. Today there are very complicated models, which describe even more complicated processes in the universe. In this work an object with very interesting properties is investigated. It is an X-ray source, namely a black hole in an X-ray binary. Its name is Cygnus X-1. The analysis follows the classical astronomical way, i.e., observing the object, analyzing the data and giving explanations for the observed properties. Each step is described in detail in this work. But at first the basis information is introduced. In this section the history of radio and X-ray astronomy is summarized briefly and it is explained what black holes are.

1.1 Radio and X-ray Astronomy

The progress in astronomy was tied to the means of observation. The usage of telescopes was an enormous improvement compared to watching the sky with the naked eye. But a real breakthrough in astrophysics came in the 20th century when it became possible to detect cosmic radiation and to observe the sky in other wave bands. In those bands the sky looks quite different than in the optical. The history of radio and X-ray astronomy will be described briefly in the following, as data in these bands are used in this work.

The emission of radio waves and further electromagnetic radiation with wavelengths different to the optical by stellar objects was already predicted in the end of the 19th century. Radio astronomy started with the first measurement of cosmic radio waves by Karl Jansky in 1933[1] (Janksy, 1933). He worked for the Bell Telephone Laboratories and investigated sources which could disturb a planned transatlantic radio telephone service. For that purposed he constructed a radio antenna detecting radio waves with a wavelength of 14.5 m and recorded signals from all directions for several months. His analysis revealed that besides thunderstorms there was a sources with a periodic modulation of a day. At first Jansky thought that this radiation originated from the sun, but after some months the position of this sourced differed from that of the sun, also the exact period was 23 hours and 56 minutes, a sidereal day. The radiation came from the Milky Way with a maximum from the direction of the galactic center. The measurement of extragalactic

---

[1] `http://www.nrao.edu/whatisra/hist_jansky.shtml`

radio waves arouse interest for radio astronomy and since then numerous radio telescopes have been built. Further information on radio telescopes is given in Sect. 3.1.

X-rays cannot be observed from the ground as the Earth's atmosphere is opaque for this radiation (see Sect. 3.2). Thus X-ray astronomy started when X-ray detectors could be carried in sufficiently high altitudes. This could be done by balloons, rockets and later satellites.

Golian et al. (1946) measured cosmic X-rays with a detector aboard a V-2 rocket. The Sun turned out to be a very bright X-ray source. Its X-ray emission allowed to estimate how much X-rays from other stars could be detected at the Earth. The values were much too small to be measured with the detectors, therefore the interest for further X-ray missions was not very large. This changed in 1962 when Giacconi et al. tried to the measure X-rays originating from the moon, but detected an X-ray source in the Scorpius constellation, which was then called Scorpius X-1. It took some time to find explanations for the nature of this source. Accretion of matter onto a compact object, such as a neutron star was a solution, which was accepted commonly. The processes causing this radiation are discussed in detail in Sect. 2.

In 1970 the *UHURU* satellite was launched and it detected more than 400 other X-ray sources, which were then cataloged. Up to now numerous X-ray satellites were orbiting the Earth allowing to monitor the sources and finding new ones. At the moment several X-ray satellites are in use and there are some upcoming missions. The Rossi X-ray Timing Explorer (*RXTE*), a satellite performing since 1998 with which the X-ray data analyzed in this work were obtained, is described in detail in Sect. 3.2.

1.2 Black Holes

Black Holes (BHs) are fascinating objects for many people, from scientist analyzing them up to laymans without much physical knowledge. The reason is that the principle of a black hole is quite easy to understand on the one hand, but on the other hand one cannot figure out details of the interior of the black hole by definition. For that reason there are several theories and speculations to what happens inside a black hole. Of course only a few of them are physically reasonable.

By definition a black hole is simply a mass within a certain volume, such that its escape velocity is greater than or equal to the speed of light. As no information can be transmitted faster than light no information can leave this volume. In principle an object of arbitrary mass can become a black hole if it is compressed strongly enough. If matter of mass M is located within a sphere with radius R_S around its center of mass no information can leave the sphere. The surface of the sphere is therefore called event horizon, its radius is given by

$$R_\mathrm{S}(M) = \frac{2GM}{c^2} \approx 3\,\mathrm{km}\,\frac{M}{M_\odot} \tag{1.1}$$

where $c = 2.99792 \cdot 10^8\,\mathrm{m/s}$ is the speed of light, $G = 6.673 \cdot 10^{-11}\,\mathrm{m^3kg^{-1}s^{-2}}$ is the gravitational constant and $M_\odot = 1.9891 \cdot 10^{30}\,\mathrm{kg}$ is the solar mass. The simple idea of the escape velocity is however a bit misleading, as the propagation of photons cannot be compared with the ballistic motion of a classical particle, which is launched from an object with a certain velocity, slowed down and falls back onto the object if the velocity was smaller than the escape velocity. Using General Relativity it can be shown that a photon cannot cross the event horizon from the inside. This can be seen considering the Schwarzschild metric. The radius R_S is called Schwarzschild radius named after the astronomer Karl Schwarzschild. He derived the radius of the event horizon of a non-rotating black hole by solving Einstein's field equations of General Relativity. In polar coordinates the metric in flat spacetime is given by

$$(ds)^2 = (c\,dt)^2 - (dr)^2 - (r\,d\theta)^2 - (r\,\sin\theta\,d\phi)^2 \tag{1.2}$$

According to General relativity spacetime is curved by mass. In the simplest case of spherical symmetry the spacetime around a massive object is described by the Schwarzschild metric[2]

$$(ds)^2 = \left(c\,dt\sqrt{1-\frac{2GM}{Rc^2}}\right)^2 - \left(\frac{dr}{\sqrt{1-\frac{2GM}{Rc^2}}}\right)^2 - (r\,d\theta)^2 - (r\,\sin\theta\,d\phi)^2 \tag{1.3}$$

Using $ds = 0$, which holds for light, one obtains the coordinate speed of radially propagating light $(d\phi = d\theta = 0)$

$$\frac{dr}{dt} = c\left(1-\frac{2GM}{Rc^2}\right) = c\left(1-\frac{R_\mathrm{S}}{R}\right) \tag{1.4}$$

The speed of light has to be constant in every inertial system, its apparent speed seems to "freeze" at the event horizon for a distant observer. It can be understood that this is consistent by considering the proper time τ. For events occuring at the same position it holds

$$d\tau = \frac{ds}{c} = dt\sqrt{1-\frac{R_\mathrm{S}}{R}} \tag{1.5}$$

For $R < R_\mathrm{S}$ the following unequation holds

$$(c\,dt)^2\left(1-\frac{R_\mathrm{S}}{R}\right) < 0 \tag{1.6}$$

A particle is not allowed to rest $(dr = d\phi = d\theta = 0)$ behind the event horizon $(R < R_\mathrm{S})$, as $(ds)^2$ would be smaller than 0 in this case and thus spacelike. For that reason even photons have to move toward the center $R = 0$, where the true singularity of the metric is located.

Using the effective potential the radius of the innermost stable circular orbit (ISCO) can be derived (Shapiro & Teukolsky, 1983). For a Schwarzschild black hole one obtains $R_\mathrm{ISCO} = 3R_\mathrm{S}$. For rotating black holes this value is different. Up to now non-rotating black holes were discussed. Particles, which fall into the black hole, keep their angular momentum thus one expects rotating black holes. They are called Kerr black holes. The angular momentum J can be characterized by the dimensionless Kerr parameter a, which is defined via

$$a = \frac{cJ}{GM^2} \tag{1.7}$$

For a Schwarzschild black hole a is equal to zero and is 1 for a maximally rotating black hole. Thorne (1974) showed that upper limit of a is not 1 but 0.998. Calculations show that the singularity at $R = 0$ changes into a ring singularity $(R > 0)$. For a maximally rotating black hole the radius of the singularity would be identical to the radius of the event horizon.

A black hole can be characterized by its mass and its angular momentum. In principle it can be electrically charged in addition. But as a charged black hole would attract particles of opposite charge by preference, there are no significantly charged black holes expected. The most important characteristic is the black hole's mass M. As the Schwarzschild radius scales linearly with M the density of black hole decreases strongly with increasing mass. In general the behavior of black holes of different masses is very similar. The properties of the accretion mechnisms and the resulting emission of energy, which are discussed in Ch. 2, scale with the mass, but are assumed to be identical in principle. As distance scales linearly with M also the time scale does. The variabilty of black holes with several solar masses can be observed and analyzed in time scales which are suitable for humans.

There are stellar-mass black holes with a few solar masses. These objects are the compact remnants of heavy stars. The way they form can be described by stellar evolution. The gas

---

[2] It is only valid outside of matter, i.e., in the vacuum.

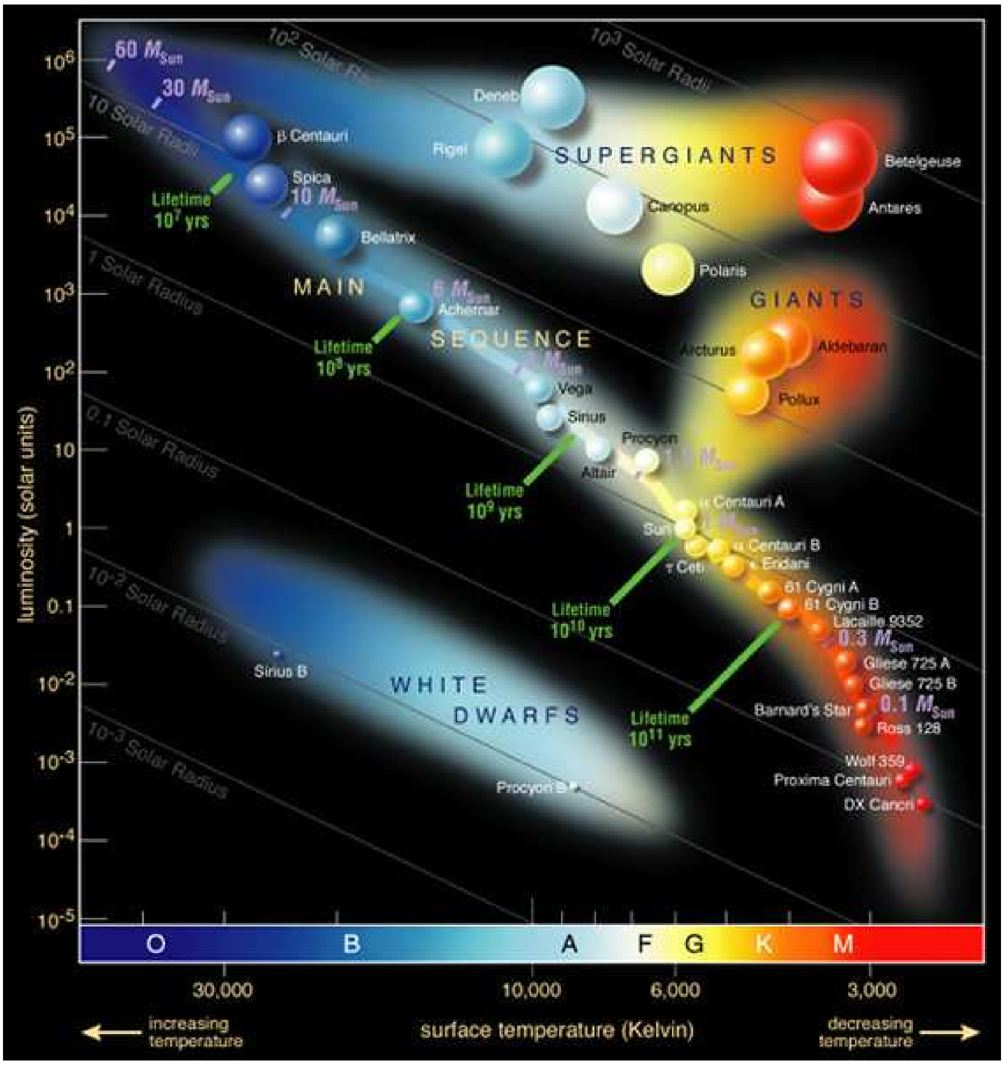

Figure 1.1: A Hertzsprung-Russell diagram shows the relation between the luminosity and the spectral type of stars. The spectral type of a star is given by its color and thus by its temperature.

pressure in a star counterbalances its gravitational force. Depending on the star's mass it will end up as a white dwarf, a neutron star or a black hole. Low and intermediate mass stars (up to $8\,M_\odot$) evolve to white dwarfs (Iben & Renzini, 1983). The mass of stars on the main sequence increases approximately with their luminosity, as it can be seen in Fig. 1.1. After the star burned its fuel, the gas pressure, which was caused by the temperature of nuclear fusion decreases and the star contracts until the electron degeneracy pressure balances gravity. The typical size of white dwarfs is comparable to that of the Earth ($R_\oplus \approx 6\,370\,\mathrm{km}$). Above a certain mass, the Chandrasekhar limit (Chandrasekhar, 1931), which is about $1.4\,M_\odot$, the degeneracy pressure is not sufficient to counterbalance the gravitational force. If the white dwarf's mass exceeds this value, for example by accreting matter from a companion star, it collapses into a neutron star, which is even smaller and denser than the white dwarf. It is prevented to collapse further by the neutron degeneracy pressure. The size of a neutron star is about 10–20 km. If its mass exceeds the Tolman-Oppenheimer-Volkoff limit of about 3 solar masses, there is no known pressure to counterbalance gravity. In this case it is assumed that the matter collapses into a singularity and a black hole is formed. Massive stars end their life with an explosion, while their core collapses directly into a neutron star or black hole. See Heger et al. (2003) for more details.

Besides these black holes there are supermassive black holes. They can have masses from $10^5\ M_\odot$

to $10^9\,M_\odot$ and are located in the center of galaxies. The mass of the black hole, which is centered in our Milky Way Galaxy, was determined to be $M = (4.8 \pm 0.3) \cdot 10^6\,M_\odot$ (Ghez et al., 2008). This can be done by analyzing trajectories of stars in the center of our galaxy. In certain galaxies the black holes can be observed in a different way, namely for Active Galactic Nuclei (AGN). Here, the supermassive black hole is active, it attracts matter in its vicinity. Before the matter falls into the black hole enormous amounts of energy can be emitted, as it is explained in Sect. 2.2. This process leads to very large luminosities. The brightest objects in the universe, the quasars, are assumed to be AGN, as there are no other explanations for the observed spectra and the energy density. As stellar-mass black holes, which are provided with matter from their vicinity, show a similar behavior on smaller scales, they are called microquasars.

1.3 Thesis Outline

In this work the X-ray emission of the source Cygnus X-1 is analyzed. Spectral-temporal correlations in this emission are presented and interpreted. In addition simultaneously obtained radio data are taken into account.

The structure of this work is the following. In Sect. 2 the nature of X-ray binaries is explained. Accretion and further processes which are supposed to be the underlying mechanisms causing the X-ray emission are discussed. Soft X-rays are a large fraction of the thermal black body radiation of the accretion disk. The Comptonization process is presented, which is an explanation for the hard X-rays. An alternative or addition to a Comptonizing corona is a jet. The different emission states of black hole binaries and the source Cyg X-1 are introduced.

Sect. 3 is about the data. It is discussed how radio waves and X-rays from a celestial source can be detected. Thus radio telescopes and an X-ray satellite, namely the Rossi X-ray Timing Explorer are presented, also are the data which used in this work.

The method of the spectral analysis of this data and the results are treated in Sect. 4. Different models are applied to fit the spectra of Cyg X-1 in order to figure out how the emission changes with time. Parameters obtained from the fits are compared with that of a long-term monitoring of Cyg X-1.

After that the timing analysis of the data is discussed (Sect. 5). In doing so the expected frequencies in the emission of X-ray binaries are explained, a detailed description of finding quasi-periodic modulations in the data by Fourier analysis is given and the results are presented. This is done in two different energy bands. To compare both energy bands two important values are introduced, namely the coherence and the time lag. Possible processes are explained, which could cause the observed timing properties.

To conclude the work the most important results are summarized in Sect. 6.1 and an outlook is given, in which planned subsequent analysis and expected results are outlined.

Chapter 2

X-Ray Binaries

In this chapter the nature of X-ray binaries is described. At first it is explained how accretion, which leads to the emission of energy, is possible in binaries. The emission differs between different sources, but also the spectrum of a single source can change with time. The characteristic spectral properties allow a classification into states, which are described in Sect. 2.4. Afterwards Cygnus X-1, the source which is analyzed in this work, is introduced and its basic properties are summarized. Finally the essential processes leading to a emission of energy from such a system are explained.

2.1 Binaries

A large number of stars are part of multiple systems, in which two or more stars orbit around a common center of mass. Binaries consisting of stars can be observed in different ways. There are visual binaries, whose components can be resolved separately with telescopes. If the orbital period is not too long, their motion can be observed directly. Spectroscopic binaries cannot be resolved as different stars, but their spectra are found to be the sum of two independent stellar spectra. Depending on the inclination of the system, which is the angle between the line of sight and a perpendicular to the orbital plane, other effects can be observed. If the inclination is sufficiently close to 90° eclipses can be observed. In this case a star passes the line of sight periodically in front of the other. If the inclination differs from 0° periodic modulations of the spectral lines, due to the Doppler effect, can be observed. The projected radial velocity of a star can be obtained by measuring the shifts of its spectral lines. Doing so is relevant to determine the mass of the binary components. If the orbit has a small eccentricity[1] and the velocities of both stars can be determined their mass ratio is simply given by:

$$\frac{M_1}{M_2} = \frac{v_2}{v_1} = \frac{v_{r,2}}{v_{r,1}} \tag{2.1}$$

where $v_r = v \sin i$ is the projected radial velocity and i the inclination. To determine the sum of the masses, the inclination must be known. Substituting the distance a between both objects

$$a = \frac{P}{2\pi}(v_1 + v_2) \tag{2.2}$$

where P is the orbital period, into Kepler's third law

$$\frac{P^2}{a^3} = \frac{4\pi^2}{G(M_1 + M_2)} \tag{2.3}$$

one obtains

$$M_1 + M_2 = \frac{P}{2\pi G} \frac{(v_{r,1} + v_{r,2})^3}{\sin^3 i} \tag{2.4}$$

---

[1] For a small eccentricities one can assume that the Keplerian velocities are constant.

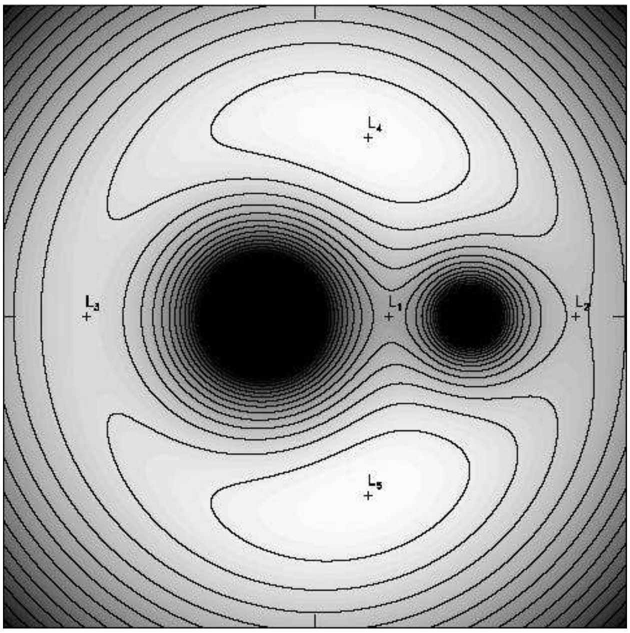

Figure 2.1: Visualization of the effective gravitational potential $\Phi(\vec{r})$ in the orbital plane. The Lagrangian points $\{L_1, ..., L_5\}$ are the positions, where $d\Phi(\vec{r})/d\vec{r} = 0$ (R. Hynes, priv. comm.)

If the radial velocity of only one component can be determined accurately, as it is of course the case if the other component is a neutron star or a black hole, Eq. 2.1 can be substituted into Eq. 2.4

$$\frac{P}{2\pi G}\, v_{r,1}^3 = \frac{M_2^3}{(M_1 + M_2)^2} \sin^3 i \tag{2.5}$$

The value on the left-hand side, which depends only on quantities which can be measured directly, is called mass function. If the mass of the star with the known radial velocity is estimated[2], the mass of the second object in the binary depends only on the inclination. It is very complicated to determine the masses with this method in binaries with eccentric orbits.

In close binaries there can be mass exchange. It can be understood more easily by considering an effective gravitational potential in a co-rotating coordinate system, whose origin is the center of mass of the system. This potential consists of the gravitational potential of both components of the binary and a centrifugal potential. It is given by

$$\Phi(\vec{r}) = -\frac{GM_1}{\|\vec{r} - \vec{r_1}\|} - \frac{GM_2}{\|\vec{r} - \vec{r_2}\|} - \frac{1}{2}(\vec{\omega} \times \vec{r})^2 \tag{2.6}$$

where $\vec{r_1}$, $\vec{r_2}$ are the positions of the components and the angular frequency is

$$\|\vec{\omega}\| = \sqrt{\frac{G(M_1 + M_2)}{(\|\vec{r_1} - \vec{r_2}\|)^3}} \tag{2.7}$$

There are points in this system, where no forces act. Five solutions of $d\Phi(\vec{r})/d\vec{r} = 0$ exist, which are called Lagrangian points L_i. One of these points is located between the components of the binary, the inner Lagrangian point L_1. The equipotential surface including L_1 is called Roche lobe. It is shaped like two drops which are connected with their vertices. Matter can easily be exchanged over the inner Lagrangian point, especially if one component of the binary almost fills its part of the Roche lobe.

---

[2] The mass of stars can be estimated using relations between the mass and other parameters of a star, such as luminosity. These relations were found within the analysis of a large number of binaries.

2.2 Accretion

In astrophysics accretion is the name for the process of growing by attracting matter, where the attractive force is gravity. If matter is accreted by compact objects energy is released. The emission of the energy can be measured. Due to accretion black holes can become extremely bright. The reason is that particles do not fall into the black hole directly, but due to the conservation of angular momentum they have to orbit the black hole. Thereby they interact with other particles, heat up due friction forces, transfer angular momentum, or lose it by emission of energy, thus the particles spiral inwards. If matter is accreted onto neutron stars there is also energy emitted at its impact on the neutron star's surface.

An useful value to quantify the luminosity of an accreting object is its Eddington luminosity L_{Edd}. It is defined as the luminosity at which the radiation pressure balances the gravitational force. For its calculation it is assumed that there is a spherically symmetric accretion of fully ionized hydrogen. The gravitational force acting on the protons is

$$F_{\mathrm{g}} = \frac{MGm_{\mathrm{p}}}{r^2} \tag{2.8}$$

The same force is assumed to act on the electrons, as they are attracted by the protons due to the Coulomb force and many particles are considered. The radiation force acting outwards is given by

$$F_{\mathrm{rad}} = \frac{\sigma_{\mathrm{T}} S}{c} \quad \text{with the energy flux} \quad S = \frac{L}{4\pi r^2} \tag{2.9}$$

where L is the luminosity. The Thomson cross section is proportional to m^{-2} and thus only important for the electrons, but again it is assumed that the same radiation force acts on the protons due to Coulomb coupling. In order to maintain accretion F_{g} must be larger than F_{rad}. Thus the Eddington luminosity is defined by

$$L < \frac{4\pi G M m_{\mathrm{p}} c}{\sigma_{\mathrm{T}}} \approx 1.3 \cdot 10^{38} \mathrm{erg\,s^{-1}} \cdot \frac{M}{M_{\odot}} \equiv L_{\mathrm{Edd}} \tag{2.10}$$

To get an idea of the enormous luminosty resulting from accretion, it is helpful to consider nuclear fusion. This is already a very efficient process. The fusion of hydrogen to helium converts about 0.7% of the rest mass of each proton into released energy. The accretion of matter by a Schwarzschild black hole can release up to about 10% of the rest mass of the matter (Frank et al., 1992). For Kerr black holes this fraction increases even to 30–40%.

Matter which is accreted by a compact object has to originate from somewhere. Significant accretion can be observed in binaries consisting of a star and a compact object. Here the star can provide its companion with matter. There are different mass exchange mechanisms. The first one was already introduced above, the so-called Roche lobe overflow. If the star fills its Roche lobe, for example in the evolution of a star its radius increases, matter can flow over the inner Lagrangian point easily. Another process is wind accretion. If the star has a sufficiently strong stellar wind, as it is the case for early type and massive stars, a part of the wind can be accreted by the compact object. Depending on parameters of the system the accreted fraction is typically 0.01–0.1% (Frank et al., 1992). Mass loss rates of OB type stars[3] can be in the range of 10^{-6}–$10^{-5}\,M_{\odot}\,\mathrm{y}^{-1}$. The accreted fraction of such a wind can be enough that the emission of the compact object is close to the Eddington limit. It is worth noting a third mechanism, which is even more tied to the type of the companion star, the so-called Be-mechanism. It is only possible with Be stars, this are special spectral type B stars which can have a disk extending to several solar radii around them. The disk is located in the star's equatorial plane. If the orbit of the compact object crosses the disk there are phases with a strong accretion, leading to outbursts.

---

[3] A Hertzsprung-Russell diagram, illustrating the basic star classification. It was shown in Fig. 1.1.

As a large fraction of the emission, resulting from accretion by a compact object, are X-rays, such binaries are called X-ray binaries and microquasars. They are classified into Low Mass X-ray Binaries (LMXBs) and High Mass X-ray Binaries (HMXBs), according to the mass of the star. The stellar wind in LMXBs is to usually too weak for wind accretion. The dominant accretion process in these systems is Roche lobe overflow. LMXBs are relatively old systems, as stars of low mass have a quite long lifetime and thus their evolution to large radii takes some time. It is contrary for HMXBs, as heavy stars of spectral type O or B with strong winds have a much short lifetimes.

2.3 Radiation Processes

The spectra of X-ray binaries have characteristic shapes. There are several models describing the components which are found in the spectra. The components are discussed in the following.

2.3.1 Black Body Radiation

The emission of electromagnetic radiation of black body with temperature T is characterized by Plank's law (Rybicki & Lightman, 1979, Eq. 1.51)

$$I(\nu, T) = \frac{2h\nu^3}{c^2} \frac{1}{e^{\frac{h\nu}{k_\mathrm{B}T}} - 1} \tag{2.11}$$

it yields the intensity of the emission of electromagnetic waves with frequency ν per solid angle, per emitting surface and per frequency. In order to obtain the total luminosity of a black body it is necessary to integrate Eq. 2.11 over these quantities. The spectrum of stars can be described with such a black body spectrum.

For an accretion disk it is different, as the temperature profile of the disk is not constant. It was shown that the temperature T of accretion disks depends on the radius R Shakura & Syunyaev (1973); Pringle (1981)

$$T(R) \propto R^{-\frac{3}{4}} \tag{2.12}$$

There is a black body emission at a radius R with a temperature $T(R)$. The total emission of the accretion disk is thus the sum of black body components of different temperature. The total spectrum can be described as a stretched black body spectrum. The disk is therefore called a multi-color disk.

2.3.2 Broadened Iron Line

An important component of the spectra of X-ray binaries is the iron line. It is the Kα emission line, caused by the transition of an electron from the L shell (2p orbital) to the K shell (1s orbital). The transition energy is about 6.4 keV, it increases for strongly ionized iron. This fluorescent line is an important tool in the analysis of black holes. It originates from the vicinity of the black hole and is shape is influenced by several parameters of the system, such as the inclination of the accretion disk, the accretion geometry and the spin of the black hole. A detailed analysis of the iron line's shape allows in principle to determine the values of these parameters. Even effects of General Relativity such as gravitational redshift could be observed. The influence of the mentioned effects is shown in Fig. 2.2.

2.3.3 Comptonization

The continuum emission found in the spectra of microquasars can be described by a power law extending from soft to hard X-rays, where a exponential cutoff is observed. This emission profile can be explained by Comptonization. Photons can gain energy by inverse Compton scattering with hot electrons. The initial photons, which are called seed photons, originate from the accretion disk,

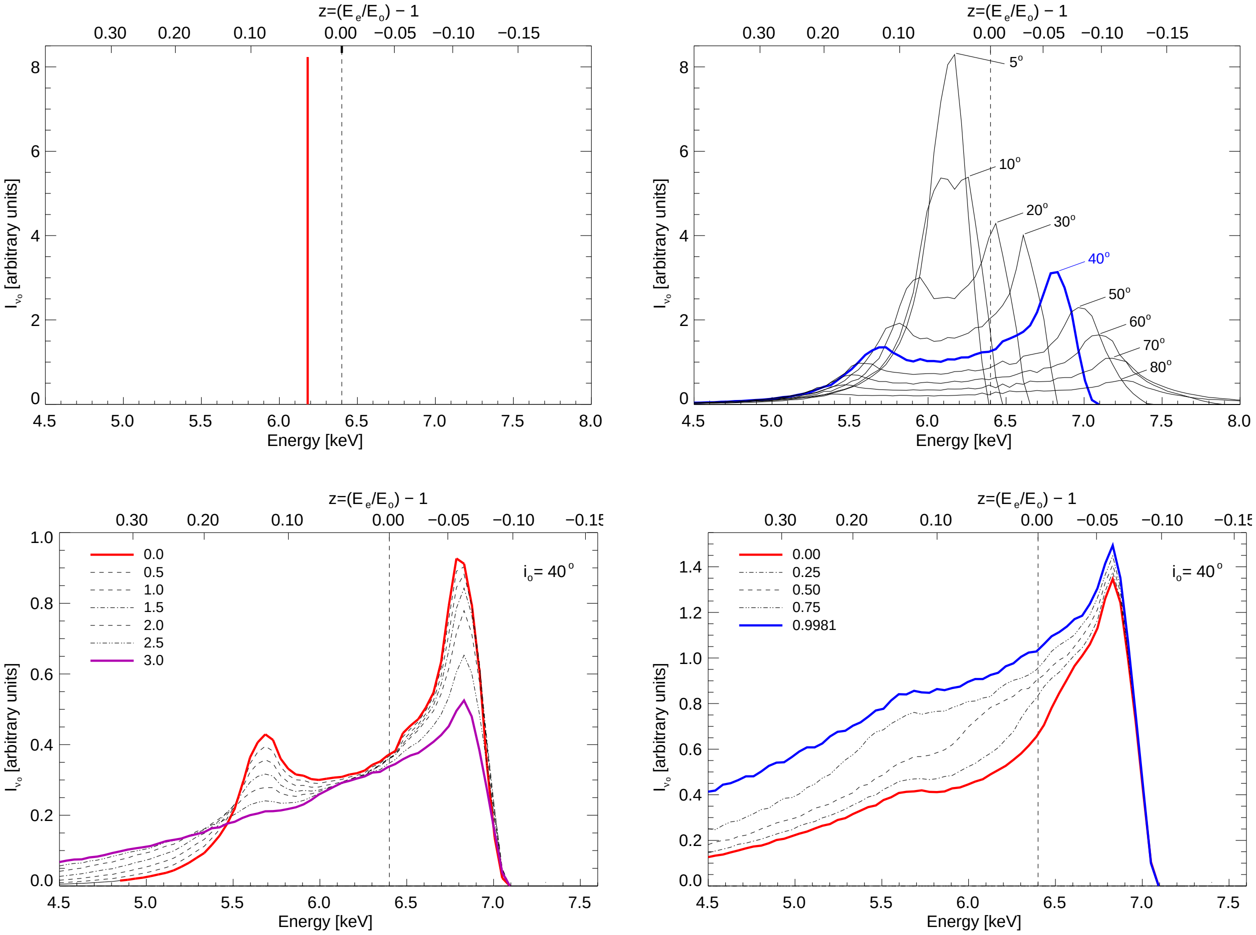

Figure 2.2: Effects on the shape of the iron line. The top left picture illustrates that the observed energy of iron line can be smaller than 6.4 keV due to gravitational redshift. In the top right it is shown how the inclination of the accretion disk would influence the shape of the iron line, due to the Doppler effect, relativistic beaming and light bending effects. The shape of the line depends also on the line emissivity in the disk. In the bottom left picture, the shape of the iron line is shown for different negative exponents of a power law of the radius, which describes the emissivity profile. The influence of the black hole spin is depicted at the bottom on the right. (J. Wilms, priv. comm.)

as soft X-rays are an essential fraction of its black body emission. The up-scattering process is assumed to occur in the corona[4]. This an optically thin and very hot plasma containing electrons, with temperatures corresponding up to 100 keV. Possible geometries of the accretion and the corona are shown in Fig. 2.3. The up-scattering process is described in Rybicki & Lightman (1979, Ch. 7). At first it is helpful to consider the scattering of a photon of energy E with a stationary electron, the standard Compton scattering. After the scattering the photon's energy would be

$$E' = \frac{E}{1 + \frac{E}{m_e c^2}(1 - \cos\theta)} \tag{2.13}$$

where θ is the angle by which the direction of propagation of the photon is changed. For $E \ll m_e c^2$ the energy change of the photon averaged over θ is given by

$$\langle \Delta E \rangle = -\frac{E^2}{m_e c^2} \tag{2.14}$$

---

[4] The origin of the corona is not clear. It is possible that it is caused by magnetohydrodynamical instabilities in the accretion disk (Balbus & Hawley, 1998).

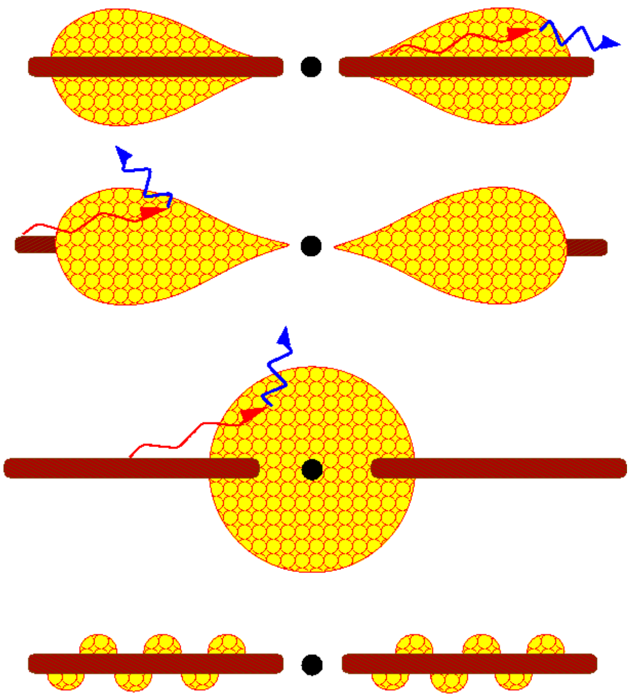

Figure 2.3: Different possible geometries of the corona. In this sketch the accretion disk is show in red and the corona in yellow. The most likely models are the two middle ones. (Nowak (2006) Fig. 1)

The differential cross section of Compton scattering was computed using quantum electrodynamics. For unpolarized radiation it is given by the Klein-Nishina formula

$$\frac{d\sigma_{\mathrm{KN}}}{d\Omega} = \frac{3}{16\pi}\sigma_{\mathrm{T}} \left(\frac{E'}{E}\right)^2 \left(\frac{E}{E'} + \frac{E'}{E} - \sin^2\theta\right) \tag{2.15}$$

where σ_{T} is the Thomson cross section

$$\sigma_{\mathrm{T}} = \frac{8\pi}{3}\left(\frac{q^2}{4\pi\epsilon_0 mc^2}\right)^2 \tag{2.16}$$

where q and m are the charge and the mass of the scattering particle and ϵ_0 is the vacuum permittivity. For an electron the Thomson cross section obtains the value

$$\sigma_{\mathrm{T}} \approx 6.65 \cdot 10^{-25}\mathrm{cm}^2 \tag{2.17}$$

Integrating Eq. 2.15 over the solid angle yields the total cross section

$$\sigma_{\mathrm{KN}} = \frac{3}{4}\sigma_{\mathrm{T}}\left[\frac{1+x}{x^3}\left(\frac{2x(1+x)}{1+2x} - \ln(1+2x)\right) + \frac{1}{2x}\ln(1+2x) - \frac{1+3x}{(1+2x)^2}\right] \tag{2.18}$$

with $x = \frac{E}{m_{\mathrm{e}}c^2}$.

If the electron is in motion, Lorentz transformations between the observer's frame and the frame of rest of the electron have to be applied. In this case the integration over the angles is more complicated. As it is shown in the book of Rybicki & Lightman (1979) in Sect. 7.2–7.4 this finally yields an averaged relative energy change of

$$\frac{\Delta E}{E} = \frac{4k_{\mathrm{B}}T - E}{m_{\mathrm{e}}c^2} \tag{2.19}$$

if non-relativistic electrons, which have a Maxwellian distribution with temperature T, scatter with photons of energy E. If the temperature of the electrons is high enough, the scattering photons gain energy. This process is called inverse Compton scattering.

It is shown by Rybicki & Lightman (1979, Sect. 7.5, 7.6 and 7.7) that the multiple scattering processes can yield a power law spectrum of photons. Thus Comptonization produces power law spectra with exponential cutoff at about $E_0 \approx k_{\mathrm{B}}T$ (Sunyaev & Titarchuk, 1985). This effect is indicated in Fig. 2.4.

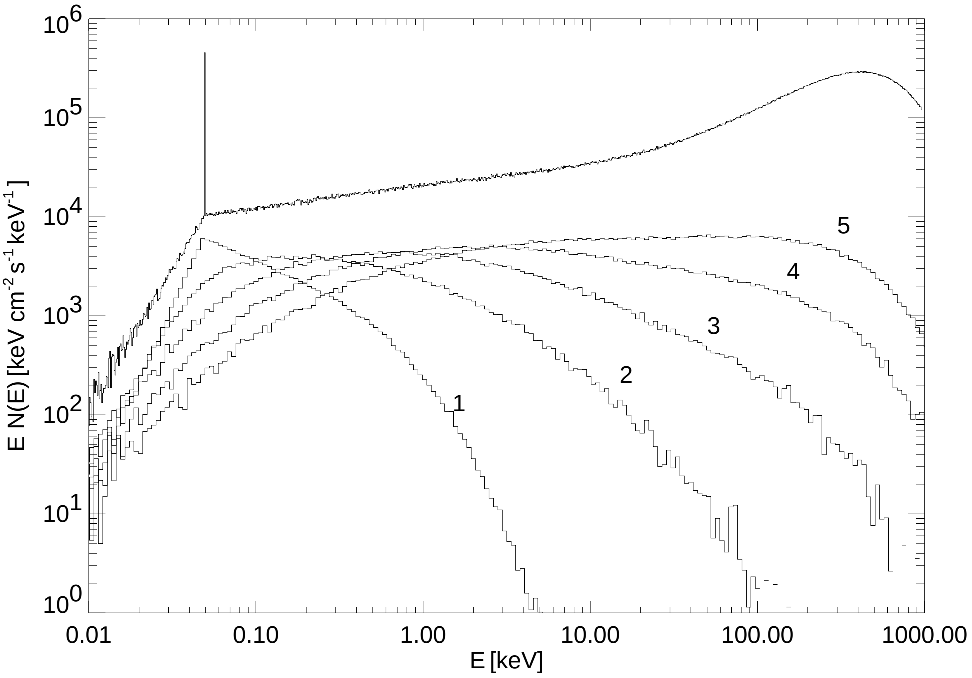

Figure 2.4: Repeated Compton scatterings cause a power law spectrum. The figure is the result of a Monte Carlo simulation by J. Wilms. The energy of the seed photons is indicated by the vertical line. The optical depth is $\tau = 5$ and the energy of the electrons $k_\mathrm{B}T = 200\,\mathrm{keV}$. The number of scatterings is noted. In this case the high temperature with the large optical depth was in order to show a significant gain of energy of the photons by a few scatterings. Due to the saturated inverse Compton scattering the total resulting spectrum becomes a Wien spectrum at high energies, instead of a power law with exponential cutoff.

2.3.4 Jets

Jets of several X-ray sources can be resolved directly. These are relativistic outflows in two opposite directions[5] and usually perpendicular to the accretion disk and probably aligned with the angular momentum of the compact object[6]. These outflows are collimated over long distances and have opening angles of only a few degrees. Jets can be observed with radio telescopes. The length of the jet of an AGN can exceed several kpc by far. They can have a strongly polarized emission, which can be described by synchrotron radiation of charged particles in the jet. Although they can be observed directly, they are not well understood yet. It is not clear whether the ejected particles are electrons and ions or an electron-positron plasma or both. There are also different theories describing the underlying mechanisms of jet formation. The jet formation is a complicated process. Magnetohydrodynamical simulations have shown that jets can be the result of the rotating accretion disk and/or corona. The magnetic field lines are well ordered in the direction of the angular momentum, whereas they seem very chaotic in the disk due to magneto-rotational instability. There is also the theory of the Blandford-Znajek mechanism describing the extraction of energy from Kerr black holes (Blandford & Znajek, 1977), which causes jets. A detailed discussion of the theoretical jet formation processes can be found in the Sect. III. D in the work of Begelman et al. (1984).

Begelman et al. (1984) present an extensive discussion of the theory of jets, including the collimation of jets (Sect. II. C.). The jet can be collimated by gas pressure, other possible collimation

---

[5] For many sources only a one-sided jet is visible. This is probably a relativistic beaming effect.

[6] Precessing jets have been observed as well. A good example is the source SS 433 (Roberts et al., 2008).

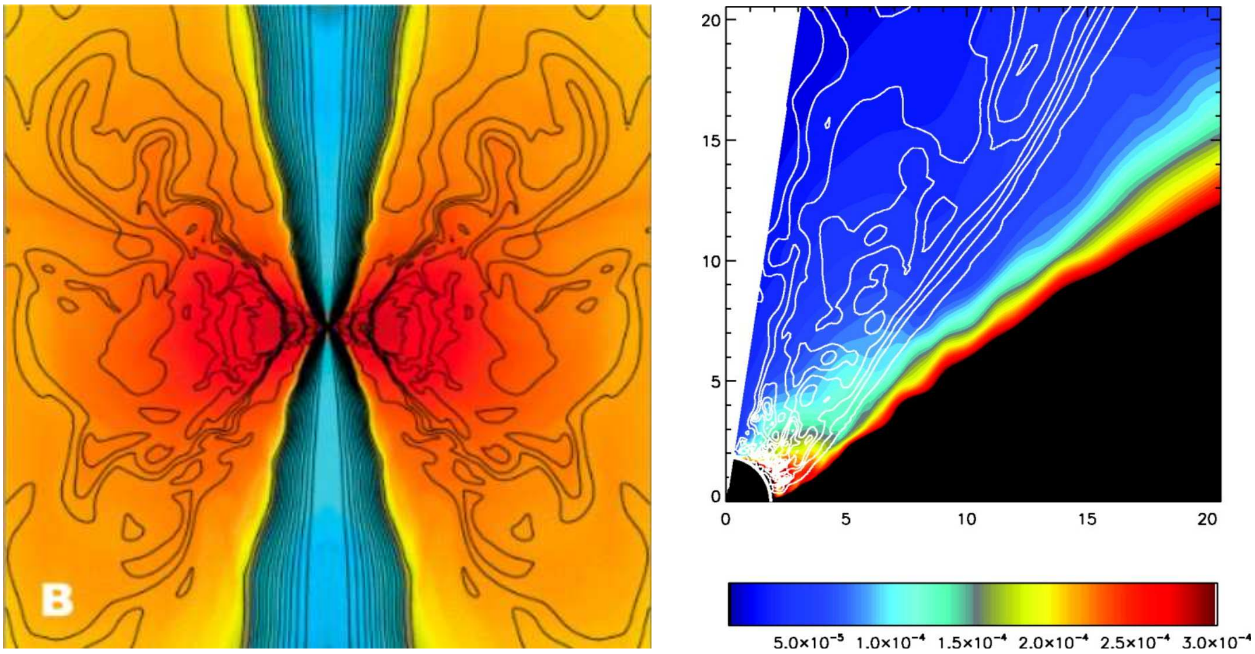

Figure 2.5: Jet formation as a result of magnetohydrodynamical simulations. On the left a Poynting-flux jet is shown. The magnetic field (black lines) is indicated and there is a color-code according to the density around a black hole (logarithmic scaling color, blue for low density and red for high density). There is a funnel region with very low density. The simulation was performed by McKinney (2006). In the right picture the formation of a matter-dominated jet is shown (Hawley & Krolik, 2006). The black hole is located in the bottom left corner. A strong pressure gradient (colors) along the coronal wall was obtained here, which pushes matter into the jet and accelerates it. (Fragile, 2008, Fig. 2, Fig. 4)

mechanisms are radiative cooling of the jet and magnetic collimation. A simulation of the propagation of a jet through the interstellar medium is presented in Fig. 2.6.

The essential radiation process in the outer jet is synchrotron radiation, which is a result of the acceleration of charged particles in magnetic fields. The charged particles in the jet move around the magnetic field lines due to the Lorentz force depending on their velocity component perpendicular to the magnetic field. The magnetic field in the jet is parallel to jet velocity, i.e., the field is mostly longitudinal, but in the outer jet the transversal component can become dominant. The reason is that the jet expands sideways. The magnetic flux in the jet is conserved along the jet as long as there are no magnetic fields from the ambient medium. The strength of the magnetic field depends on the distance d from the source. The longitudinal and transversal components of the magnetic field have a different dependence on the radius, there are the relations $B_{\|} \propto d^{-2}$ and $B_{\perp} \propto d^{-1}$. This effect changes the polarization of the emission and can thus be seen clearly in observation. It can be shown that the synchrotron radiation of electrons with an energy distribution given by a power law yields a power law spectrum. See Rybicki & Lightman (1979, Ch. 6) for a detailed discussion of synchrotron radiation.

The total radiation processes tied to a jet are explained by the example of jet model by Markoff et al. (2005). This model includes the thermal radiation of the accretion disk, as its properties have influence on the jet. A very important component is the base of the jet, where Comptonization occurs. There is external Comptonization (EC), in this case thermal photons from the disk are up-scattered. In the synchrotron self-Comptonization (SSC) the seed photons originate from synchrotron radiation. The derived properties of the plasma forming the base of the jet are very similar to that of the corona, which were obtained from Comptonization fits. It is possible that the corona and the jet base are identical.

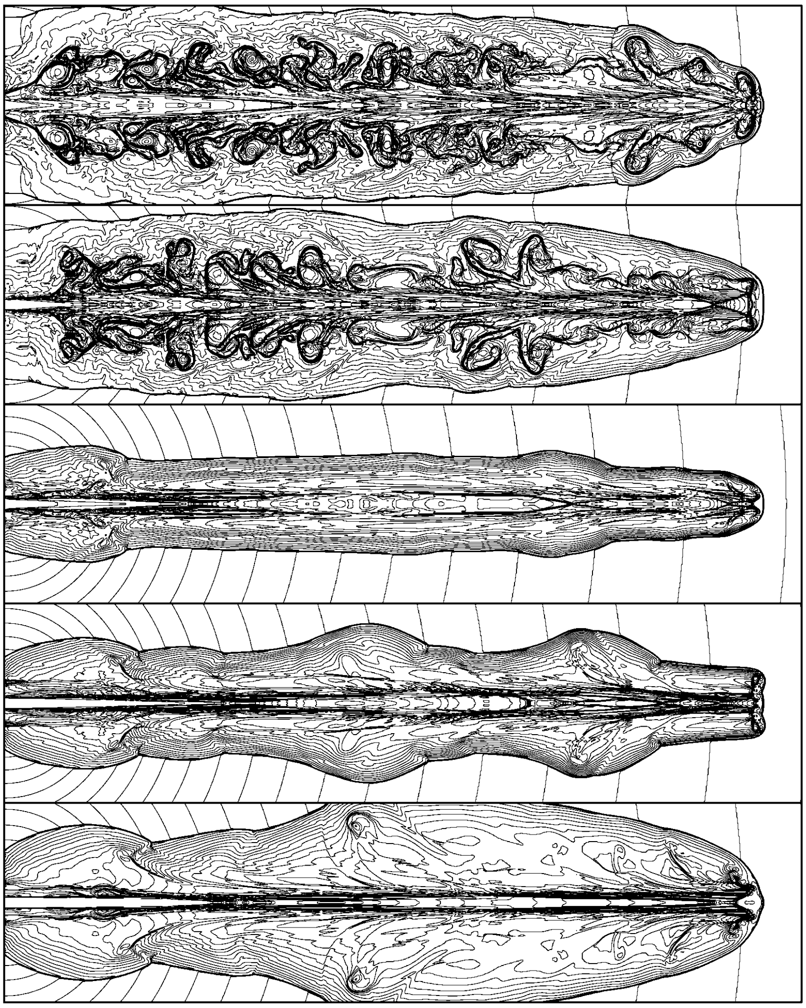

Figure 2.6: A simulation of the propagation of a jet in the inter stellar medium. The density ratio of the jet to that of the ambient medium is increased top down, as well as the Mach number of the jet Carvalho & O'Dea (2002, Fig. 1).

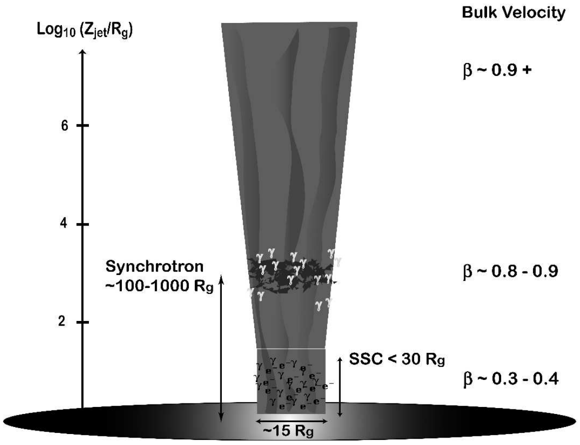

Figure 2.7: Sketch of the geometry of the jet model by Markoff et al. (2005). There is thermal radiation from the accretion disk. These photons are reprocessed in the base of the jet (external Comptonization), where also synchrontron self-Comptonization occurs. Above the jet expands freely. There is synchrotron radiation throughout the jet.

Another jet model is given by Foellmi et al. (2008). They consider a jet emitting disk (JED), whose geometry can vary resulting in changes of the emission properties. The total emission properties are quite similar to that of the model above.

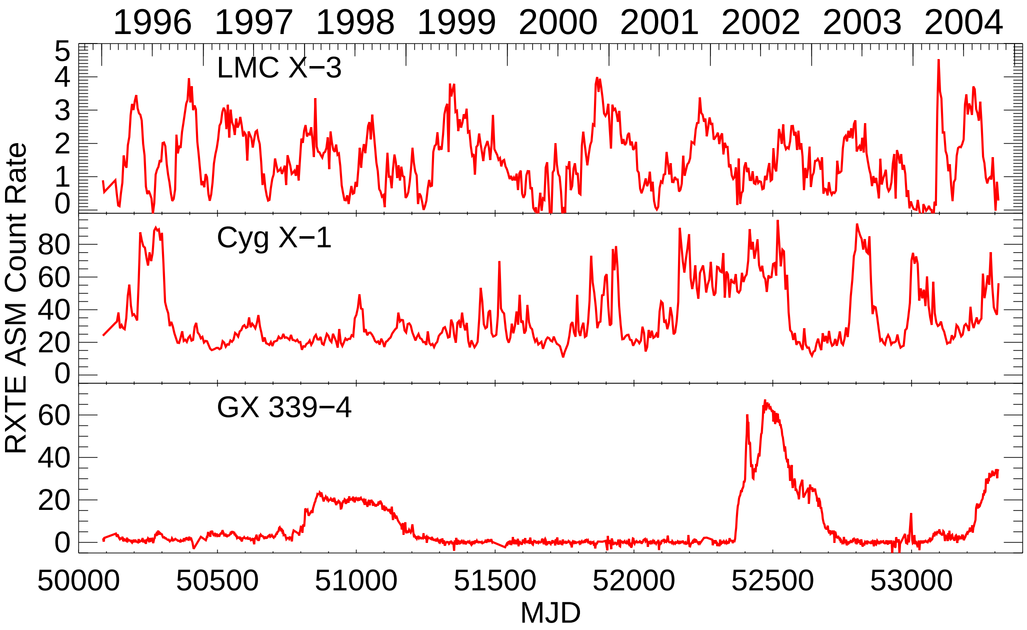

Figure 2.8: The soft X-ray variability of different sources. LMC X-3 is a persistent X-ray binary consisting of a B5V star and a 9.5–13.6 $M_\odot$ black hole (Val-Baker et al., 2007). The HMXB Cyg X-1 is discussed in Sect. 2.5. The companion star of the galactic X-ray source GX 339-4 has not been detected and there are only upper limits to the star's luminosity (Dunn et al., 2008). It is thus classified as a LMXB. The time is noted in the form of the Modified Julian Date (MJD), which is defined by MJD = JD − 2400000.5. The Julian Date JD is the number of days since -4712 Jan 1, 12 h. (J. Wilms, priv. comm.)

2.4 States

The emission in X-ray binaries can be very variable. Different sources show different behavior, but also the emission of a single X-ray binary can change strongly with time. Fig. 2.8 shows light curves, which are the count rates as a function of time, of the sources LMC X-3, Cyg X-1 and GX 339-4. Nevertheless, characteristic properties are found in the emission. Based on these properties it is possible to classify the emission into states. Transitions between these states have been observed. The two standard states are the hard state and the soft state. They are characterized by their spectral shape. As the name indicates the spectrum of a source in the hard state is hard, i.e., the ratio of low energy X-rays to X-rays of higher energy is relatively small. This ratio is much larger in the soft state. Considering the soft X-ray flux, the soft state is also called high state, whereas the hard state is called low state. As the spectra can be described by a power law $E^{-\Gamma}$, a value to characterize the hardness of a spectrum is the photon index Γ. The typical value of Γ depends on the source. There was also an intermediate state introduced between hard and soft state. A possible explanation of the spectral shape is the accretion geometry. In the hard state the accretion disk is only weakly extended with a large inner radius. The emitted photons are reprocessed in a hot corona and reach high energies due to inverse Compton scattering. Thus the resulting spectrum is hard. In the soft state the accretion disk reaches closer to the black hole and its thermal emission is strongly increased, leading to Compton cooling of the corona. For that reason the spectrum is softer. An overview of these states is shown in Fig. 2.9.

This explanation for the different states is by far too simple, as the states do not only have different spectral shapes but there are additional properties. A detailed summary of the properties of the different state are shown in Fig. 2.10. According to these properties there are even more states introduced than mentioned above. Here also radio emission and timing properties are considered.

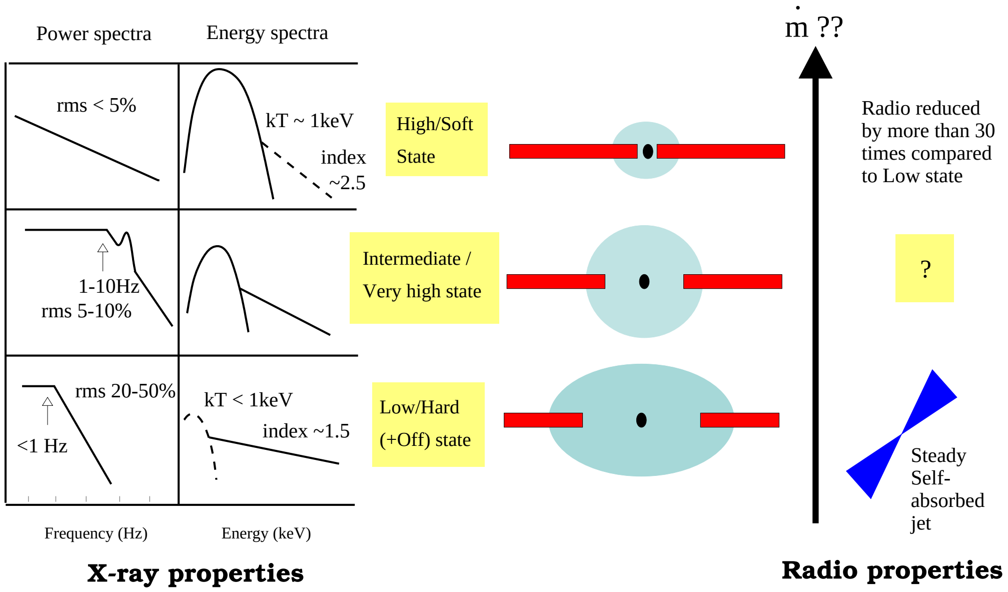

Figure 2.9: Overview of the most important states, which are characterized by the shape of their energy spectra. The shape is explained by the accretion geometry, considering the thermal emission of the accretion disk (red) and the Comptonization in a corona (blue). (Fender, 2002, Fig. 4)

For example there is evidence for a steady jet in the hard state. If the spectrum gets softer there seems to be a certain limit called jet line, where the jet disappears. In this region radio flares can be observed. There are also characteristic timing properties, resulting from a detailed analysis of the light curves. For example its rms (root mean square) of the variance changes throughout the states. Methods of timing analysis and the results are discussed in detail in Sect. 5.

In the center of Fig. 2.10 a hardness intensity diagram is shown, illustrating that the states are allocated in certain positions in this diagram. There is also a typical track of a source sketched. The transitions between the states are assumed to occur in certain sequence. Note that several sources exhibit a characteristic behavior and not all of them follow the shown track trough the states. Due to the shape of the track, this diagram is called q-diagram.

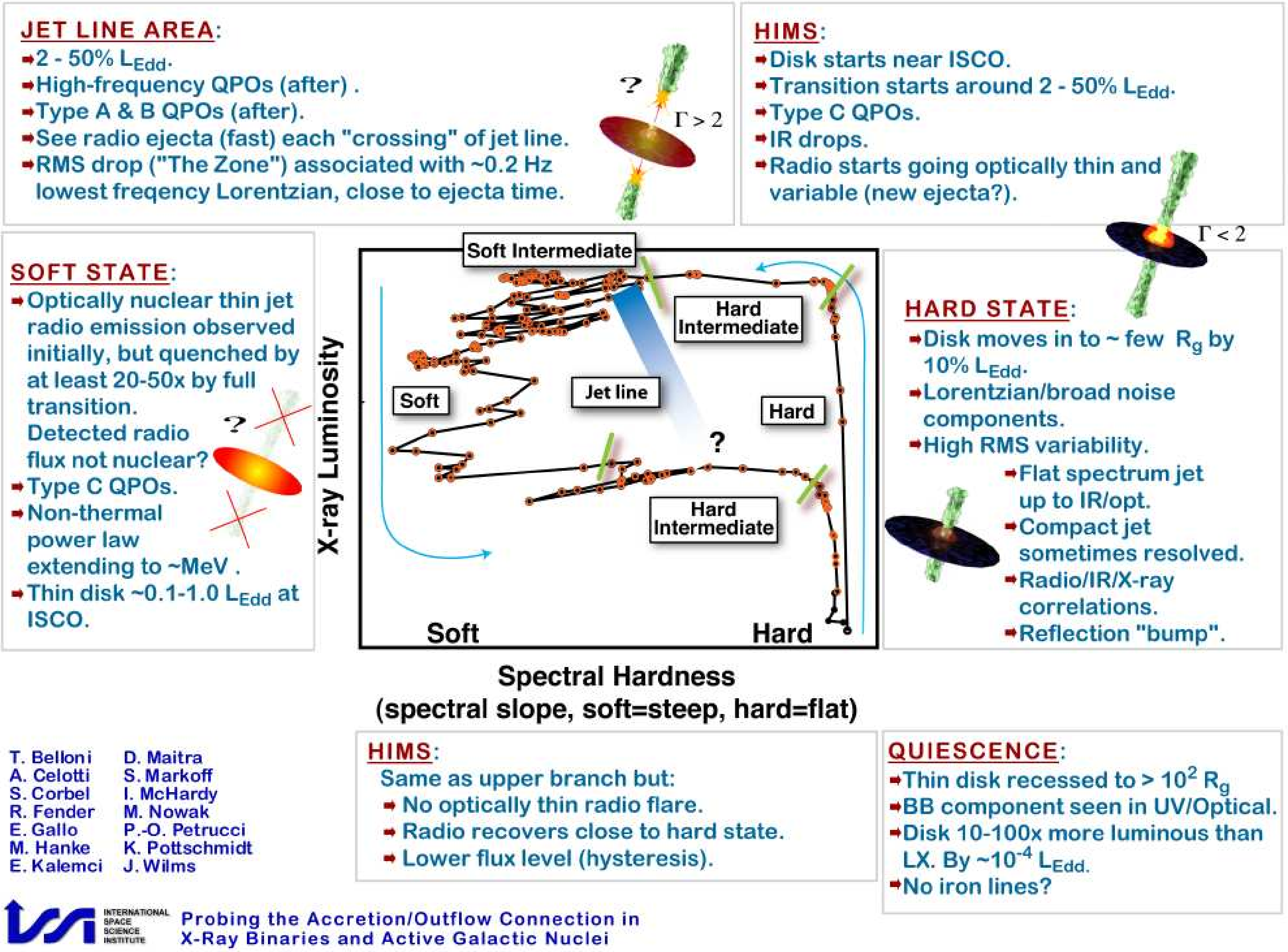

JET LINE AREA:
- 2 - 50% L_{Edd}.
- High-frequency QPOs (after) .
- Type A & B QPOs (after).
- See radio ejecta (fast) each "crossing" of jet line.
- RMS drop ("The Zone") associated with ~0.2 Hz lowest freqency Lorentzian, close to ejecta time.

HIMS:
- Disk starts near ISCO.
- Transition starts around 2 - 50% L_{Edd}.
- Type C QPOs.
- IR drops.
- Radio starts going optically thin and variable (new ejecta?).

SOFT STATE:
- Optically nuclear thin jet radio emission observed initially, but quenched by at least 20-50x by full transition. Detected radio flux not nuclear?
- Type C QPOs.
- Non-thermal power law extending to ~MeV .
- Thin disk ~0.1-1.0 L_{Edd} at ISCO.

HARD STATE:
- Disk moves in to ~ few R_g by 10% L_{Edd}.
- Lorentzian/broad noise components.
- High RMS variability.
  - Flat spectrum jet up to IR/opt.
  - Compact jet sometimes resolved.
  - Radio/IR/X-ray correlations.
  - Reflection "bump".

HIMS:
Same as upper branch but:
- No optically thin radio flare.
- Radio recovers close to hard state.
- Lower flux level (hysteresis).

QUIESCENCE:
- Thin disk recessed to > 10^2 R_g
- BB component seen in UV/Optical.
- Disk 10-100x more luminous than LX. By ~10^{-4} L_{Edd}.
- No iron lines?

T. Belloni
A. Celotti
S. Corbel
R. Fender
E. Gallo
M. Hanke
E. Kalemci
D. Maitra
S. Markoff
I. McHardy
M. Nowak
P.-O. Petrucci
K. Pottschmidt
J. Wilms

Probing the Accretion/Outflow Connection in X-Ray Binaries and Active Galactic Nuclei

Figure 2.10: Detailed overview of the properties of the states. The hardness intensity diagram in the center indicates the typical sequence in which state transitions occur. Due to its shape it is called q-diagram. (Picture courtesy of International Space Science Institute (ISSI), see `http://www.sternwarte.uni-erlangen.de/proaccretion/`).

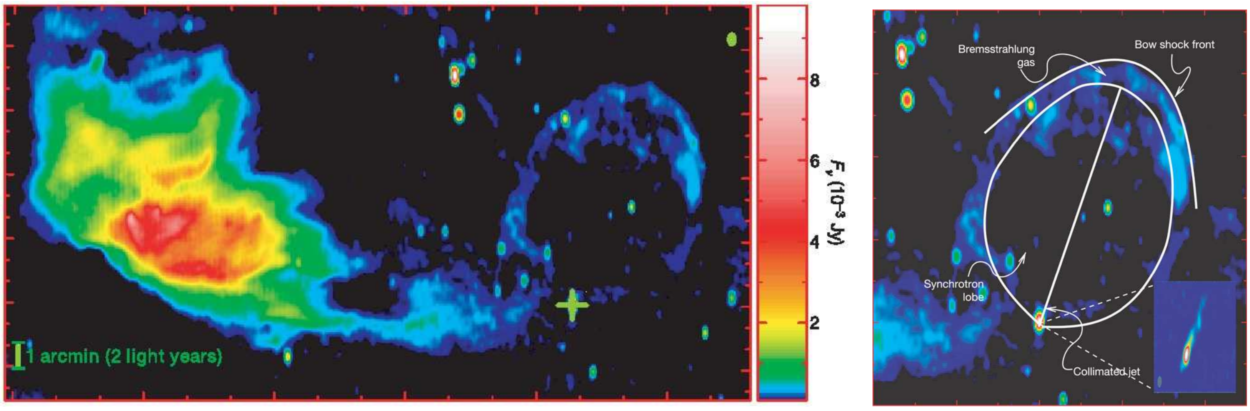

Figure 2.11: Picture of the region around Cyg X-1, whose position is marked by the cross, as it is seen at the 1.4 GHz radio flux. The bright structure to the left is the H II emission nebula Sh2-101. The radio emitting ring with a diameter of about 15 light years is caused by Cyg X-1. The picture on the right illustrates its origin: A collimated relativistic jet inflates a synchrotron-emitting lobe, which expands sideways interacting with the interstellar medium, thus the shock-compressed gas emits bremsstrahlung. (Gallo et al., 2005)

2.5 Cygnus X-1

Cygnus X-1 (Cyg X-1) is one of the brightest X-ray sources in the sky. It is located in the constellation Cygnus and was discovered during a rocket flight in 1964 (Bowyer et al., 1965). The nature of this source was not clear at first. In 1971 a radio outburst occurred (Hjellming & Wade, 1971), whose position was determined accurately, simultaneously changes in the X-ray spectrum occurred. The position of the radio outburst was consistent with that of the star HDE 226868[7], which is classified as a O9.7Iab supergiant. This allowed an identification of the compact object with a companion star. Measurements of the radial velocities by Webster & Murdin (1972) confirmed that this identification was correct. The orbital period of the system is 5.599829(16) days (Brocksopp et al., 1999b). The orbital modulation is discussed in more detail in Sect. 5.1.1. A distance of the binary of 2.5(3) kpc was determined by Ninkov et al. (1987). Different values for the mass of Cyg X-1 have been calculated, but almost all of them exceeded the Oppenheimer-Volkoff limit. For that reason the compact object cannot be a neutron star. Cyg X-1 was the first detected black hole candidate. Herrero et al. (1995) determined the mass of the companion star to $M_\star \approx 17.8\,M_\odot$ and that of the black hole to about $M_\mathrm{X} \approx 10.1\,M_\odot$ for an inclination $i \approx 35°$ (Gies & Bolton, 1986)[8]. These values are commonly accepted at the moment, although quite different values were obtained in former calculations. $M_\star$, $M_\odot$ and i are connected via the mass function (Eq. 2.5), which is $0.252\,M_\odot$ for Cyg X-1. The mass of the star can for example be estimated from the analysis of its spectrum. If the inclination is known the mass of the compact object can be determined. In other works different values of the mass of the star and thus different black hole masses were computed. Ziółkowski (2005) even claims $M_\star = 40 \pm 5\,M_\odot$ and thus $M_\mathrm{X} = 20 \pm 5\,M_\odot$. A quite small mass of the compact object was obtained by Shaposhnikov & Titarchuk (2007), who obtained $M_\mathrm{X} = 8.7 \pm 0.8\,M_\odot$ from spectral-timing relations. The high masses were derived using non-standard methods. Plausible values are those given by Herrero et al. (1995). They also determined several parameters of HDE 226868, namely a radius of $R_\star = 17\,R_\odot$[9], an effective temperature

---

[7] The Henry Draper Extension (HDE, published between 1925–1936, see Cannon (1936)) is an expansion of the Henry Draper Catalogue (HD, 1918–1924). In the Henry Draper Extension Charts (HDEC, 1937–1949) more than 350 000 stars are classified.

[8] Abubekerov et al. (2004) determined a consistent value of $31° < i < 45°$.

[9] The solar radius is $R_\odot = 7 \cdot 10^8$ m.

$T_{\mathrm{eff}} = 32\,000\,\mathrm{K}$ and a luminosity of $L_\star \approx 10^{5.4}\,L_\odot$[10]. The supergiant has a mass loss rate of about $\dot{M}_\star = 3 \cdot 10^{-6}\,M_\odot\,\mathrm{y}^{-1}$ due to its strong stellar wind, which can be accelerated up to a terminal velocity of 2100 km/s. HDE 226868 almost fills its Roche lobe, but nevertheless wind accretion is the dominant accretion process in this system. The separation of the star and the compact object is believed to be only $40\,R_\odot$. The wind is strongly focused toward Cyg X-1. As mentioned above up to 0.1% of the material emitted by the star is accreted by the black hole, causing an emission of energy, especially in the form of X-rays. The average luminosity of Cyg X-1 is about $L_\mathrm{X} = 4 \cdot 10^{30}\,\mathrm{W} \approx 10^4\,L_\odot$. The characteristic properties of this emission are discussed in this work. Cyg X-1 is a persistent X-ray source, as the stellar wind causes a relatively continuous accretion rate, which is not the case for transient LMXBs. But nevertheless Cyg X-1 is a strongly variable X-ray source. Its long-term monitoring (Pottschmidt et al., 2003; Wilms et al., 2006) shows that the source was found in hard and soft states several times, thus there had to be transitions in between. Also so-called "failed state transitions" occurred, which are often connected with strong X-ray flares. Although Cyg X-1 is a well studied source, it is still unclear what the emission mechanisms are in detail and how they change between the states. Cyg X-1 is found in hard, soft and intermediate states, but however it does not follow the complete sequence of transitions shown in the q-diagram, instead it seems that this source changes from the hard to the soft state and back on the upper branch in the q-diagram. The data used in this work here cover a full transition from the hard to the soft state, allowing a detailed analysis of the changes in the emission, which are tied to the transition.

There is also evidence that Cyg X-1 has a relativistic jet. The detected radio emission of Cyg X-1 can be explained by the synchrotron emission of a jet. It is even possible to resolved radio emitting "blobs" in the jet directly (e.g., Fender et al., 2006, Fig. 2). Fig. 2.11 shows a ring emitting 1.4 GHz radio waves, which is believed to indicate the shock front between the interstellar medium and a lobe inflated by the jet.

---

[10] The solar luminosity is $L_\odot \approx 3.8 \cdot 10^{26}\,\mathrm{W}$.

Chapter 3

Data

Celestial objects can only be studied by analyzing the information reaching the Earth. The most convenient method is to study electromagnetic waves. Note however that there can be various particle radiation, which can be measured. For example several neutrino detectors are constructed. In order to understand the behavior of these objects, such as binaries in this case, it is of course necessary to obtain as much information as possible. The observation of binaries in different wave bands sets a basis for their investigation. The atmosphere of the Earth is not transparent for all kinds of electromagnetic waves however, but the transparency depends on the wavelength, as illustrated in Fig. 3.1. For that reason only certain wavelengths can be observed from the ground. The atmosphere is highly transparent for radio waves and visible light, whereas it is opaque for ultraviolet (UV), X-rays and γ-rays.

In this work radio and X-ray data were analyzed. In this chapter it is described how these data were obtained and the methods of the analysis are explained.

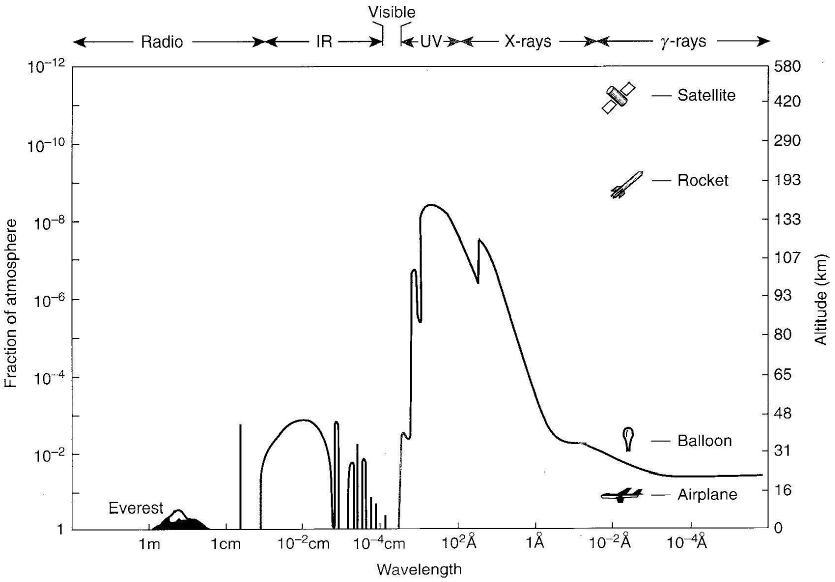

Figure 3.1: The pentration depth of electromagnetic waves into the atmosphere of the Earth depends on the wave length. The illustration shows in which altitude only the half of the incoming radiation remains. (from Charles & Seward (1995, Fig. 1.12))

Figure 3.2: Compact configuration of the Ryle Telescope. 5 of its 8 elements, which can be moved on rail tracks, are grouped together. (Picture courtesy: www.mrao.cam.ac.uk/telescopes/ryle/)

3.1 Radio Data

As mentioned above radio waves can penetrate the Earth's atmosphere and can thus be detected from the ground. The measurements are performed with radio telescopes, which typically consist of a large parabolic (or spherical) dish focussing the radio waves to a detector. A detailed description of how radio telescopes work is given in Rohlfs & Wilson (2004). The measured wavelengths depend on the construction of the telescope and are in the range from 30 m, which corresponds to a frequency of 10 MHz, to the sub-millimeter region. As this range covers quite a few orders of magnitude, it is obvious that the size of the telescopes also varies. The best possible angular resolution θ of a radio telescope depends on the diameter of the dish D and the wavelength λ of the observed radiation and is given by the Rayleigh criterion:

$$\sin\theta = 1.220\frac{\lambda}{D} \tag{3.1}$$

For larger λ bigger dishes are used. Radio telescopes which are constructed to observe electromagnetic radiation with a wavelength of several meters need a dish with a diameter of about 100 m or more, in order to achieve an angular resolution of a few degrees. This is not a satisfying resolution for scientific research. The resolution can be improved by increasing the dishes, but this is not meaningful as dishes with a diameter in the length scale of kilometers are quite impractical. A solution was found in the Very Long Baseline Interferometry (VLBI), which is described in detail in Thompson et al. (2001). The underlying principle of the interferometry is to combine many telescopes instead of using a large one, to measure simultaneously with all telescopes and to correlate the data. The angular resolution of such a system corresponds to that of a single radio telescope with a dish diameter identical to the largest distance between the telescopes. For example in the Very Long Baseline Array (VLBA), which is an array of ten radio telescopes distributed over the USA, the longest baseline is more than 8000 km. It can detect radio waves between 300 MHz and 86 GHz, thus the highest angular resolution is less than 1 milliarcsecond.

The radio flux is measured in units of jansky (Jy), which is defined by $1\,\mathrm{Jy} = 10^{-26}\,\mathrm{W\,m^{-2}\,Hz^{-1}}$. The typical measured 15 GHz radio flux density[1] caused by the Sun amounts to $4.5\cdot10^{6}$ Jy, whereas that of Cygnus X-1 averages 15 mJy at the Earth. To get a feeling for the unit janksy it is helpful

---

[1] `http://www.swpc.noaa.gov/ftpdir/lists/radio/7day_rad.txt`

to consider a measurement on the Earth of the radiation of a cellphone located on the Moon. Its transmission power is assumed to be about 2 watts in the frequency band around 0.9 GHz with a band width of about 100 kHz[2]. Such a cellphone on the Moon would then cause a radio flux of about 10^3 Jy at the Earth. Thus it would be the fourth brightest radio source at this frequency in the sky after the radio galaxy Cygnus A (∼1500 Jy), the supernova remnant Cassiopeia A (∼2500 Jy) and the sun. This comparison illustrates clearly why the different uses of radio technology, such as audio, telephony, video, navigation, radar, heating and so forth are a problem for radio astronomy. However, these applications use specific frequencies and there are some frequency bands protected for astronomy. For that reason it is still possible to obtain good data of celestial radio sources.

The radio data analyzed in this work were measured at 15 GHz (2 cm wavelength) with the Ryle Telescope (Fig. 3.2), which is located at the Mullard Radio Astronomy Observatory (MRAO) near Cambridge (UK). It consists of 8 elements. Each element is an antenna with a 13 m dish. They are mounted on rail tracks, on which they can be moved. The longest possible baseline is 4.8 km. Further information on the Ryle telescope and explanations of phase-calibration observations are given in Pooley & Fender (1997) and Wilms et al. (2007).

3.2 X-ray Data – Rossi X-ray Timing Explorer

In contrast to the radio waves X-rays are not used commercially to a large extent in the environment, as they are a serious health hazard to living organisms. An unimpaired measurement on the ground of cosmic X-rays is however not possible. This is due to the atmosphere of the Earth, which is opaque for this radiation. For that reason a measurement of X-rays originating from celestial sources can only be performed outside the atmosphere or in its upper layers. As mentioned in Sect. 1.1 detectors mounted on rockets were used at first to measure the cosmic X-ray radiation. In order to obtain data on longer periods of time satellites are necessary. An overview of the high energy missions is given in `http://heasarc.gsfc.nasa.gov/docs/heasarc/missions/`, where the past, active and the upcoming satellites are listed.

The data analyzed in this work were obtained with the Rossi X-ray Timing Explorer (*RXTE*), which is a satellite that observes X-ray sources. Light curves and spectra of the observed source can be extracted from the raw data provided by the satellite. There are extraction scripts available[3]. HEASOFT 6.3.1 was used to extract the data which are analyzed in this work. The possible properties, such as time resolution or the spectral binning of the extracted data depends on the data modes used during the observation. A mode is characterized by the way in which detector events are processed by the satellite's electronic. A detailed description of the data modes of the detectors aboard *RXTE* is provided by the HEASARC[4]. The most important characteristics of *RXTE* and its instrument will be described in the following. During the last years it provided data, which were outstanding for scientific research of the sources and the processes causing the X-ray emission. *RXTE* was launched in December 30, 1995 into a circular low earth orbit, with an altitude of 580 km. This results in an orbital period of about 90 minutes[5]. The inclination of the orbit is 23 degrees. Five years were the planned lifetime of *RXTE*. Luckily this goal was passed by far and *RXTE* is still working. The importance of this satellite is based on the combination of the properties of its instruments. Pointed observations with a very large collecting area and a high time resolution can be performed with *RXTE*, but also all-sky monitoring is possible. The spectral range is 2–250 keV. The combination of features is achieved by using different detectors.

---

[2] For mobile phones using the GSM network, the transmission power is limited to 2 watts in the frequency bands around 0.9 GHz (GSM850/900) and 1 watt around 1.9 GHz (GSM1800/1900) (see: `http://en.wikipedia.org/wiki/GSM`).

[3] The scripts are described in detail on NASA's High Energy Astrophysics Science Archive Research Center (HEASARC): `http://heasarc.gsfc.nasa.gov/docs/xte/abc/extracting.html`

[4] `http://heasarc.gsfc.nasa.gov/docs/xte/RXTE_tech_append.pdf`

[5] `http://heasarc.gsfc.nasa.gov/docs/xte/XTE.html`

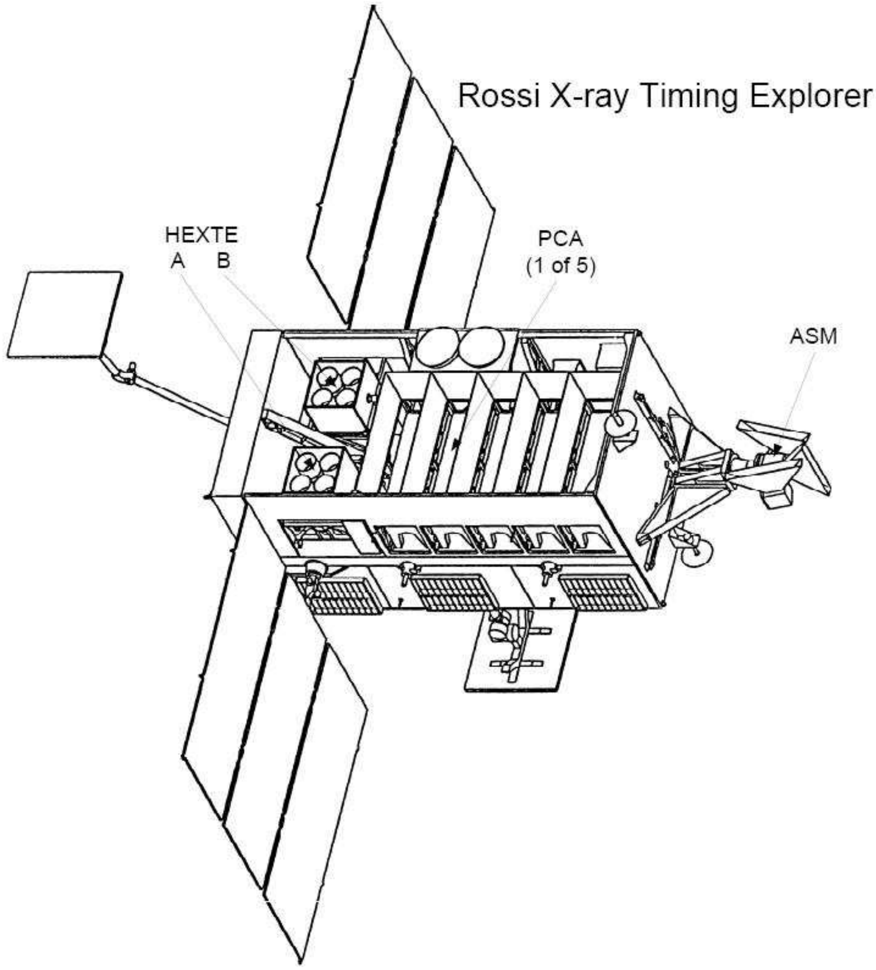

Figure 3.3: Schematic view of the *RXTE* spacecraft. Its instruments are labeled. There is the All-Sky Monitor (ASM) consisting of three wide-angle shadow cameras. Five Proportional Counter Units (PCUs) form the Proportional Counter Array (PCA). The High Energy X-ray Timing Experiment (HEXTE) consists of two clusters A and B. Not labeled are the solar panels, which are located on the sides of the satellite and its antennas, which are mounted on the outside. There are also two star trackers aboard the satellite (above PCA in this picture). They are necessary for the alignment of the satellite. (Rothschild et al., 1998, Fig. 1)

There are three different instruments aboard the spacecraft, namely the All-Sky Monitor (ASM; Levine et al., 1996), the Proportional Counter Array (PCA; Jahoda et al., 1996, 2006) and the High Energy X-ray Timing Experiment (HEXTE; Rothschild et al., 1998). Their set-up on the satellite is illustrated in Fig. 3.3. The important characteristics of the instruments will be described in the following, detailed information can be found in the noted references.

3.2.1 All-Sky Monitor

As its name indicates the purpose of the All-Sky Monitor (ASM) is to scan the whole sky and monitor X-ray sources. The spectral range of the ASM extends from about 2 to 10 keV. The ASM consists of three identical scanning shadow cameras (SSCs), which are mounted on a rotatable boom. Each of them has a wide field of view (FOV) of 6° × 90°. Due to the arrangement of the cameras most of the sky (about 80%) can be scanned every 90 minutes. This arrangement can be seen in Fig. 3.4, its position on the satellite is illustrated in Fig. 3.3. The region which is close to the Sun is not scanned, because of the X-ray emission of the sun. Performing in this way the

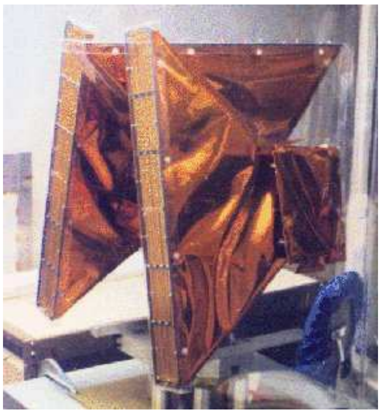

Figure 3.4: The three scanning shadow cameras of the ASM. A coded mask is located on top of each camera and a position-sensitive proportional counter on the bottom. (Picture from: `http://heasarc.gsfc.nasa.gov/docs/xte/learning_center/asm.html`)

ASM provides several observations or at least one per day of bright X-ray sources and thus is very helpful to investigate the long-term behavior of these sources. Of course only the variability of the sources in the 2–10 keV band is measured. But for most sources the behavior in different energy bands is correlated. Knowing the behavior in the 2–10 keV emission, it is therefore possible to estimate that in other energy bands for well studied sources. For a detailed study sources have to be observed with other instruments. The All-Sky Monitor is also very important to indicate interesting timeframes for observations with other instruments. As it scans large amounts of the sky in the timescale of hours, it is perfectly adapted to detect interesting phenomena which are worth being analyzed in detail. Such phenomena are for example increasing X-ray emission from transient sources, outbursts or other changes in the radiation originating from known or even by then unknown sources. In order to be able to identify a measured count rate with a specific source a certain angular resolution is necessary. That of the ASM is $3' \times 15'$. This resolution is achieved by using a coded mask on top of each camera in combination with a position-sensitive proportional counter at the bottom of the cameras. The structure of opaque and transparent parts of the mask causes a characteristic shadowgram on the detector from that the direction of the photons can be reconstructed. This process yields the mentioned spatial resolution.

3.2.2 Proportional Counter Array

The name Proportional Counter Array (PCA) already implies that this instrument is an array of proportional counters. There are five proportional counter units (PCUs), which are filled with xenon gas. PCA is sensitive to X-rays with an energy of 2–60 keV with a spectral resolution of 18% at 6 keV and its total collecting area is $6500\,\mathrm{cm}^2$. Its purpose is completely different to that of the ASM. Whereas the ASM has a large field of view in order to scan the whole sky within a short period of time, PCA is constructed to perform pointed observations. Its FOV is about 1° due to the limitations of a collimator. In contrast to the moderate energy resolution PCA has an excellent time resolution of 1 microsecond.

A more detailed description of the PCA and its functionality is given by Jahoda et al. (1996) and Jahoda et al. (2006). See Kreykenbohm (2004, Sect. 4.2.1) and the references therein for a summarized version.

PCA has several data modes, such as binned mode, pulsar fold, delta binned, event encoded and additional ones. In this work the binned mode was used. There is a standard event analyzer ("standard2f") with a time resolution of 16 s, i.e. the counts are binned to time intervals of 16 s. A spectral resolution is given by binning the events to 129 channels[6] covering the energy range 2–118 keV. This range is larger than that quoted above, which is the one in that good data can be obtained. Light curves can be extracted in different energy bands by using only specific channels for the extraction. Depending on the modes it is possible to obtain light curves with other time

---

[6] The energy range of the 129 bins is summarized at: `http://heasarc.gsfc.nasa.gov/docs/xte/e-c_table.html`

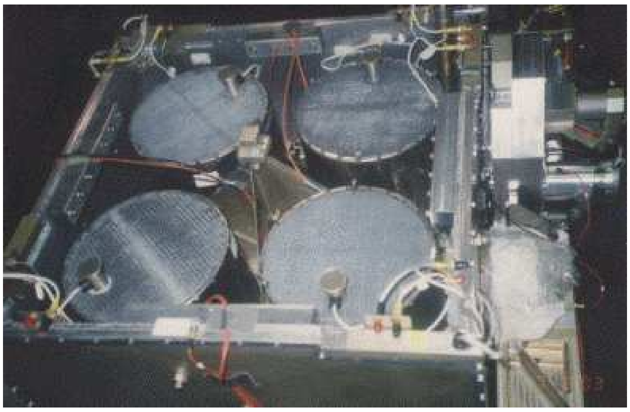

Figure 3.5: One of the two clusters of scintillation counters of HEXTE.
(Picture from the NASA `http://heasarc.gsfc.nasa.gov/docs/xte/learning_center/hexte.html`)

resolution, such as 2 ms, 250 μs, and 125 μs.

3.2.3 High Energy Timing Experiment

The third instrument aboard *RXTE* is the High Energy X-ray Timing Experiment (HEXTE). It consists of two clusters (HEXTE A and B) of 4 NaI/CsI scintillation counters. Its phoswich[7] ("phosphor sandwich") detectors are constructed to measure hard X-rays even for a high background radiation. The energy range of HEXTE is 15–250 keV. Similar to the PCA, HEXTE has a moderate spectral resolution of about 16% at 60 keV, but a good time resolution. A sampling rate of 8 μs is possible. HEXTE's field of view is 1° and it points in the same direction as PCA. This can be seen in Fig. 3.3. HEXTE and PCA are arranged to observe the same source simultaneously. However, HEXTE A and B are not fixed pointing in this position, but can be moved independently. The mobility of these clusters is necessary for the so-called "rocking" process, which is used to determine the background radiation accurately. Rocking means that each cluster is alternately on- and off-source, i.e. it points on the source for a certain time and then changes the direction some degrees (1.5° or 3°) away from the source. The clusters switch in orthogonal directions to avoid distortions of the data by another source in the background field of view. For that reason each cluster has two off-source positions in addition, called "plus" and "minus". Thus different backgrounds per cluster can be extracted if necessary.

3.3 Available Data

All the analyzed X-ray data were obtained with the instruments aboard the *Rossi X-Ray Timing Explorer*. The total PCA light curve in the energy band 4.5–5.8 keV is shown in Fig. 3.6, also is that of *RXTE* ASM and the radio data which was obtained with Ryle Telescope. The *RXTE* observation, which had the ID 90127, started at about MJD = 53402.32. This corresponds to seven forty a.m. at the first of February 2005. The data cover the following 10 days.

For the spectral analysis HEXTE data in the energy range 20–200 keV were considered. Corresponding spectra between 4 and 20 keV were extracted from the PCA data. In addition light curves in several energy bands were obtained using the PCA data. To compare the results with that of a long-term analysis by Pottschmidt et al. (2003) it was convenient to use similar energy bands. For that reason two energy bands were chosen namely a "low" energy band of ~4.5–5.8 keV (PCA channels 11–13) and a "high" one with the range ~9.5–15 keV (PCA channels 23–35). A problem was that the energy range of each PCA channel shifted over the years due to modifications of the detector voltage. The used combination of channels covers an energy range which can be

---

[7] A description of phoswich detectors can be found at `http://www.detectors.saint-gobain.com/Media/Documents/S0000000000000001004/SGC_Bicron_Brand_Phoswich_Configurations.pdf`

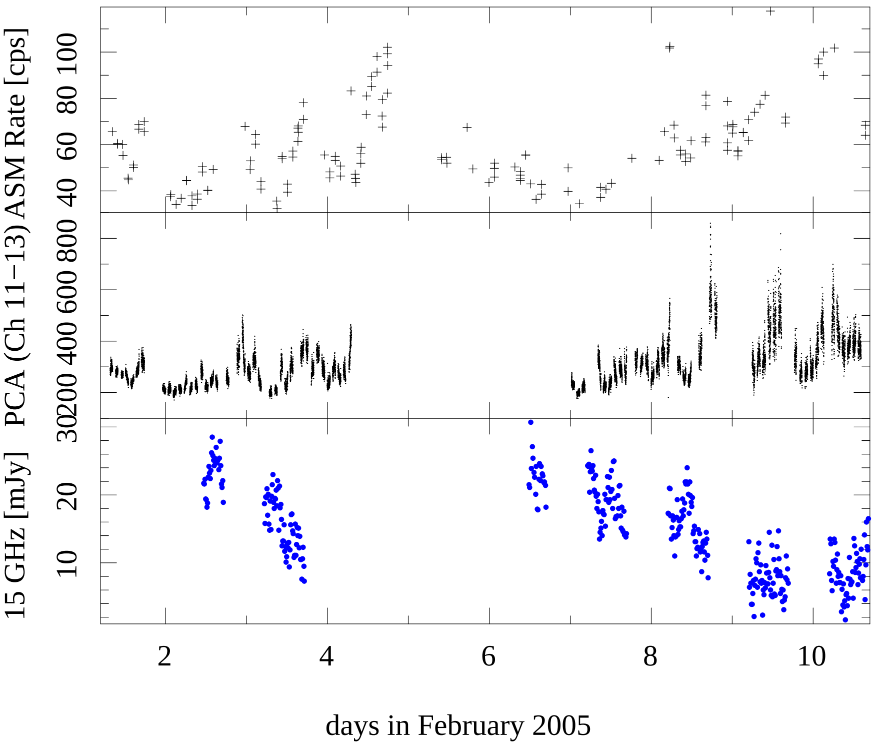

Figure 3.6: The data which were analyzed in this work. Almost 10 days in February 2005 are covered. The *RXTE* ASM light curve in the top panel illustrates the variability in the energy band 2–12 keV of Cyg X-1 in that period of time. In the second panel a PCA light curve is shown. PCA and HEXTE observations were performed simultaneously. The bottom panel shows the radio data, which was obtained with the Ryle Telescope at 15 GHz.

considered well in all PCA epochs[8]. For the timing analysis both light curves of a block were also extracted with a high time resolution of 2 ms. For the spectral analysis and creation of hardness intensity diagrams (Sect. 4.2.1) a time resolution of 16 s was used.

A typical observation is shown in Fig. 3.7. It can be seen clearly that the total counts of PCA are interupted periodically. The reason is the 90 min orbit of the satellite. For that reason Cyg X-1 cannot be observed continuously. Due to its orbit in an altitude of 580 km and an inclination of 23°, *RXTE* has to fly through the South Atlantic Anomaly (SAA). This is a region located over South America and the south Atlantic in which the background radiation is very high, due to the shape of the Earth's magnetic field. In order to avoid damaging the detectors, they are switched off while the satellite crosses the SAA. Due to contamination with radiation it is necessary to wait for a certain time to get unaffected data. In this work a SAA exclusion time of 15 minutes was applied. The crossing of the SAA and the satellite's orbital movement split the observation into blocks, which are characterized by good time intervals (GTIs). For the extraction of spectra and light curves only data within these intervals are considered. The GTIs can have further gaps due to background effects. Fig. 3.7 indicates that the count rates of the blocks can vary strongly from one to another, but also within a single block. As the spectrum of the X-ray emission changes commonly with the count rate, it was decided in this work to extract spectra for single *RXTE* orbits, i.e. a spectrum for each block instead of one for a total observation. As a result 78 blocks with an exposure time of about 3 ks in each case were obtained. Some additional blocks were not

---

[8] The energy range of the PCA channels during the epochs is listed at: `http://heasarc.gsfc.nasa.gov/docs/xte/e-c_table.html`

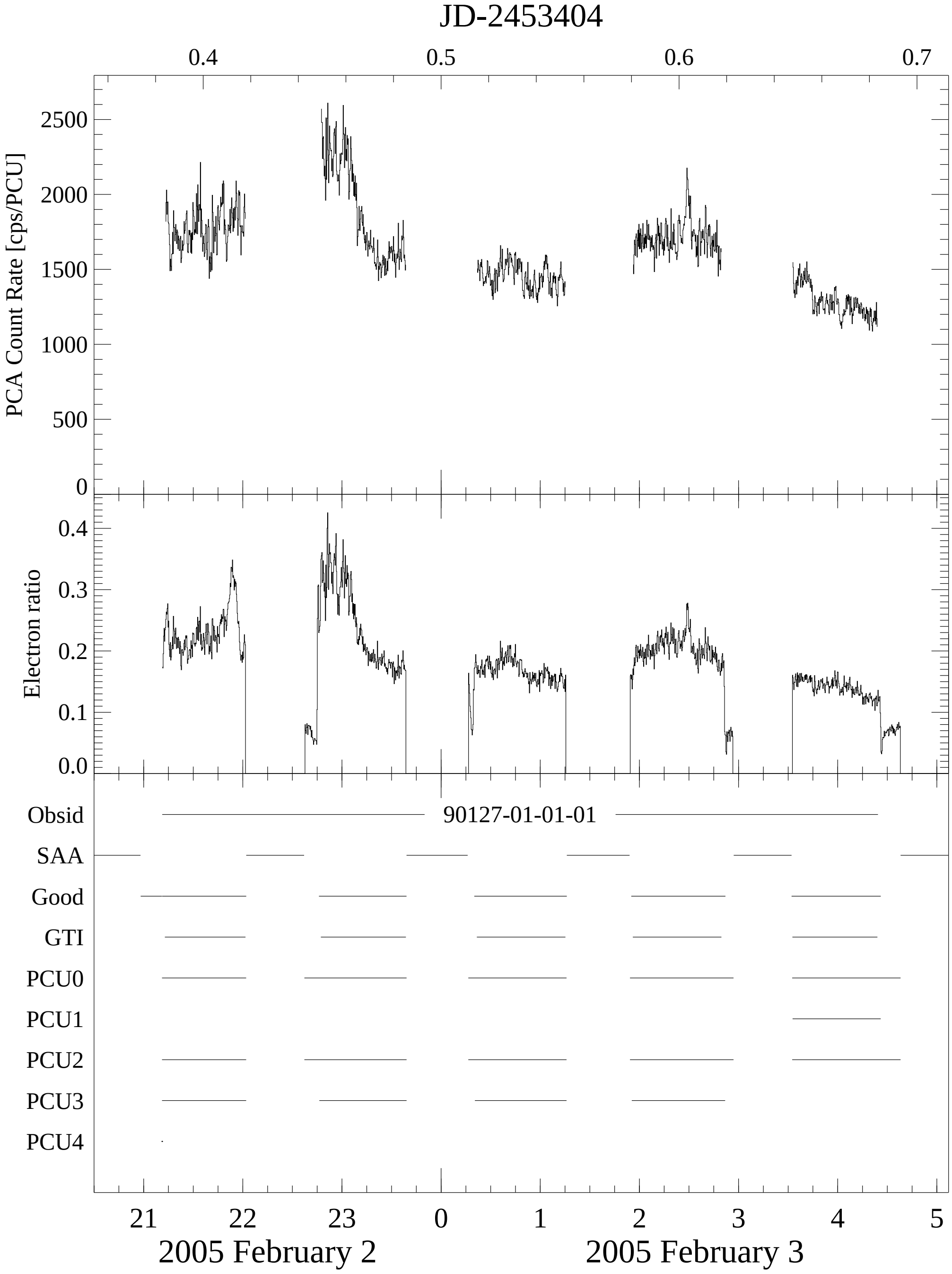

Figure 3.7: Typical observation of Cyg X-1 with PCA. The top panel shows the total (integrated over all energy channels) count rate of PCA per PCU. It is indicated by dashes in the bottom panel when which PCU was active. No measurements were performed while *RXTE* passes the South Atlantic Anomaly. The GTI is the good time interval, the time in which good data were obtained.

taken into account as no timing was analysis was possible, because the exposure was too small. For each block a single spectrum was extracted.

3.4 Data Analysis

In this section the analysis of X-ray spectra is explained briefly, a very detailed description is given by Hanke (2007, Sect. 2.2). The extration of spectra from the satellite data yields count rates in the energy bins. It will be discussed in the following, how these count rates are related to the source flux and in which way the analysis is performed.

3.4.1 Binned Spectra

A direct measurement of the X-ray spectrum of the observed source is not possible, due to the functioning of a detector. At first the spectral resolution of the detector is binned and secondly the count rate in a bin differs from the real flux in that energy band. A reason for the binning is the limited precision of the detector's spectral resolution and the fact that the telemetry is limited as well. In order to understand the difference between the measured count rate and the real flux, it is illustrative to consider the following equation:

$$C_D(i) = C_B(i) + t_{\text{exp}} \int_0^\infty R(i,E) \cdot A(E) \cdot F_S(E) dE \tag{3.2}$$

where $C_D(i)$ are the detector counts in the ith bin $B_i = [E_i, E_{i+1}]$, $C_B(i)$ are counts caused by background events and t_{exp} is the exposure time of the observation. The integrand consists of the flux spectrum $F_S(E)$ originating from the source, the redistribution matrix function (RMF) which is noted as $R(i,E)$ and the ancillary response function (ARF) $A(E)$. The RMF $R(i,E)$ gives the probability that a photon with energy E causes an event in the detector bin B_i. The ARF is mainly the effective area of the detector, but also includes additional detector effects. For an ideal detector with a continuous spectral resolution ($E_{i+1} - E_i \to 0$) the RMF $R(i,E)$ would be a delta function $\delta(E_i, E)$. The RMF of a real detector takes into account that there can be photon escape, i.e., that a photon ionizes an atom in the detector and is thus measured as a photon of lower energy. The recombination photon can be measured again, but this has a strong effect on the measured spectrum anyway.

3.4.2 Fitting Spectra

Knowing the count rates of the detector $C_D(i)$ the flux spectrum originating from the source $F_S(E)$ cannot be obtained easily, but depends on the structure of the response function (RSP = RMF·ARF) of the detector. Commonly this deconvolution is not possible, even if the response of the detector is well known. A convenient method to figure out the initial source flux is a χ^2-minimization approach. In doing so a model flux spectrum $F_M(E)$ is considered and the corresponding count rates are calculated, i.e., how the detector would measure it:

$$C_M(i) = t_{\text{exp}} \int_0^\infty R(i,E) \cdot A(E) \cdot F_M(E) dE \tag{3.3}$$

The obtained count rates are compared with the measurement of the source $C_S(i) = C_D(i) - B(i)$. The model is varied until the difference between the count rates is minimal. To find a model which reproduces the spectrum of the source very well it is necessary to know the RSP in detail, for that purpose there is a calibration team for each detector. In addition the difference between model and data count rate has to be qualified, hence the value $\chi^2 =$ is introduced, which is defined as the squared deviation of the count rates in units of the error summed over all detector bins i:

$$\chi^2 = \sum_i \left(\frac{C_S(i) - C_M(i)}{\sigma_i} \right)^2 \tag{3.4}$$

Usually the error $\sigma_i = \sqrt{C_D(i)}$ is assumed if the count rate is high enough, due to Poisson statistics. The value of χ^2 increases with the number of bins, thus the quality of a fit is mostly evaluated by

χ^2_{red}, which can be obtained by dividing χ^2 by the degrees of freedom, namely the number of bins minus the number of varied fit parameters. For a good fit the difference of data and model in a bin is comparable to the error σ, thus χ^2_{red} is close to 1.

With a model fitting the data very well the original flux spectrum is reproduced. The target is of course to find models explaining the measured emission of the source with physical processes. Such models, as for example a Comptonization and a jet model are described in Sect. 4.1. As the χ^2-minimization process can be really complicated depending on the number of parameters of the model , programs like XSPEC (Arnaud et al., 2007) or ISIS (Houck, 2002) are applied. In this work the spectra and the power spectra (Sect. 5.2.1) were fitted with ISIS 1.4.9. The fitting process runs in the following way, at first a fit model is defined, which depends on a set of parameters $\{p_1, p_2, ...p_N\}$. Substituting $F_M(E; p_1, p_2, ...p_N)$ into Eq. 3.3 the corresponding count rates could be calculated. To reduce the computation time it makes sense to use the integral of the model instead of performing complicated integrations at each fitting step. This can be done by approximating that the response function is constant on certain energy bins $\mathrm{bin}_j = [E'_j, E'_{j+1}]$ and thus Eq. 3.3 can be transformed into:

$$C_M(i; p_1, p_2, ...p_N) = t_{\mathrm{exp}} \sum_j \mathrm{RSP}(i,j) \int\limits_{\mathrm{bin}_j} F_M(E; p_1, p_2, ...p_N) dE \qquad (3.5)$$

For that reason only the integral of the fit functions, which depends on the borders of the bins and the parameters, is implemented into XSPEC and ISIS. It is of course possible to use the sum of different fit functions as a model. Besides bin-integrated models there are also bin-averaged fit functions, which are multiplicative models, such as a high energy cutoff or absorption models. The models used in this work to fit the spectra are described in Sect. 4.1. The fit functions used for the power spectral densities are explained in Sect. 5.2.2. After calculating the model count rates, χ^2 is computed, which is a function of the set of parameter. The minimization of the χ^2 is in general very complicated for a large number of parameters. In ISIS several minimization algorithms are provided, such as the Marquardt or the Nelder-Mead simplex algorithm (see Hanke (2007), Sect. 2.2.2 and the references therin).

The errors of the best fit parameters, which are noted in this work, are the 90% confidence intervals. This interval is defined in the following way: If the parameter is fixed to a value within its confidence interval, the χ^2 of the best fit, which can be obtained by varying the other parameters, is at least 2.705543 worse than the total best fit. A detailed explanation of confidence levels is given by Hanke (2007, Sect. 2.2.2) and the references therein.

Chapter 4

Spectral Analysis

The main issue of this work was to analyze the behavior of the source Cyg X-1 on time scales of days. Its long-term spectral evolution from 1999 to 2004 has been studied by Wilms et al. (2006). Their work revealed correlations between parameters of the models describing the observed spectra and it was found that Cyg X-1 spent time in different states, which were identified as soft, hard and intermediate state. This study covered a long period of time, but the source was observed about every two weeks and thus a continuous transition between the states was not studied.

The data available for this work cover about 10 days in February 2005 and consist of 78 observations with an exposure time of 3 ks in each case. Thus the behavior of the Cyg X-1 and the changes in the fitting parameters can be analyzed quasi-continuously with a high sampling. The fitting models, the results of the analysis and a comparison with that of the long-term evolution is discussed in this chapter.

4.1 Fit Functions

For the analysis PCA data between 4 and 20 keV and HEXTE data in the energy range 20–200 keV are considered. The X-ray spectra were fitted with different models which were discussed in the following. This phenomenological model describes the data with the spectral hardening above 10 keV quite well. A multiplicative constant was used to adapt PCA and HEXTE normalization.

4.1.1 Components

Absorption To model the photo-electric absorption the fit function *phabs* was used, which can be written in the very simple form:

$$A(E) = \exp\left(-N_\mathrm{H} \cdot \sigma(E)\right) \tag{4.1}$$

where N_H, the equivalent hydrogen column, is the only fitted parameter of this function. Thomson scattering is not included in the photo-electric cross-section $\sigma(E)$, but is is possible to change the relative abundances. Fig. 4.1 shows the absorption fraction as a function of the energy for different values of N_H.

Iron Line The Fe Kα line is important in X-ray astronomy (see Sect. 2.3.2). From its detailed shape many information can be obtained. To do so with PCA data is very limited, as its resolution is about 0.4 keV. For that reason it is sufficient to model the relativistically broadened iron line with a simple Gaussian profile:

$$G(E) = \frac{A}{\sigma\sqrt{2\pi}} \exp\left[-\frac{(E-E_0)^2}{2\sigma^2}\right] \tag{4.2}$$

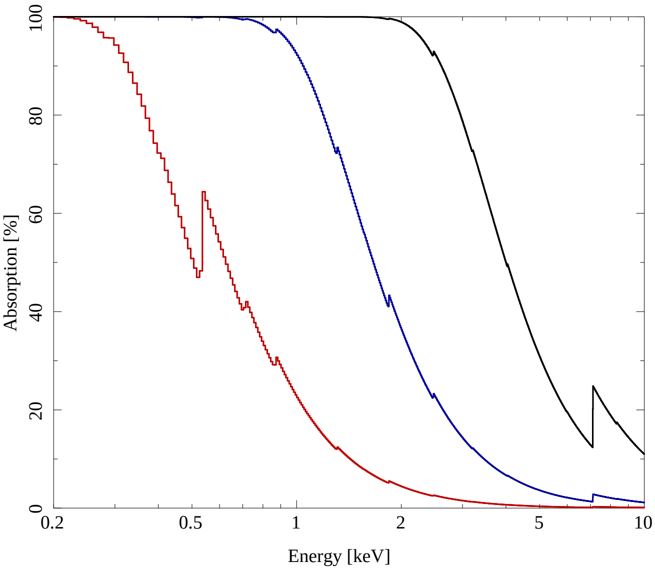

Figure 4.1: Illustration of the photoelectric absorption as it is modeled by the *phabs* function. The graphs correspond to different values of the equivalent hydrogen column N_H in units of $10^{22}\,\mathrm{atoms/cm^2}$. For the red graph a N_H of 0.1 was used, 1 for the blue one, and 10 for the black one. Typical values for Cyg X-1 are about 0.5–0.6, thus it is obvious that the PCA data above 4 keV are hardly absorbed.

where A is the total area under the Gaussian profile (the total line flux) in units of photons/s/cm^2, σ is the width in keV and E_0 is the center of the Gaussion profile.

Accretion Disk The black body radiation of the accretion disk contributes strongly to the soft X-ray emission. Especially during soft states this thermal component is important. As mentioned in Sect. 2.3.1 the temperature in a thin accretion disk depends on the radius R and is proportional to $R^{-3/4}$. This distribution of temperatures yields a total spectrum similar to a stretched one of a black body. A simple model describing such spectra is called *diskbb* (Mitsuda et al., 1984; Makishima et al., 1986). Only two parameters are required for this model, namely the temperature at the inner radius T_in in keV and a normalization parameter K, which takes the distance of the source d, the inclination of the disk θ and its inner radius R_in into account: $K = ((R_\mathrm{in}/\mathrm{km})/(d/10\,\mathrm{kpc}))^2 \cdot \cos(\theta)$. The distance of Cyg X-1 is about 2.5 kpc (Sect. 2.5) and the orbital inclination of the system is assumed to be about 35°, but the inclination of the accretion disk is not determined exactly. There are indications that the disk is not coplanar with the orbital plane (see Sect. 5.1.2). Beside these uncertainties there is a larger problem, which makes detailed interpretations of the fit parameters of this model obtained in this work difficult. Only energies above 4 keV are considered in the spectral analysis, whereas for Cyg X-1 temperatures at the inner radius smaller than 1 keV are usually found. For that reason only the high energy part of the disk emission effects PCA data, thus it is not possible to determine the fit parameters exactly. In addition photoabsorption affects soft X-rays, which contributes to the uncertainty of the fitting results of the disk. To some extent it is possible to obtain similar fits by increasing or decreasing the disk emission and the absorption simultaneously by corresponding values.

Broken Power Law A broken power law is only a phenomenological model, which describes no physical process. The fit function *bknpower* has the following simple form:

$$P_\mathrm{bkn}(E) = \begin{cases} K \cdot (E/1\,\mathrm{keV})^{-\Gamma_1} & \text{for} \quad E \le E_\mathrm{br} \\ K \cdot E_\mathrm{br}^{(\Gamma_2-\Gamma_1)} \cdot (E/1\,\mathrm{keV})^{-\Gamma_2} & \text{for} \quad E > E_\mathrm{br} \end{cases} \tag{4.3}$$

where K is the flux at 1 keV, a normalization factor in units of photons/keV/s/cm^2. The photon index Γ_1 is the exponent at energies smaller than the break energy E_br and Γ_2 is that at higher energies.

High Energy Cutoff A high energy cutoff is given by the multiplicative fit function *highecut*. It describes an exponential cutoff above a certain value. The function has the simple form:

$$C_{\mathrm{cut}}(E) = \begin{cases} 1 & \text{for} \quad E \leq E_{\mathrm{cut}} \\ \exp((E_{\mathrm{cut}} - E)/E_{\mathrm{fold}}) & \text{for} \quad E > E_{\mathrm{cut}} \end{cases} \tag{4.4}$$

The two required parameters are the cutoff energy E_{cut} in keV and the exponential folding energy E_{fold} in keV.

Comptonization The model *comptt* by Titarchuk (1994) describes the Comptonization of soft photons in a hot plasma. Relativistic effects are included. In this model the spectrum of the soft photons, which are called seed photons, is described by a Wien distribution law. In this case a analytic solution is possible. The physical assumptions are explained by Titarchuk (1994), Hua & Titarchuk (1995) and Titarchuk & Lyubarskij (1995). Important parameters of the model are the plasma temperature with possible values between 2 and 500 keV, the optical depth of the plasma and the temperature of the seed photons. There is also a normalization parameter, a parameter describing the redshift, which was fixed to zero in this work[1], and a geometry switch. A disk and a sphere are the possible geometries. Here, the disk was used, but no significant difference in the quality of the fits was found between both cases.

Reflection The Compton reflection hump can be modeled using the *reflect* fit function. It describes the reflection of hard X-rays from material in the disk (Magdziarz & Zdziarski, 1995). The high energy photons are Compton downscattered. This model is a convolution model. It requires another fit model, the emission of which is reflected. One parameter of the model is the reflection scaling factor. Its value determines the reflected fraction. There is a redshift parameter, which was fixed to 0, as for the Comptonization model, and it is possible to change the abundances of elements heavier than helium. It is possible to change the iron abundance seperately. The fifth parameter of the *reflect* model is the cosine of the inclination angle of the disk.

4.1.2 Total Fit Models

The models which are used to fit the spectra are a combination of the components described above.

Broken Power Law For the broken power law fits the following fit function is used:

*phabs(1)*constant(Isis_Active_Dataset)*(bknpower(1)*highecut(1)+egauss(1)+diskbb(1))*

The number in brackets after each component is its id parameter, as several components can be applied more than once, for example multiple Gaussian profiles are allowed in one model. The main component of the model noted above is the broken power law with exponential cutoff at high energies, which describes the continuum spectrum. In addition there is a Gaussian line profile modeling the Fe Kα line, and the *diskbb* model describing the thermal emission of the accretion disk. Photo-electric absorption is used for the whole model. The *constant* function normalizes the data obtained with different detectors to each other. This is necessary due to problems with the exact calibration of the detectors, which have different responses. Fig. 4.3 shows the components of this fit model.

Comptonization Model The Comptonization model is similar to the model described above:

*phabs(1)*constant(Isis_Active_Dataset)*(comptt(1)+reflect(1,comptt(1))+egauss(1)+comptt(2))*

---

[1] No significant redshift of the spectral lines in the emission of Cyg X-1 was observed.

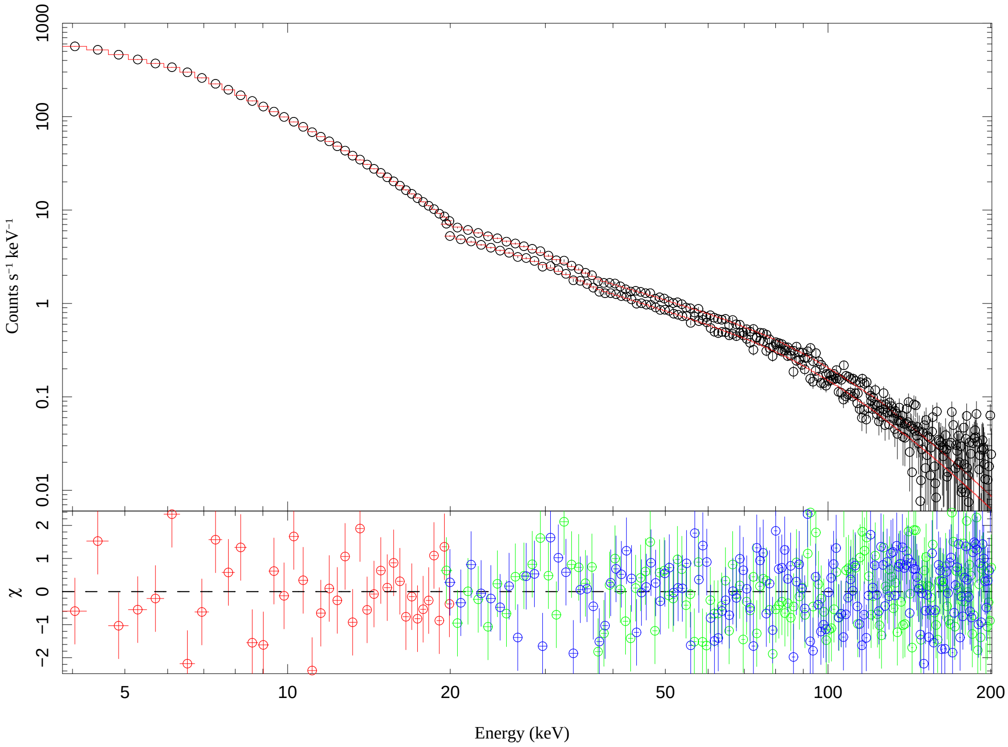

Figure 4.2: The black circles correspond to the background subtracted count rates of an observation on February 3, 2005 from 06:49:04 to 07:30:56 UT. PCA data reach from 4–20 keV, whereas data above 20 keV were obtained with HEXTE A and B. The red lines are the model count rates. The bottom panel shows the residuals, the difference between data and model, in units of σ (see Sect. 3.4.2).

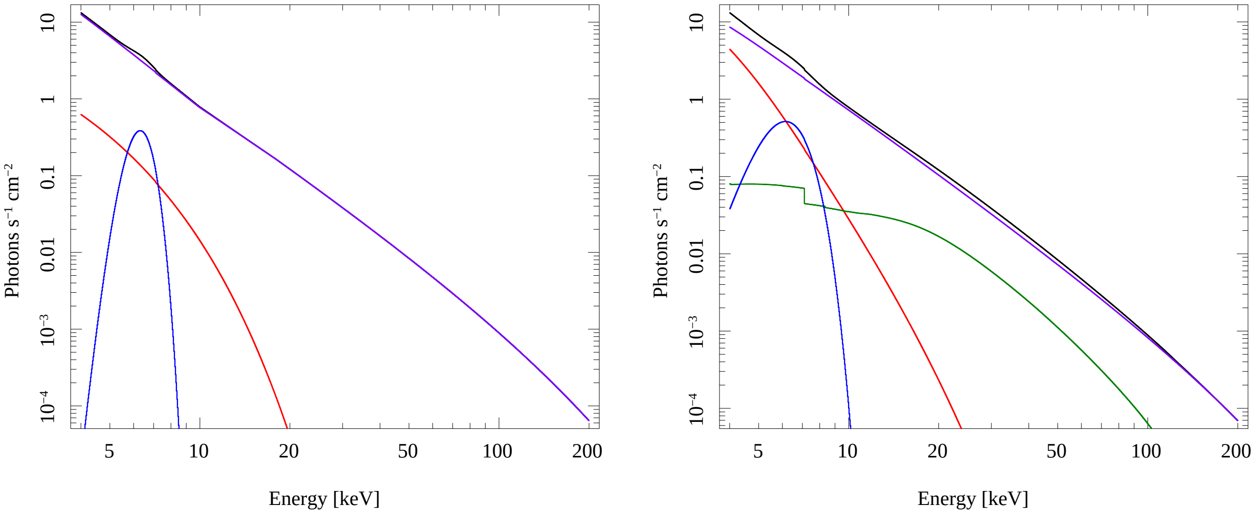

Figure 4.3: The left plot shows the broken power law model which was used in Fig. 4.2. The purple component is the absorbed broken power law with high energy cutoff, the blue component is the iron line and the red one the thermal emission of the accretion disk. A fit of comparable quality can be achieved with a Comptonization model, which is shown on the right side. The iron line is again shown in blue, the Comptonization component in a hot and optically thin plasma is illustrated in purple. The red line corresponds to the cooler and optically thicker plasma and the Compton reflection is shown in green.

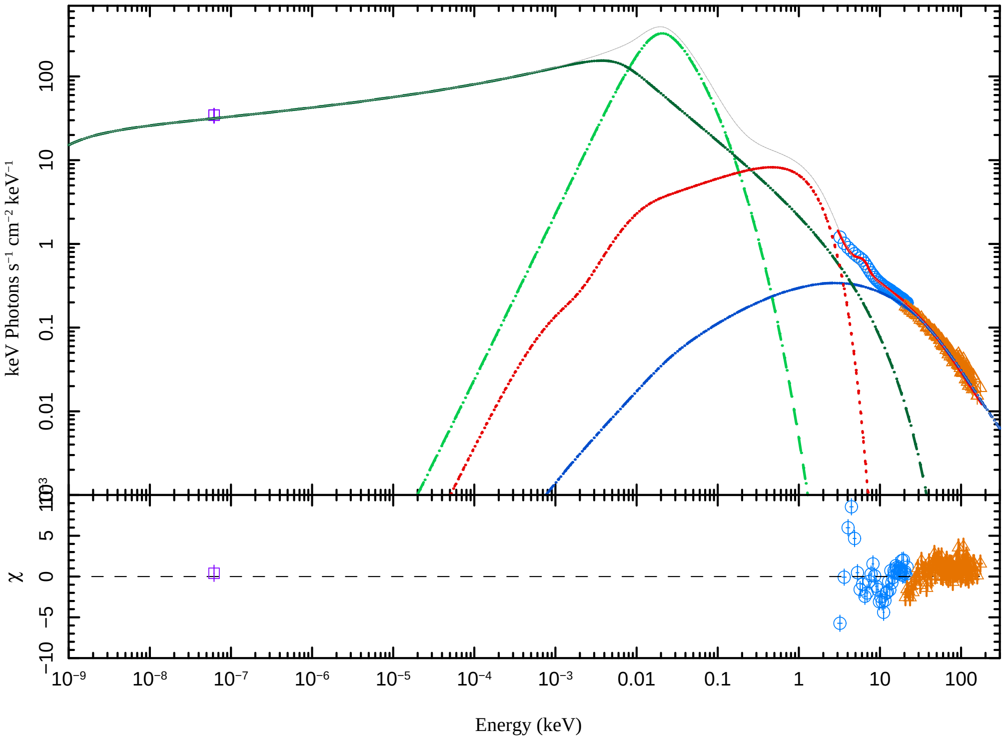

Figure 4.4: A fit with the jet model to the data shown in Fig. 4.2 and radio data which was obtained simultaneously. The component shown in red is the thermal emission of the accretion disk, the dark green one is the synchrotron emission of the outer jet. That of the inner jet is shown in bright green. The component at high energies, which is shown in blue, corresponds to External Comptonization and Synchrotron Self-Comptonization.

The difference is that the continuum is modeled by Comptonization in a hot optically thin plasma and a reflection component. It is possible to replace the thermal disk emission with Comptonization in optically thick plasma which is cooler than the first one. Both variants have been tried in this work with similar result. The contribution of the components to the total model is shown in Fig. 4.3.

Jet Model Besides the broken power law and the Comptonization model, it is also possible to describe the data with a jet model. The corresponding fit function reads as follows:

*(phabs(1)*constant(Isis_Active_Dataset)*reflect(1,(agnjet(1)+gaussian(1))))*

In this fit function the reflected components are only substituted in the *reflect* model and are not added separately. In this case the complete spectrum is calculated and the reflection is not calculated separately, due to computation time as the jet model is very complicated. A detailed explanation of this model is given by Markoff et al. (2005). The model requires more than 20 parameters[2], but some of them can be fixed to certain values. For example the mass of the BH, that of Cyg X-1 was determined in the scope of other works. The *agnjet* was developed in order to model the spectrum of a BH throughout a large range of wavelengths, namely from radio waves to X-rays. The contribution of the components, which were included in this model, to the total emission are shown in Fig. 4.4.

---

[2] On `http://staff.science.uva.nl/~dmaitra/jets/report_20070312/` the parameters of the jet model are listed and it is shown how changes of their values affect the resulting spectrum.

4.2 Results

4.2.1 Transition

The long-term variability of Cyg X-1 between 2–12 keV is shown in Fig. 4.5 using the *RXTE* ASM data since 1996. As mentioned in Sect. 3.2.1 ASM is an excellent tool for monitoring the long-term behavior of X-ray sources due to the fact that usually there are several observations of a source per day. Plotting the mean count rates of each observation as a function of time yields the light curve shown in Fig. 4.5. The comparison of the data analyzed in this work with the total data illustrates that the analyzed data covers a relatively active phase of Cyg X-1, in which no typical hard state was included. During hard states the lowest count rates of Cyg X-1 of soft X-rays are observed (e.g., Wilms et al., 2006). To obtain a better overview in which state Cyg X-1 was during this period of time it is helpful to consider a hardness intensity diagram (HID). Here the count rate (intensity) is plotted against the hardness. Such a diagram corresponds to a Hertzsprung-Russel diagram, where the luminosity is shown as a function of the color of a star. The color is related to the temperature of stars, as their spectrum can be approximated as that of a black body. The "color" of the X-ray emission corresponds to a hardness ratio, i.e., as the ratio of the count rate in a high energy band cps_H to that in a low energy band cps_L. Instead of the ratio $\mathrm{cps}_H/\mathrm{cps}_L$ often the ratio $(\mathrm{cps}_H - \mathrm{cps}_L) / (\mathrm{cps}_H + \mathrm{cps}_L)$ is used, which yields a similar result. Fig. 4.6 shows a HID using all ASM data since 1996. The used hardness is the ratio between the 5–12 keV count rate to that in the energy band 1.5–3 keV. The HID reveals that there are two regions distinct from each other, which are covered more frequently with data of Cyg X-1. The region with a larger hardness is identified with the hard state, whereas the soft region with the soft state. Based on the HID an exact classification is not possible, as there is only a vague resemblance between this HID and the "q-diagram" (Fig. 2.10). States such as the hard intermediate or the soft intermediate state are not clearly identifiable. The reason for the different HIDs is that for Cyg X-1 no complete run through the whole "q" has been observed up to now. An approximate, more detailed differentiation of the HID into different states is proposed by Fender et al. (2006). It is shown in Fig. 4.7. The data analyzed in this work cover the region between the typical hard and the typical soft state of Cyg X-1. This is the interesting region, the transition region. As the properties of hard and soft states are different, there must be a more or less continuous transition between these states.

Using the PCA data the transition can be investigated with a high sampling rate. Fig. 4.8 shows a hardness intensity diagram with a time resolution of 16 s. The used energy bands are the high (9.5–15 keV) and the low (4.5–5.8 keV) energy band. This HID reveals the two different regions more clearly than the ASM data. Up to a certain time the data cover only the hard region, which corresponds to the hard state or the hard intermediate state. This holds up to an observation ending at MJD $\approx$ 53409.625. The spectra are significantly softer from the next observation on, which started about 135 min later (at MJD $\approx$ 53409.719). During the 10 days of observation this was the only clearly visible transition. As the transition obviously occurred between two observations its duration cannot be determined, but there is an upper limit. It is interesting that state transitions take less than a few hours. A full transition from the hard to the soft state of Cyg X-1 has not been observed before with such a high sampling rate. A chronological sequence including the hardness and the PCA count rate is shown in Fig. 4.10. Here, the radio data are also shown. The radio flux does not exceed 30 mJy and decreases after the transition. No radio flare was observed. Wilms et al. (2007) found a radio flare which lagged an X-ray flare by about 7 minutes, as Cyg X-1 was close to a transition from the hard to the soft state. The observed peak radio flux was about 70 mJy. In the data analyzed here a full transition occurs, which is followed by an increased X-ray flux. Unfortunately no radio data were available in the corresponding period of time. It seems that there is correlation between the hardness and the radio flux, which is similar to the strong correlation between the radio flux and the X-ray flux between 10 and 50 keV found by Wilms et al. (2006). The reason is that large flux in this energy range is tied to a hard spectrum.

To figure out detailed changes in the X-ray emission the spectra are fitted with a broken power

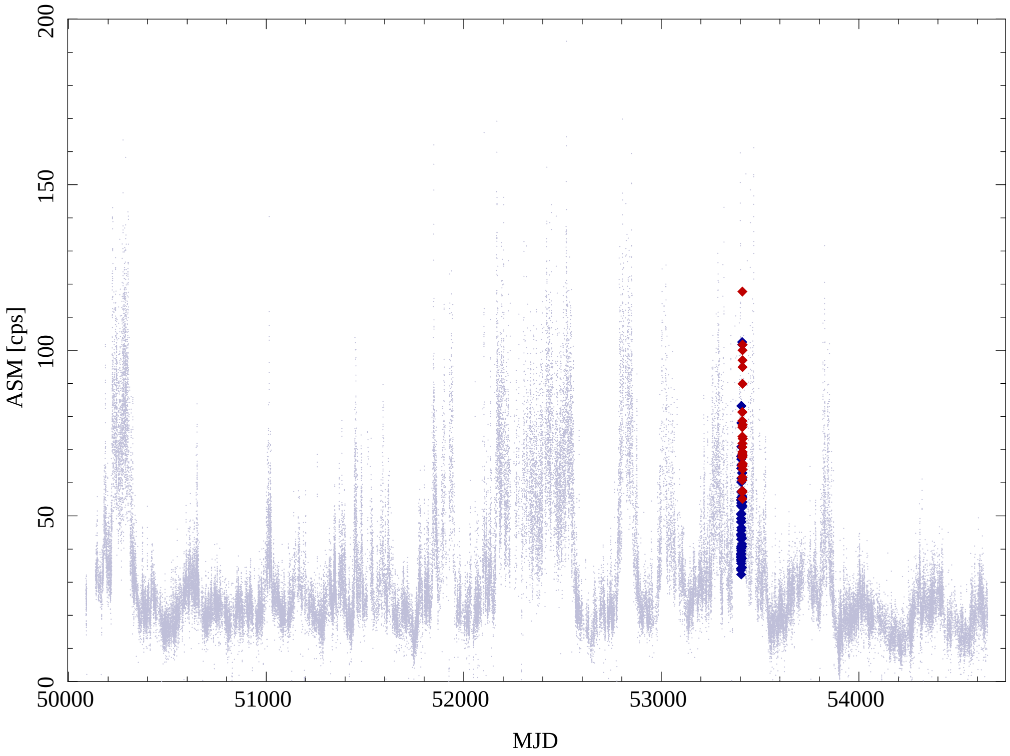

Figure 4.5: A light curve using all data (small gray dots) since 1996 obtained with *RXTE* ASM. The data analyzed here are shown with red and blue symbols. Blue corresponds to data obtained before a transition from hard to soft state, whereas red to that of the soft state (see Fig. 4.8). The transition which was found in this work will be discussed in this section.

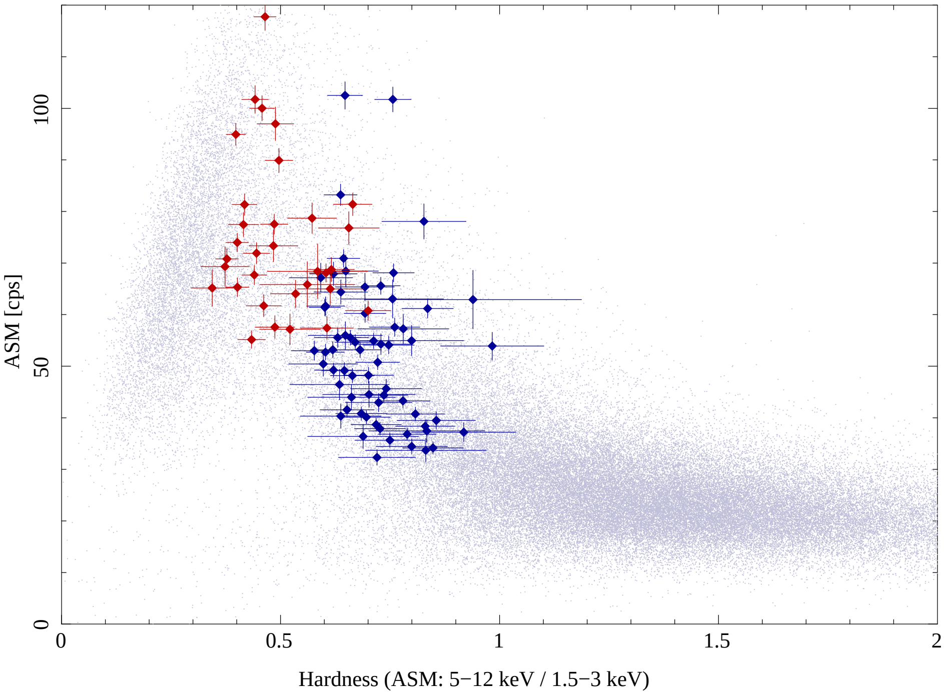

Figure 4.6: A hardness intensity diagram using all data (small gray dots) since 1996 obtained with *RXTE* ASM. The same colors as in Fig. 4.5 are used here, indicating the analyzed data(red and blue symbols with error bars), which cover the transition region. This is the region between the two areas where a accumulation of dots is found.

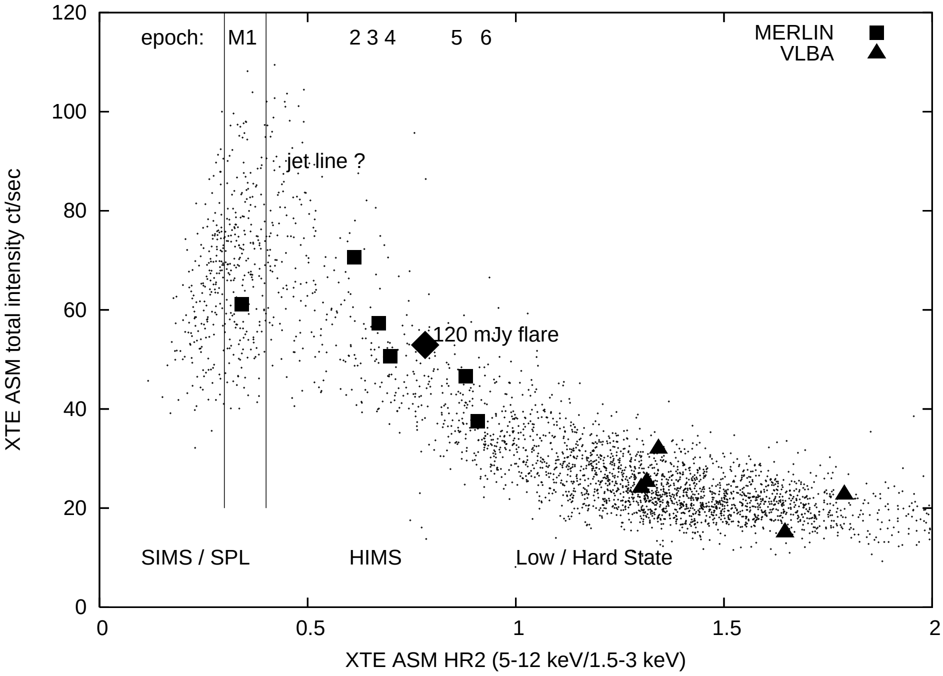

Figure 4.7: The same hardness intensity diagram of Cyg X-1 by Fender et al. (2006) (Fig. 5), using the daily average of the ASM count rates. The diagram includes their proposed classification of the states, namely the hard state, the hard intermediate state (HIMS), and a soft intermediate state (SIMS) or steep power law state (SPL). In addition radio data are shown, which were obtained with the VLBA (see Sect. 3.1) and the Multi-Element Radio Linked Interferometer Network (MERLIN, see: http://www.merlin.ac.uk/).

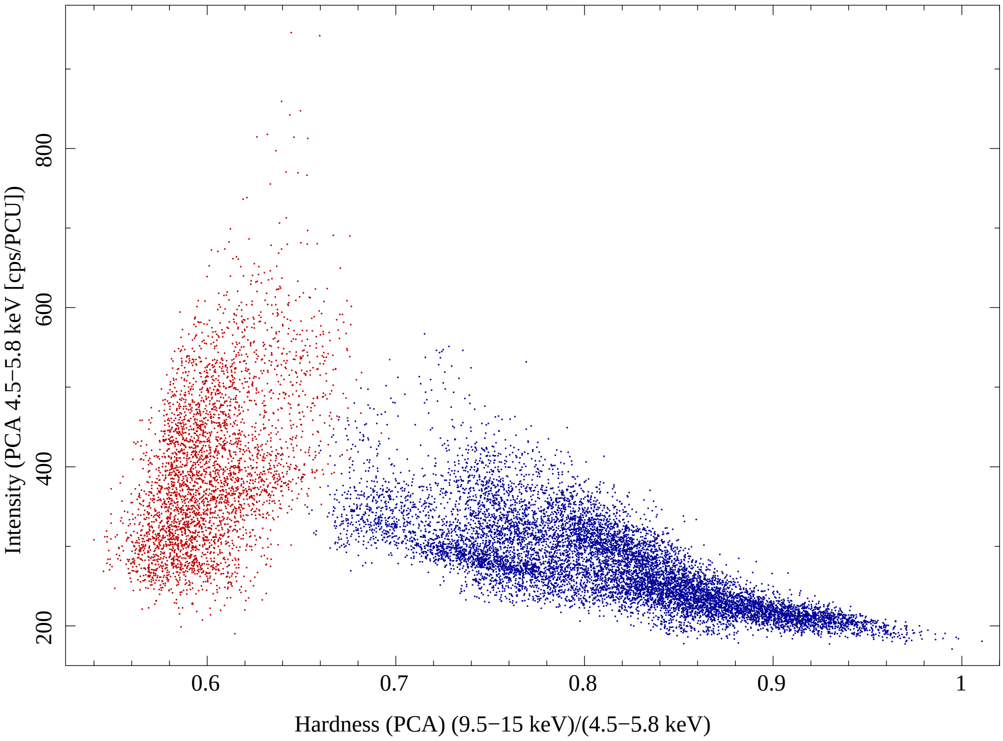

Figure 4.8: A HID using the PCA data analyzed in this work. The two different regions can be seen more clearly than in Fig. 4.6. From one observation to the next one Cyg X-1 changed its state. The data obtained before MJD = 53409.7 is colored in blue, whereas data obtained later is shown in red and corresponds to the soft state.

law model. The temporal behavior of the important fit parameters is illustrated in Fig. 4.10. The photon indices $\Gamma_{1,2}$ are the most important values, as they characterize the slope of the spectra. The break energy of the broken power law is almost constant and varies only slightly around a mean value of 10.3 keV. The photon index Γ_1, which holds for energies smaller than the break energy, seems to be correlated with the PCA count rate in the low energy channel during the hard state. After the transition to the soft state the values of the photon indices change only slightly in the range 2.4–2.6, whereas the low energy count rate varies strongly between about 200 and 800 counts per second and PCU. This effect was already visible in the hardness intensity diagram (Fig. 4.8) due to the strong anti-correlation between hardness and the photon index Γ_1. The anti-correlation is trivial, as the hardness is defined as the ratio between the count rate in the energy band 9.5–15 keV and that in the range 4.5–5.8 keV and the photon index is the slope of the spectra in a comparable energy range (4–10 keV). A value which describes the spectral hardening above the break energy is the difference between Γ_1 and Γ_2. This value increases with Γ_1.

The parameters of the high energy cutoff do not change significantly and no clear correlations with other parameters have been found. The cutoff energy varies by a few keV around a mean value of 22.4 keV. No specific behavior of the folding energy was figured out, but it seems that its confidence levels decrease after the transition. The values of the folding energy is shown in Fig. 4.10.

As discussed above, it is difficult to determine the parameters of the accretion disk accurately by considering X-ray data above 4 keV. Despite the uncertainty of the disk parameters, it was visible that there was no evidence for disk emission during the hard state. The fitted norm parameter was close to zero. It changed after the transition, when the norm increased to values between $1 \cdot 10^4$ and $5 \cdot 10^4$. The temperature at the inner radius was then 0.3–0.4 keV. Substituting the distance of about 2.5 kpc of Cyg X-1 into the definition of the norm parameter and assuming a disk inclination of 35° yields an inner disk radius of 400 km, which is about 13 R_g, during the soft state, but due to the uncertainty of the fits and the data this is not a credible result.

Also the fit parameter of the photoabsorption cannot be determined exactly from the PCA data, because only the low energy bins are affected by the photoabsorption. The fitted equivalent hydrogen column varies between 0 and 10^{22} atoms/cm^2. For PCA data it is meaningful to fix this parameter to about 0.5–0.6. Using soft X-ray data which were obtained with other satellites, Dotani et al. (1997) determined the value $N_\mathrm{H} = (5.3 \pm 0.2) \times 10^{21}$ atoms/cm^2 from *ASCA*[3] data. Schulz et al. (2002) and Hanke et al. (2008) obtained $N_\mathrm{H} = 6.2 \times 10^{21}$ atoms/cm^2 from *Chandra*[4] data.

The PCA is not a suitable detector for measuring the spectral shape of the iron line, as its spectral resolution is not accurate enough. The corresponding energy channel has the range 6.12–6.53 keV[5]. For that reason it is convenient to fix the center of the Gaussian line profile, which is used to model the iron line to 6.4 keV that is the energy of the Fe Kα transition. In this work the center of the Gaussian line was not fixed, and a small variation around 6.35 keV was observed, which is perfectly consistent with the expected values in the scope of the energy bins. The width varies around a mean value of 0.6 keV. No dependence of the width on other parameters such as the photon index were found. The third parameter of the Gaussian profile, which is the total area under the Gaussian profile and thus gives the total line flux, is clearly correlated with the continuum flux in the corresponding energy range (Fig. 4.9). Whereas the line flux was obtained directly as a fit parameter, the norm and the photon index of the broken power law fits were used to calculate the unabsorbed continuum flux between 5.2 and 7.6 keV. The linear correlation indicates that the iron

---

[3] The Advanced Satellite for Cosmology and Astrophysics (*ASCA*) had an energy range of 0.4–10 keV and worked from 1993 to 2001 (see `http://heasarc.gsfc.nasa.gov/docs/asca/asca.html`)

[4] Information on the *Chandra* mission can be found at `http://www.nasa.gov/mission_pages/chandra/main/index.html`

[5] The energy range of the detector's channels depends on the calibration epoch. The value noted in the text holds for the period of time for in which the data analyzed here were obtained. More information on the calibration epochs can be found at `http://heasarc.gsfc.nasa.gov/docs/xte/e-c_table.html`

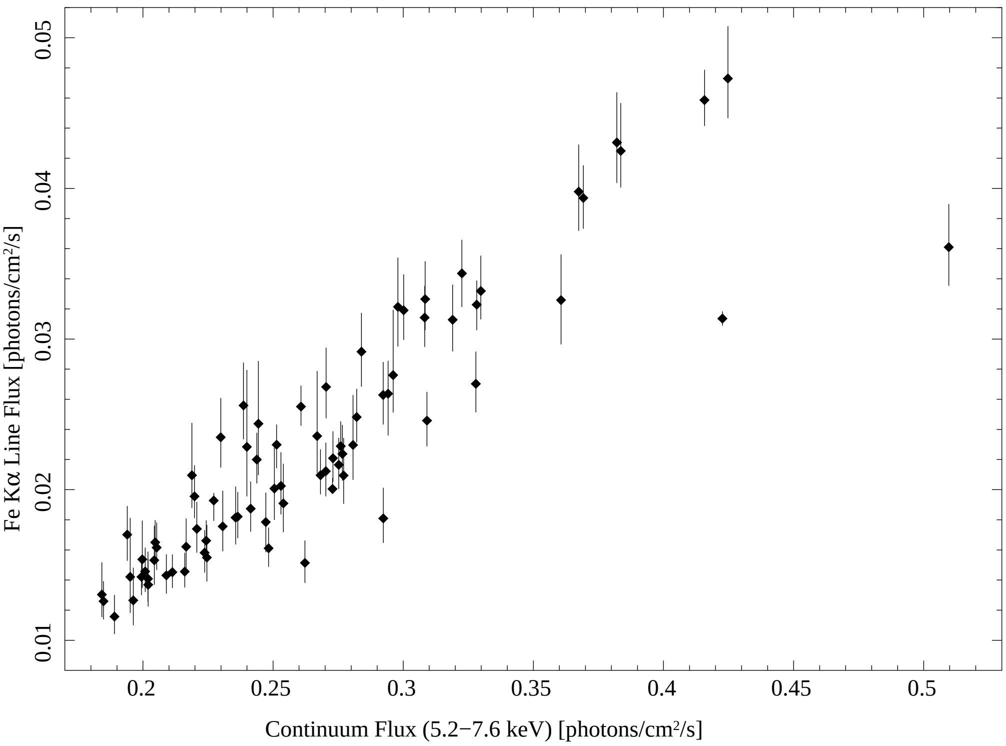

Figure 4.9: The total flux of the Fe Kα line is clearly correlated with the continuum flux at energies around 6.4 keV.

line is indeed caused by Cyg X-1 and not by another source in the field of view and that this line is caused by fluorescence.

Besides the fits with a broken power law, a Comptonization model was used to fit the data. The Comptonization fits have been performed with a lower priority than the broken power law fits and no errors of the fit parameters were calculated due to the following reasons. In the first place, when the state transition was found during the spectral analysis, it was decided that it is very interesting to figure out how the timing properties change with the transition. To find spectral-temporal correlations it was more convenient to use the phenomenological broken power law model for the spectral analysis, because it fits the data better, especially for the intermediate and soft states. It needs less computation time and it is more general to use parameters like the photon index, which describes the slope of the spectrum, for the spectral-temporal correlations than for example a plasma temperature, as it is not clear if the corresponding X-ray emission or which fraction of it is really caused by Comptonization and not by a jet or something else. Errors of the Comptonization fit parameters have not been calculated due to computation time. For a single spectrum the calculation of the confidence levels took several days. To perform such a computation for all spectra within meaningful timescales, it would have been necessary to use parallel computing. By now it is possible to use PVM (parallel virtual machine) for the error calculation at the Dr. Remeis observatory in Bamberg, but within the scope of this work the data were not synchronized there.[6] Nevertheless the obtained Comptonization fit parameters reveal an interesting behavior, although some of the fits are certainly not the best possible ones. The fit model consists of a Comptonization component with reflection in addition two another Comptonization component and a Gaussian line, which models the iron line. As described in Sect. 4.1 the first *comptt*, which is reflected, models a optically thin and hot corona, whereas the other one replaces a black body disk model and thus is optically thick and significantly cooler than the first one. The behavior of the important parameters is shown in Fig. 4.11. It can be clearly seen that the most

---

[6] The data are stored at the computing center of the university of Erlangen-Nuremberg.

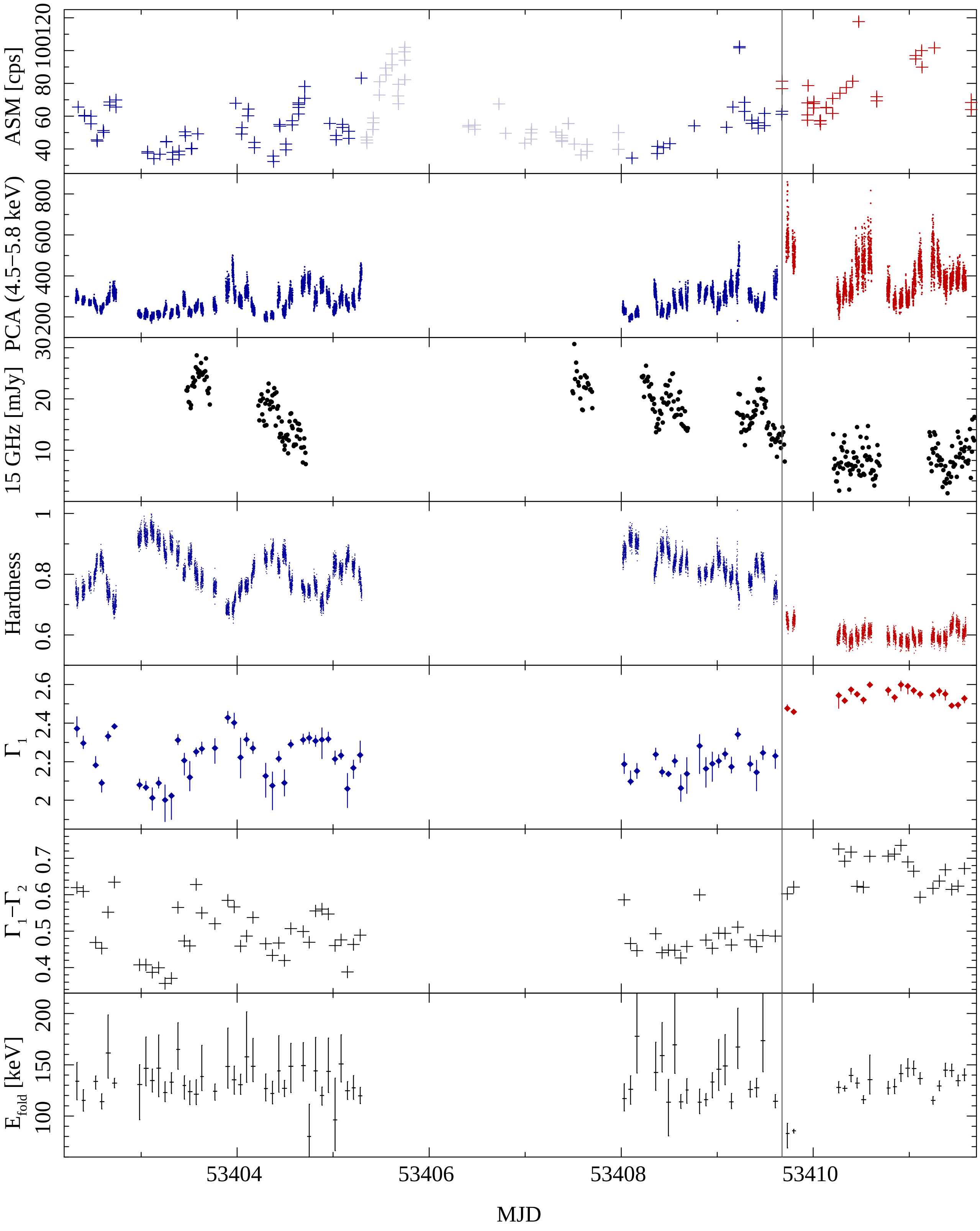

Figure 4.10: Overview of spectral parameters as a function of time. The vertical line indicates the state transition. The two upper panels show the ASM and the PCA light curves, which are colored according to the transition. The coloring of data is identical to that used in the figures 4.5, 4.6, and 4.8.

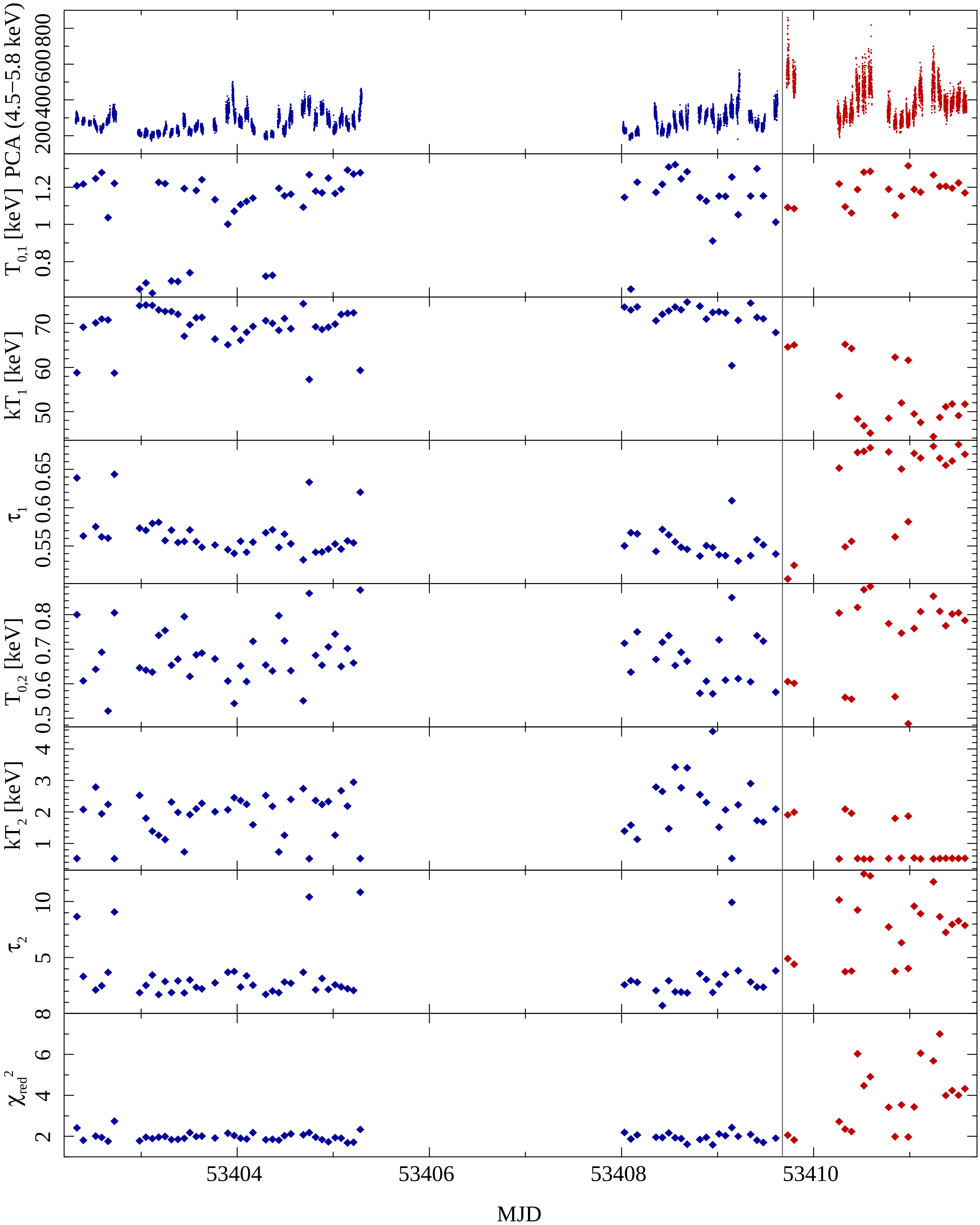

Figure 4.11: Temporal evolution of parameters obtained from the Comptonization fits. The top panel shows the PCA light curve in the low energy band, the bottom panel shows the reduced χ^2 of the fits, in between are parameters from the *comptt* model. T_0 is the temperature of the seed photons, kT that of the Comptonizing plasma and τ its optical depth. The index 1 corresponds to the optically thin and hot corona, whereas the other Comptonization component is used instead of a black body disk model.

significant changes of the parameters are tied to the transition. After the transition to the soft state the reduced χ^2 worsens sharply, indicating that Comptonization, or more precisely the used Comptonization model, does not fit the observed spectra well. Before the transition, i.e., while Cyg X-1 was in the hard or hard intermediate state, acceptable fits are possible. This confirms the assumption that the corona is sparsely extended in the soft state or at least changes its properties. Fig. 4.11 indicates that the plasma temperature of both Comptonizing components is smaller in the soft state than in the hard state, whereas the optical depth is larger. A systematic change of the temperature of the seed photons is not noticeable. The fits are, however, not good enough for any detailed predictions or constraints on the corona.

The jet model was applied only on a few exemplary spectra, in order to figure out if good fits can be obtained with this model. As not all spectra were fitted with this model no temporal evolution, characteristic changes or correlations of the fit parameters were analyzed. The reason is that the jet model needs even more computation time than the Comptonization model used here. The jet model includes a Comptonization component, which is a convolution model, and there are several dependences between its components in order to get a self-consistent model. Another point is that the jet model was developed for the hard state, in this case it is assumed that a steady jet exists, whereas in the analyzed period of time the spectrum with a photon index $\Gamma_1 > 2.1$ of Cyg X-1 was not very hard. The state source is more likely a hard intermediate state than a typical hard state. Observations with a relative hard spectrum cold be fitted with the jet model. The fits were slightly worse than that with the broken power law or the Comptonization model. In order to understand state transitions, as a reason of changes of the accretion flow and the outflow, Maitra et al. (2008) work on a time dependend version of the jet model. For example the emission resulting from ejection of blobs is expected to play an important role in this case.

4.2.2 Comparison with Long-Term Observation

Wilms et al. (2006) analyzed the long-term spectral evolution from 1999 to 2004 of Cyg X-1. They used about 200 pointed *RXTE* observations, which were not split into single orbits of the satellite, and fitted the spectra with a broken power law model with exponential cutoff, but also with Comptonization models, namely the *comptt* model, which was described above (Sect. 4.1), and the *eqpair* model (Coppi, 1999). The data cover a large range of states of Cyg X-1. Hard and soft states have been observed and several correlations have been found. It is interesting to compare these results with that of this work and search for differences and similarities between single *RXTE* orbit observations covering 10 days and that of the long-term analysis.

The figures 4.5, and 4.6 already show a comparison of the behavior of Cyg X-1 during the 10 days and that of the last years. Although the source was rather variable during the analyzed period of time and a hard and soft state were observed, only a fraction of the parameter space, which was found in the long-term analysis is covered. This can be seen clearly by considering the range of the photon indices. Fig. 4.12 shows a linear correlation between the two photon indices, which was presented by Wilms et al. (2006), where values of Γ_1 between 1.6 and 3.4 were found. In this work this range was only 2.0–2.6. The correlation between Γ_1 and Γ_2 is identical in both cases. It is interesting that the correlation holds throughout all states, whereas several other properties change significantly with the states. Wilms et al. (2006) found that in hard states, which they classified by $\Gamma_1 < 2.1$, the exponential folding energy was quite large in relation to that in soft states and thus the cutoff was less strong. The data used in this work contains no typical hard states, as Γ_1 is always larger than 2.0, and folding energies of about 130 keV were obtained. These values are consistent with that of the long-term evolution.

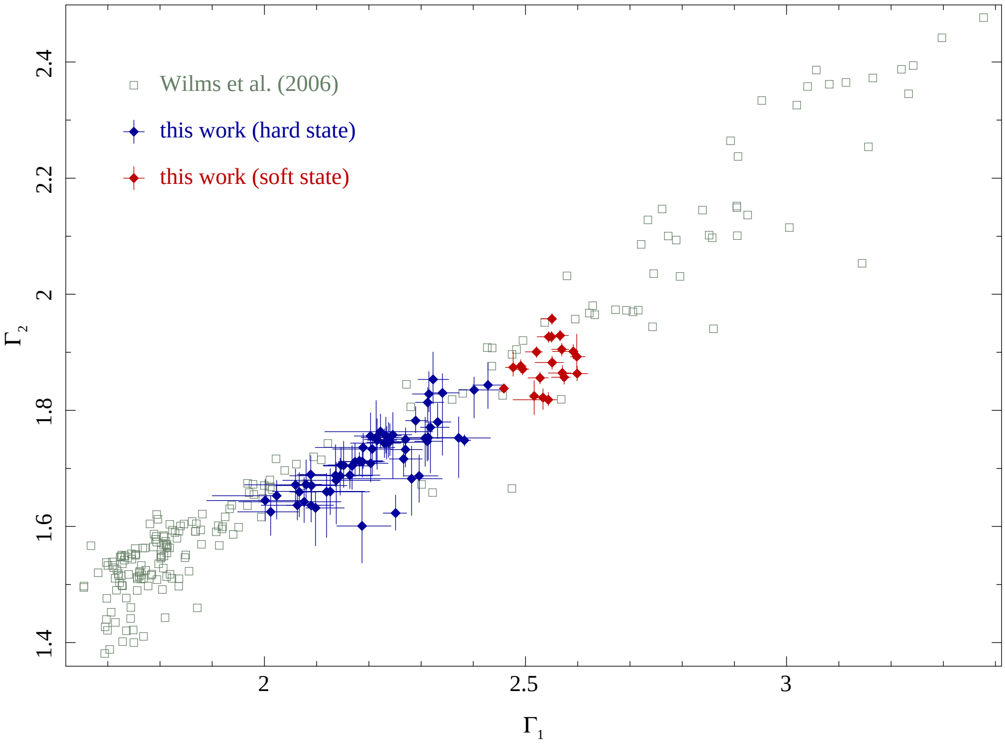

Figure 4.12: Comparison of the correlations between Γ_1 and Γ_2 obtained in this work and in the long-term analysis by Wilms et al. (2006). In both cases the same relation between these parameters is found.

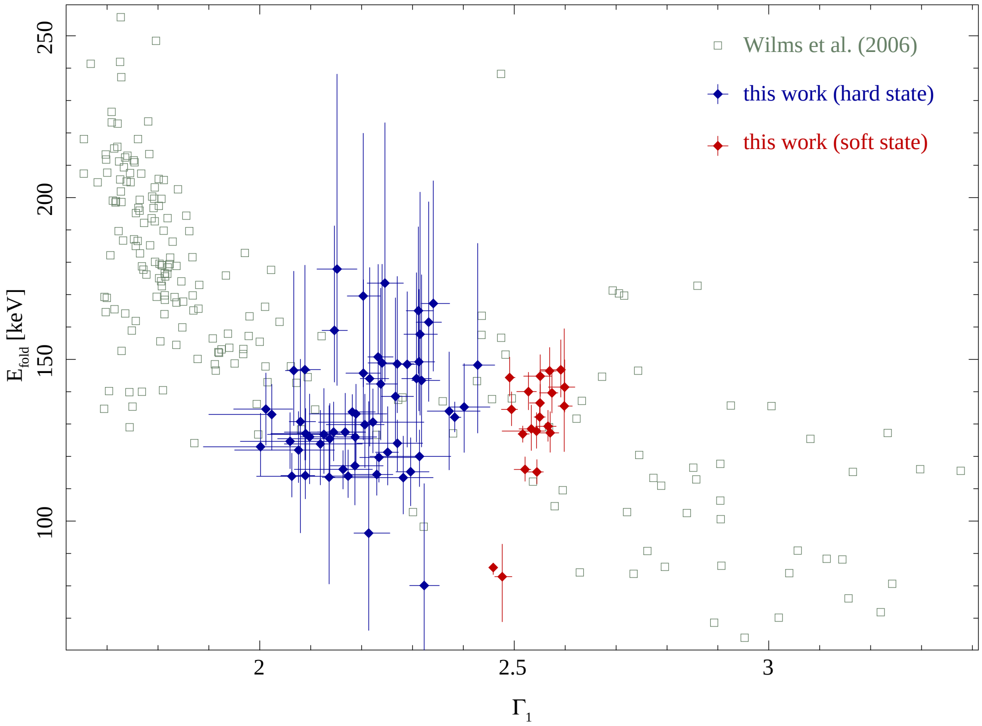

Figure 4.13: The relation between the folding energy and the photon index Γ_1. There is no clear correlation but the values of the parameters are consistent.

Chapter 5

Timing

As X-ray binaries show high variability on all timescales, it is crucial to perform timing analysis to figure out the physical processes causing this variability. Combining temporal with spectral analysis reveals the characteristic behavior of X-ray binaries and it is necessary to find explanations for it. In this section the timing methods are expounded and the results of their utilization are presented and interpreted.

5.1 Frequencies

An overview of characteristic frequencies for Cygnus X-1 and binaries in general is given in the following. Methods to detect them and common interpretations are discussed in addition.

5.1.1 Orbital Modulation

The most expected frequency in a light curve of a binary is probably the Keplerian frequency. It is caused by the orbital movement of its components. For Cygnus X-1 the orbital period P_{orb} is about 5.6 days. It was confirmed in all wavebands and by several authors. Its values agree well. For example a precise determination of the orbital period was performed by Brocksopp et al. (1999b). They used two different methods. The first one was spectroscopy. In the course of this characteristic lines were fitted to figure out their wavelengths. The radial velocity of the object causing these lines can be obtained from the Doppler shift of the lines. If there are enough observations, the period can be determined by considering the radial velocity and the point in time of each observation. Using many lines of helium (He II λ4686, He I λ4713, He I λ4921, He I λ5015, etc.) oxygen, magnesium and additional elements the final result was $P_{orb,sp} = 5.599829 \pm 0.000016$ days. The radial velocities are plotted in Fig. 5.1. The other method, which was photometry, yielded the value $P_{orb,phot} = 5.599836 \pm 0.000024$ days. The photometric period was given by a peak in the power spectrum, which was obtained by using discrete Fourier transformations of a data set consisting of several hundreds of observations. How power spectra are computed is described in section 5.2.1. Figure 5.2 shows the modulation of the radio and soft X-ray (2–12 keV) emission. The measured X-ray flux is minimal at superior conjunction of the system, which is defined as phase zero. It means that the black hole is behind its companion star, from our view. Due to the orbital inclination of Cygnus X-1, which is about 35°, there is no eclipse. But the geometry of the system (see Fig. 5.4) reveals that radiation originating close from the black hole has to cross a longer distance in the wind of the companion in the case of superior conjunction than in inferior conjunction. Thomson scattering and absorption by the wind is considered to cause the orbital modulation. As the density of the wind increases towards the star, the shape of the phase binned flux can be explained. The modulation of the radio emission is very interesting, especially by thinking about jets. As the radio emission is thought to be the synchrotron radiation of jets, it does not originate directly from the close surrounding of the black hole, like the accretion disk. The emission occurs further

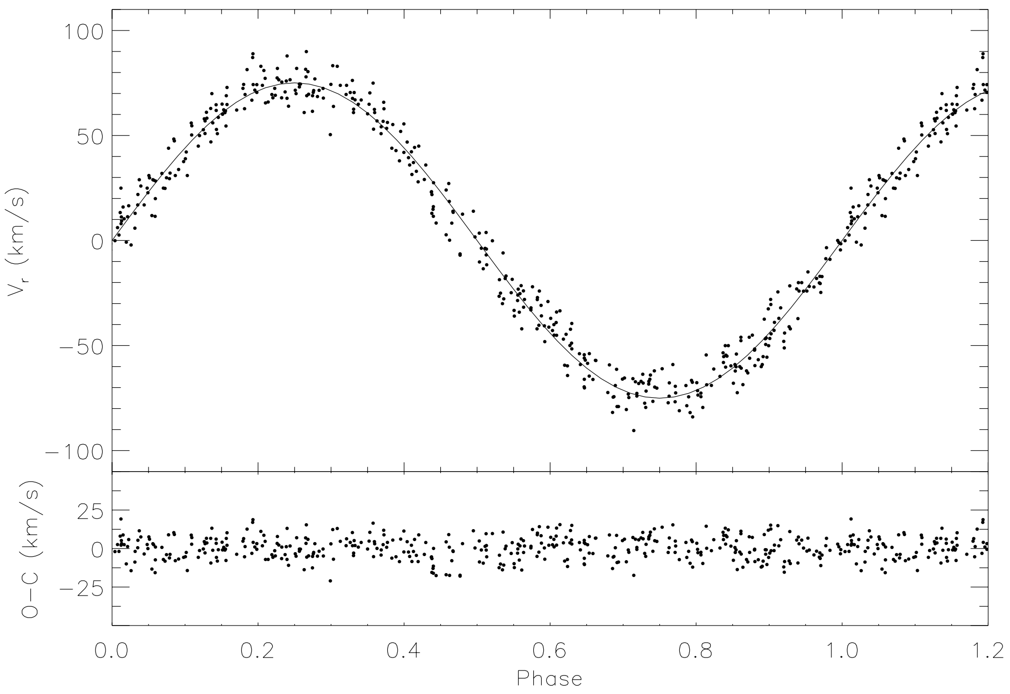

Figure 5.1: Radial velocities plotted as a function of the matching phase, which is measured in multiples of 2π. The solid line corresponds to the theoretical model. The bottom panel shows the differences. (picture from: Brocksopp et al. (1999b) Fig. 1)

afar of the black hole. Due to the expansion and cooling of the outer jet, the frequencies of the radio emission decrease with the distance. The radio data shows that the orbital modulation at 15 GHz is larger than that at 8.3 GHz, which was again larger than the measured modulation of the 2.25 GHz data (Fig. 5.2). Additionally there is a phase shift. Depending on its frequency the mean radio flux obtains a minimum at a different phase. The data sets measured at the three mentioned frequencies indicate a delay. Starting from a point in time with phase zero, the X-ray flux is minimal, the lower the frequency of the radio emission is, the longer it takes until its flux gets minimal. Pooley et al. (1999) found that the mean 2.25 GHz radiation is minimal at phase 0.3. Szostek & Zdziarski (2007) explain these phase lags by implying that the particles in the jet core have non-relativistic velocities. They also give a model for the orbital modulation of the radio emission due to free-free absorption in the wind of the companion star, by using strong restrictions on the spatial distribution of the emission.

5.1.2 Superorbital Period

The search for low frequencies revealed that there are lower frequencies than the Keplerian frequency contained in the emission of Cygnus X-1. Priedhorsky et al. (1983) found evidence for a period of 294 ± 4 days in data between 1969 and 1980, which were obtained with detectors aboard the satellites *Vela 5B* (3–12 keV) and *Ariel 5* (3–6 keV). It was the first low frequency which was found in the Cyg X-1 emission. As it was found only in these data, several test were performed to figure out if this periodicity was a real feature (Lachowicz et al., 2006, Appendix A). The results were confirmed and in addition a similar period of ~293 days was indicated in the corresponding 15 Ghz radio data. Another frequency with a period of about 150 days was detected in all data since ~1976. Benlloch et al. (2004) used data obtained with *RXTE*/ASM and PCA to investigate this period. The period and the phase of the corresponding modulation was stable over more than 65 cycles (Lachowicz et al., 2006). The most common interpretation of this superorbital modulation

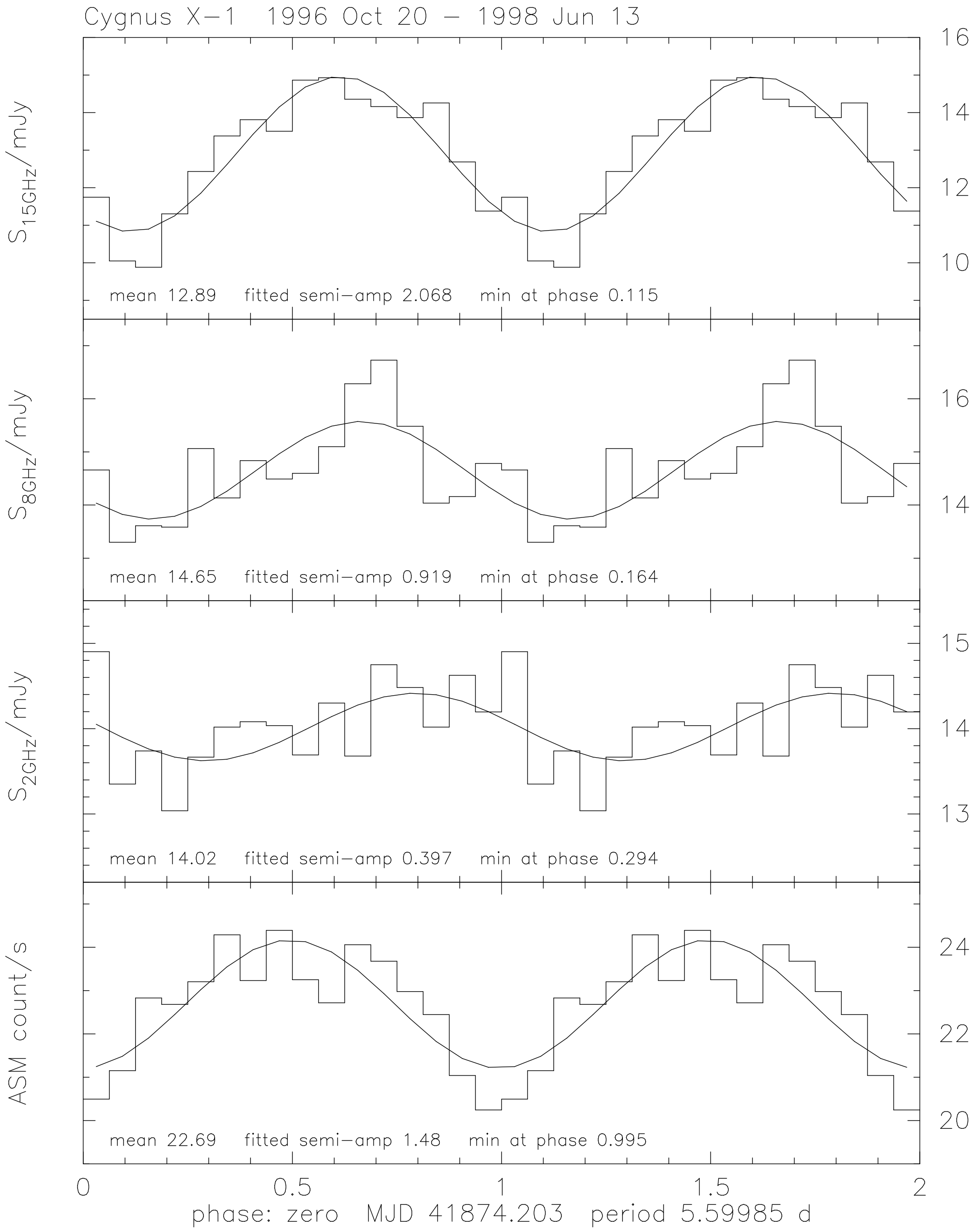

Figure 5.2: Picture from Pooley et al. (1999) (Fig. 2) which illustrates the orbital modulation in the radio and X-ray emission and the best sinusoidal fit to the data, which were ranged in 16 phase bins. Phase zero is defined as superior conjunction. RXTE-ASM detects photons between 2 and 12 keV. The radio flux was measured at 15, 8.3 and 2.25 GHz. This behavior indicates that the modulation decreases towards lower frequencies. In addition to the decrease of modulation there is an increasing phase shift.

is a precessing accretion disk, which is tilted with respect to the orbital plane by a certain angle δ. If the ratio between the two components of the binary, the orbital P_{orb} and the superorbital period P_{sup} are known, δ can be approximated via (Larwood, 1998, Eq. (3)):

$$\frac{P_{\mathrm{orb}}}{P_{\mathrm{sup}}} \simeq \frac{3}{7}\beta_{\mathrm{P}}^{3/2}\frac{\mu R^{3/2}}{\sqrt{1+\mu}}\cos\delta \tag{5.1}$$

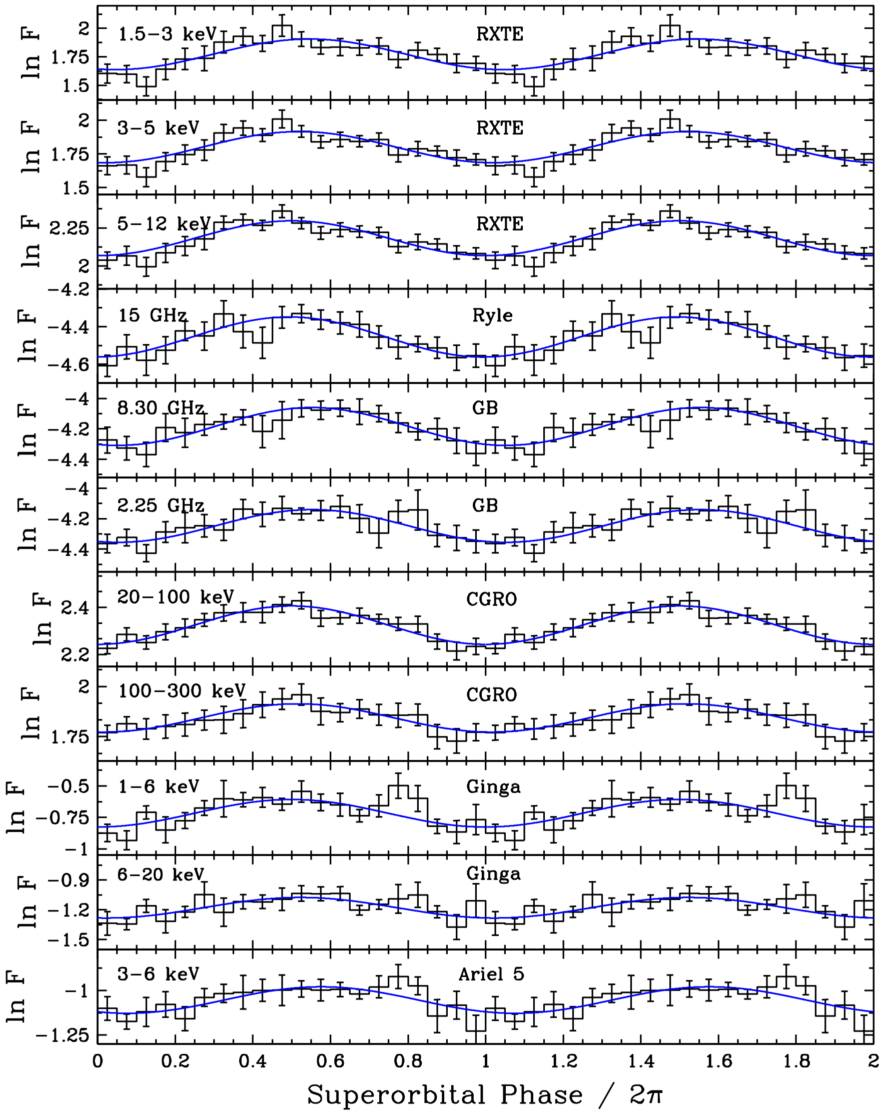

Figure 5.3: Phase diagram of the superorbital modulation (Lachowicz et al., 2006, Fig. 7), which illustrates the modulation in all measured wavebands. Here the fractional modulation depends on the energy of the data and varies between ∼13% (for 1.5–3 keV) and ∼26% (for 100–300 keV).

where μ is the ratio between the mass of the companion to that of the compact object and where R is the ratio between the Roche radius to the radius of the accretion disk. R can be written as a function of μ:

$$R(\mu) \simeq \frac{0.49}{0.6 + \mu^{3/2} \log\left(1 + \mu^{-1/3}\right)} \tag{5.2}$$

The factor β_P, which is called Paczyński's radius, describes the mean disk radius. It also depends on μ:

$$\beta_\mathrm{P}(\mu) \simeq \frac{1.4}{1 + [\log(1.8\mu)]^{0.24}} \tag{5.3}$$

A derivation of these functions and specifications of the used approximations is described in Larwood (1998) in more detail. Using Eq. 5.1 and the ∼150 day period Brocksopp et al. (1999a) found $\delta \simeq 37^\circ$ for Cyg X-1. The resulting geometry is illustrated in Fig. 5.4.

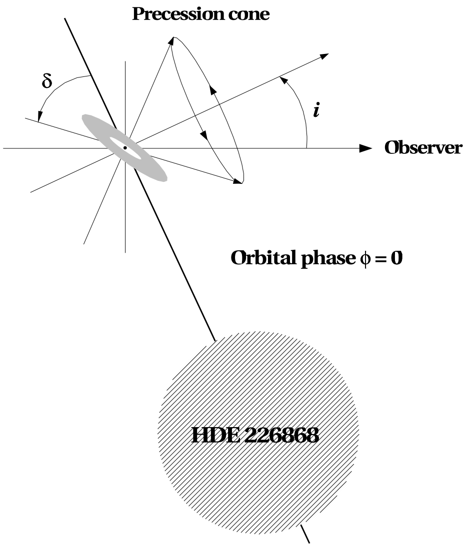

Figure 5.4: Schematic view of Cygnus X-1 by Lachowicz et al. (2006) (Fig. 9). Here, i is the inclination and δ the angle between disk and orbital plane. The precession of a tilted accretion disk is an explanation of the superorbital modulation.

There are no generally accepted interpretations for the 294 ± 4 day period, which was only detected in a certain space of time. The same holds for some other frequencies which were more or less slightly indicated in some data, like a modulation with a period of 210–230 days. These frequencies and the corresponding references are listed by Lachowicz et al. (2006, Sect. 5).

5.1.3 High Frequencies

In addition to the low frequencies one also expects higher frequencies. As the time scales for their periods are not days but seconds and milliseconds, the underlying processes have to occur in smaller spaces. Orbital movements of the compact object and its companion star do not come into question as a reason for these frequencies. High frequencies can be detected in the X-ray emission, which originates close from the compact object. For that reason it is obvious to consider processes in the vicinity of the compact object to be the cause for the small time scale modulations. Several frequencies can originate from the accretion disk. Possible modulations will be summarized in the following. A detailed description can be found in Nowak & Lehr (1998) and the references therein, where the characteristic frequencies in thin accretion disks are discussed. An equatorial plane of the compact object can be defined, which is perpendicular to its angular momentum. It can be assumed that the disk lies in this plane. The discussed frequencies depend on the mass of the compact object and its angular momentum. As the typical length scales, as for instance the Schwarzschild radius, increase linearly with the mass, the frequencies decrease. In the following formulas distances r are measured in multiples of the gravitational radius:

$$r_{\mathrm{g}} = GM/c^2 \tag{5.4}$$

Thus a radius is given in a dimensionless form by $R(r) = rc^2/(GM)$ where M is the mass of the compact object, G is the gravitational constant and where c is the speed of light. The angular momentum J of the black hole is characterized by the dimensionless value:

$$a = cJ/(GM^2) \tag{5.5}$$

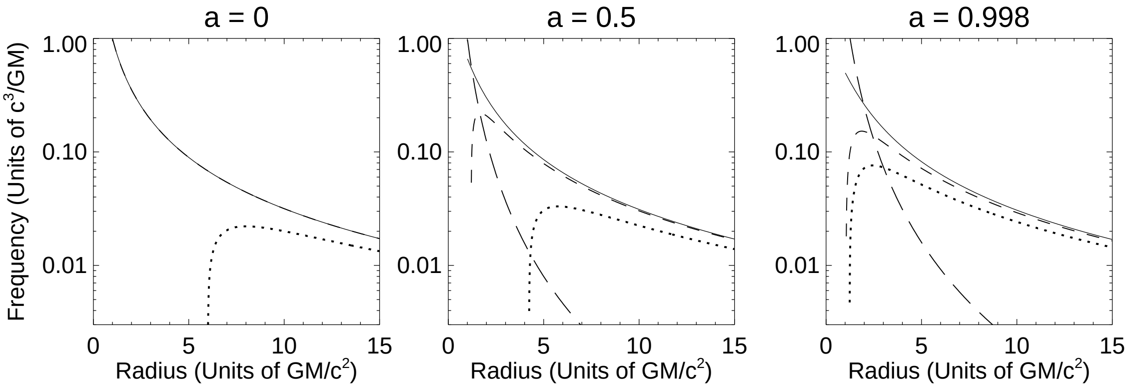

Figure 5.5: Overview of the most important frequencies in an accretion disk around a black hole by Nowak & Lehr (1998, Fig. 3). The radius is given in units of the gravitational radius, and the frequencies are normalized to $c^3/(2\pi GM)$, that is about 3.2×10^3 Hz for a black hole with a mass of $M = 10\,M_\odot$. The frequencies were calculated for different angular momentums of the black hole, characterized by the parameter a. The solid line is the Keplerian frequency f_k, the dotted line is the radial epicyclic frequency f_r and the dashed line is the vertical epicyclic frequency $f_\perp$. Values of the Lense-Thirring precession frequency f_LT are illustrated with a long dashed line.

For a non-rotating object, like a Schwarzschild black hole, a is equal to zero, whereas $0 < a < 0.998$ for a Kerr black hole ($J \neq 0$, Sect. 1.2).

The most plausible frequency in the disk is again the Keplerian frequency, that with which particles orbit around the compact object. A modulation in the light curve with a corresponding period can be interpreted as the orbital movement of an emitting area. The Keplerian frequency f_k is given by:

$$f_\mathrm{k}(R) = (R^{3/2} + a)^{-1} \cdot \frac{c^3}{2\pi GM} \tag{5.6}$$

For a Schwarzschild black hole ($a = 0$) with the mass $10\,M_\odot$, which is comparable to that of Cyg X-1, one obtains a frequency of about 220 Hz at $R = 6$. This is the radius of the innermost stable circular orbit for a non-rotating black hole. It decreases with increasing a. The dependence of $f_\mathrm{k}(R)$ on a is a relativistic effect, hence it cannot be explained be classical mechanics. $f_\mathrm{k}(R)$ is the frequency, which is observed at infinity, that is far away of the black hole. The following frequencies are also based on effects of General Relativity. Here, a particle on a circular orbit oscillates about this orbit, if it is radially perturbed. The frequency of this oscillation is called radial epicyclic frequency f_r and given by:

$$f_\mathrm{r}^2(R) = f_\mathrm{k}^2(R)\left(1 - \frac{6}{R} + \frac{8a}{R^{3/2}} - \frac{3a^2}{R^2}\right) \tag{5.7}$$

A Schwarzschild black hole with the mass $M = 10\,M_\odot$ yields a maximal radial epicyclic frequency of about 71 Hz for $R = 8$. At the innermost stable circular orbit f_r is equal to zero. The maximum increases with a. If a is close to 1, this maximum is approximately equal to the maximal Keplerian frequency. In classical mechanics $f_\mathrm{k}(R)$ and $f_\mathrm{r}(R)$ are identical for Keplerian orbits in an r^{-1} potential, where a radial perturbation changes a circular orbit in an elliptical one. A vertical epicyclic frequency $f_\perp(R)$ can be defined analogously to the radial one. It is the frequency at which a particle, that was on a circular orbit, oscillates about its original orbit, if it was vertically perturbed. The resulting frequency is given by:

$$f_\perp^2(R) = f_\mathrm{k}^2(R)\left(1 - \frac{4a}{R^{3/2}} + \frac{3a^2}{R^2}\right) \tag{5.8}$$

Another important frequency is the Lence-Thirring precession frequency f_LT. It describes the frequency at which matter, which is tilted against the equatorial plane, precesses around a rotating black hole due to frame dragging effects. The precession occurs only if the black hole is rotating. The Lense-Thirring precession frequency has a strong radial dependence and is given by:

$$f_{\mathrm{LT}}(R) = \frac{2a}{R^3} \cdot \frac{c^3}{2\pi GM} \tag{5.9}$$

An overview of the discussed frequencies is shown in Fig. 5.5. They are illustrated as a function of the radius, for different values of the angular momentum. The values of the two epicyclic frequencies are similar to that of the Keplerian frequency. An increasing difference occurs towards the innermost stable orbit. A high Lense-Thirring precession frequency is expected at small radii in the case of large angular momentums of the black hole.

5.2 Power Spectral Density

5.2.1 Computation

To find the frequencies in a time-dependent curve it is common to use Fourier analysis. As light curves are binned quantities a discrete Fourier transformation has to be applied. The calculation of the power spectral density (PSD) used here follows Nowak et al. (1999a). The starting point is a light curve, which is binned at $2^{-9}\,\mathrm{s} \approx 2\,\mathrm{ms}$ time resolution. There are of course different time resolutions available, depending on the data modes (section 3.2), but it has turned out that $2^{-9}\,\mathrm{s}$ is the most meaningful resolution for the Fourier analysis. The highest observable frequency depends on the binning of the light curve, thus a high time resolution is necessary. No frequencies $\gtrsim 200\,\mathrm{Hz}$ can be observed (Nowak et al., 1999a) however, they are drowned out by noise.For that reason it is not necessary to use data modes with higher time resolutions, such as 2^{-12} or $2^{-13}\,\mathrm{s}$. To calculate the power spectral density, the light curve is divided into segments. Each segment has the same duration $T = N\Delta t$, where N is the number of the bins per segment and where Δt is the length of one time bin, it has to be identical for each bin. Only segments without any time gaps are taken into account. The complex discrete Fourier transformation of a segment s is given by:

$$S_j = \sum_{k=0}^{N-1} s_k \exp\left(2\pi i \frac{jk}{N}\right) \tag{5.10}$$

where s_k is the number of counts in the kth bin of the segment. S_j depends on the Fourier frequency:

$$f_j = \frac{j}{N\Delta t} \tag{5.11}$$

The frequencies which can be obtained are given by the possible values of j, which are $j \in [-N/2, N/2]$. It is now easy to see how the maximal observable frequency is tied to the time resolution: $f_{\mathrm{max}} = 1/(2\Delta t)$. f_{max} is the Nyquist frequency. The minimal frequency depends on the duration of the segment: $f_{\mathrm{min}} = 1/(N\Delta t) = 1/T$.

The power spectral density is a real value, which is given by the square of the absolute value of the complex discrete Fourier transformations:

$$P(f_j) \propto \langle |S_j|^2 \rangle = \langle S_j S_j^* \rangle \tag{5.12}$$

To improve the signal to noise ratio, several segments are considered and the squares of $|S_j|$ are averaged (van der Klis, 1989).

The normalization of the PSD determines its relation to the variance of a light curve. With the normalization of Miyamoto et al. (1991), the PSD reads as follows:

$$P(f_j) = \frac{2}{\langle L_c \rangle^2 T} \langle |S_j|^2 \rangle \tag{5.13}$$

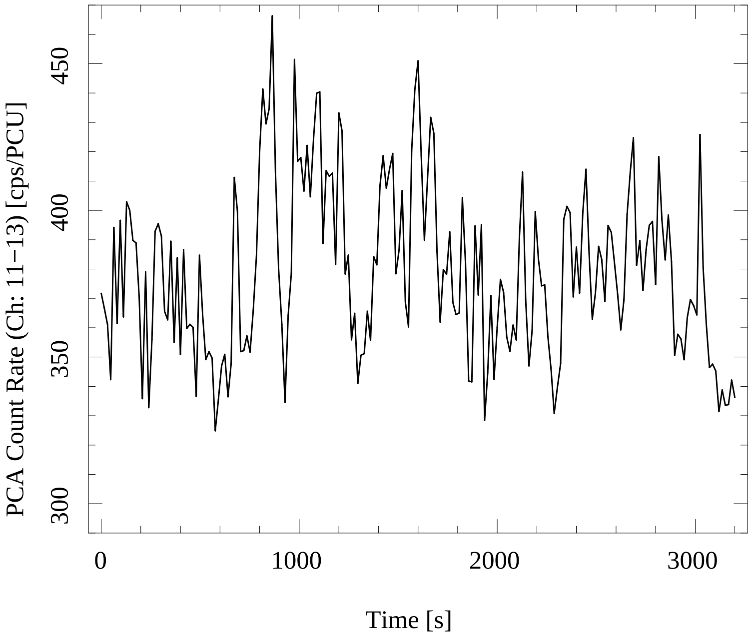

Figure 5.6: A typical light curve of an observation with an exposure of about 3 ks. The shown light curve has a time resolution of 16 seconds. To figure out the contained frequencies the power spectral density of the light curve is computed. For the computation a higher resolution of the light curve is used, namely 2 ms.

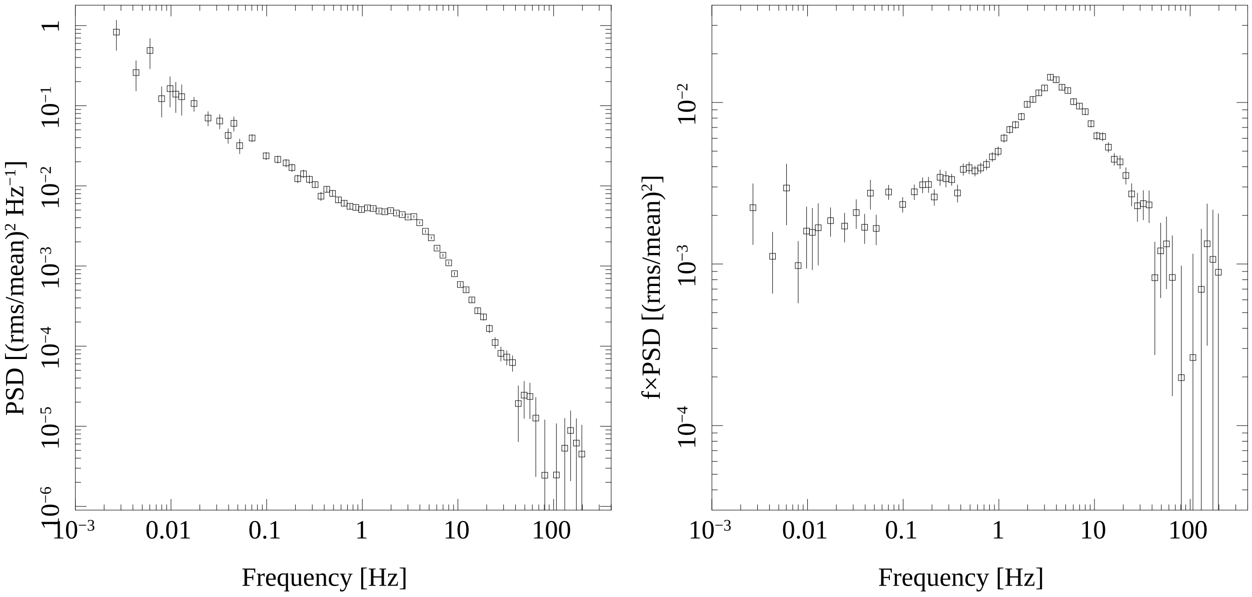

Figure 5.7: The PSD which was computed from the light curve shown in Fig. 5.6. Instead of a PSD the most Figures in this work show f×PSD. Here the characteristic humps can be seen more clearly, as well as the contribution of the Fourier frequencies to the total variability considering the logarithmically scaled frequencies axis.

Where $\langle L_c \rangle$ is the mean count rate of the light curve (in counts per second). Using this normalization, the integral of the PSD over positive frequencies yields the fractional variance of the light curve $L_c(t)$ which is the square of the root mean square (rms) divided by the mean count rate:

$$\frac{rms^2}{\langle L_c \rangle^2} = \frac{\langle L_c^2 \rangle - \langle L_c \rangle^2}{\langle L_c \rangle^2} \tag{5.14}$$

Note that only the integration over positive frequencies is necessary due to the factor 2 in the numerator of the PSD normalization, which takes into account that $|S_j|^2$ is equal to $|S_{-j}|^2$. Integrating only over a certain frequency range yields the fractional variance of the light curve caused by the variability given by these frequencies. $P(f)$ measures the contribution of the frequency f to the variability of the light curve and is therefore a very useful method to find periodic signals in light curves. Such signals can be seen in a PSD as a peak at the corresponding frequency. The analyzed PSDs of Cygnus X-1 show a variability over broad frequency ranges. PSDs are also proper to figure out the characteristic variability distributions as a function of the frequencies. Fig. 5.7 illustrates such a PSD. An important point is that effects like noise, background and detector dead time or statistical uncertainties can be considered in the calculation of the PSDs. To decrease the errors of a PSD of an observation, it is averaged over the PSD which were obtained for the different segments and it is logarithmically re-binned. A very detailed description of the computation of PSDs and the minimization of their uncertainties is given by Pottschmidt (2002) in Ch. 3.2.

5.2.2 Fit Functions

To model the PSDs the Interactive Spectral Interpretation System (ISIS) (Houck & Denicola, 2000) was used, which is designed to fit spectra. A spectrum consisting of energy bins and a number of counts in these bins, is a bin integrated value, whereas a PSD is a bin density value. By simply multiplying the value of the PSD in a bin with the width of the bin, the PSD can be treated like a spectrum and advantage of the fit algorithms being implemented in ISIS can be taken. The power spectra were modeled with a powerlaw with an exponential cutoff added to the sum of Lorentzian profiles. A Lorentzian is the Fourier transformation of a damped harmonic oscillation and given by:

$$L_i(f) = \frac{\nu_i R_i^2}{\pi Q_i \left(\nu_i^2 - \frac{4\nu_i Q_i}{\sqrt{1+4Q_i^2}} f + f^2 \right)} \tag{5.15}$$

where R_i is the normalization constant, $Q_i = f_i / \Delta f_{i,\mathrm{FWHM}}$ the quality factor and the peak frequency ν_i is the frequency where $f \times L_i(f)$ reaches its maximum. It is related to the resonance frequency f_i via:

$$\nu_i = f_i \sqrt{1 + \frac{1}{4Q_i^2}} \tag{5.16}$$

Substituting this expression into Eq. (5.15) yields the definition used by Pottschmidt et al. (2003):

$$L_i(f) = \pi^{-1} \frac{2R_i^2 Q_i f_i}{f_i^2 + 4Q_i^2 (f - f_i)^2} \tag{5.17}$$

In Miyamoto normalization, the rms amplitude of a Lorentzian L_i is given by:

$$\mathrm{rms}_i^2 = \int_0^\infty L_i(f) df = R_i^2 \left(\frac{1}{2} + \frac{\arctan(2Q_i)}{\pi} \right) \tag{5.18}$$

A Lorentzian profile as given by Eq. (5.13) had to be implemented in ISIS. As bin-integrated data and model values are considered within ISIS, one has to provide the integral of the fit function over

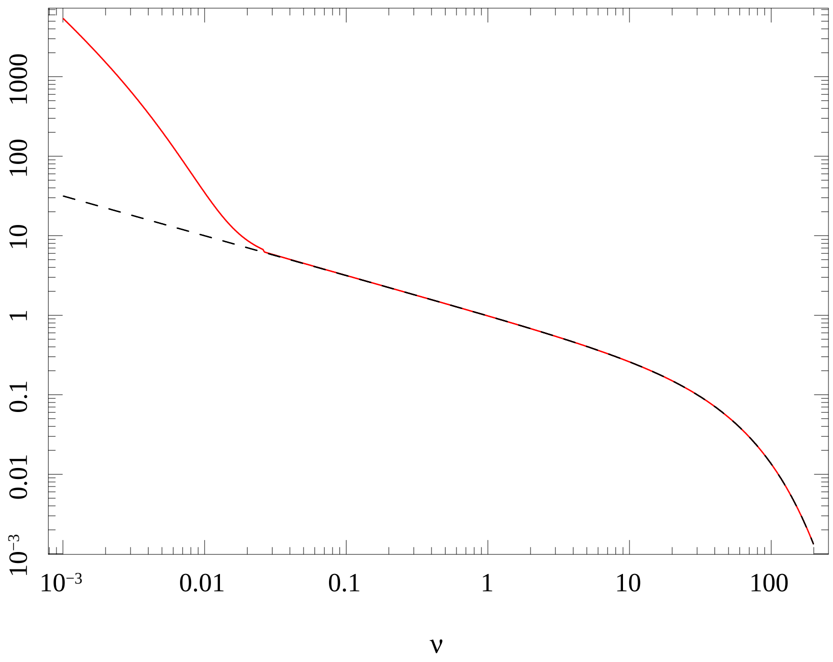

Figure 5.8: The correct power law with exponential cutoff: $P_{cut}(\nu) = \nu^{-1/2}\exp(-\nu/50)$ (dashed) compared to the one with bug (solid, red).

a bin $[lo, hi]$. For a Lorentzian profile it can be calculated analytically:

$$\int_{\mathrm{lo}}^{\mathrm{hi}} L_i(f)df = \frac{R_i^2}{\pi}\left[\arctan\left(\frac{2Q_i(f_i - lo)}{f_i}\right) + \arctan\left(\frac{2Q_i(f_i - hi)}{f_i}\right)\right] \tag{5.19}$$

Where lo and hi are the lower und upper limits of the bin. Additionally to the Lorentzian profiles a power law with an exponential cutoff $P_{\mathrm{cut}}(f)$ was required to model the PSDs properly:

$$P_{\mathrm{cut}}(f) = kf^{\alpha}\exp\left(-f/f_{cut}\right) \tag{5.20}$$

This function has three parameters, namely a norm k, a cutoff frequency f_{cut} and the power law index α. Using the fit function *cutoffpl* provided by XSPEC, which was implemented in ISIS, revealed a strange feature at low frequencies. At a certain frequency the *cutoffpl* started deviating from the correct values (see Fig. 5.8). It could be figured out this behavior was caused by problems in the numerical calculation of the integral of P_{cut}. There is no analytical solution to this integral for $\alpha \in \mathbb{R}\backslash\mathbb{N}$. It can, however, be expressed in terms of incomplete gamma functions:

$$\int_{lo}^{hi} P_{cut}(f)df = \int_{lo}^{hi} kf^{\alpha}e^{-f/f_{\mathrm{cut}}}df = kf_{cut}^{\alpha}\left[\gamma\left(\alpha-1, \frac{hi}{f_{cut}}\right) - \gamma\left(\alpha-1, \frac{lo}{f_{cut}}\right)\right] \tag{5.21}$$

$$= kf_{cut}^{\alpha}\left[\Gamma\left(\alpha-1, \frac{lo}{f_{cut}}\right) - \Gamma\left(\alpha-1, \frac{hi}{f_{cut}}\right)\right] \tag{5.22}$$

where $\gamma(a,x)$ is the lower and $\Gamma(a,x) = \Gamma(a) - \gamma(a,x)$ the upper incomplete Gamma function. $\Gamma(a)$ is of course the Gamma function.

$$\gamma(a,x) = \int\limits_0^x e^{-t} t^{a-1} dt = e^{-x} x^a \sum_{n=0}^{\infty} \frac{\Gamma(a)}{\Gamma(a+1+n)} x^n \tag{5.23}$$

$$\Gamma(a,x) = \int\limits_x^{\infty} e^{-t} t^{a-1} dt = e^{-x} x^a \left(\frac{1}{x + \frac{1-a}{1+\frac{1}{x+\frac{2-a}{1+\frac{2}{x+\cdots}}}}} \right) = e^{-x} x^a \left(\frac{1}{x+} \frac{1-a}{1+} \frac{1}{x+} \frac{2-a}{1+} \frac{2}{x+} \cdots \right) \tag{5.24}$$

The continued fraction development in Eq. (5.24) converges fast for $x \gtrsim a+1$, while Eq. (5.23) does so for $x \lesssim a+1$. Further information can be found in "Numerical Recipes in C" (Chapter 6.2, Press et al., 1992). In XSPEC only the expansion of Eq. (5.24) was used for the numerical calculations in the fit function *cutoffpl*, which led to the discussed problem at low frequencies. This issue could be fixed by defining the fit function with help of the GNU Scientific Library (GSL), which evaluates an incomplete gamma function by the expansion of Eqs. (5.23) or (5.24) which converges better, depending on the value of α and f/f_{cut}.

5.2.3 Fit Model

The components of the model which was used to fit the power spectra, are explained above, namely Lorentzian profiles and a power law with exponential cutoff. Up to now the number of Lorentzian profiles has not been fixed. But this number is of course important for the fits and the interpretation. The first idea was to use the sum of four Lorentzian profiles in addition to the power law. The reason was that there was already a long term observation of Cygnus X-1 by Pottschmidt et al. (2003). They used four Lorentzians to model the power spectra of observations between 1998 and 2001. In certain cases close to the soft state an additional power law was required. To model quasi periodic oscillations (QPOs) one or two additional narrow Lorentzians were applied. QPOs are narrow peaks in the power spectra. Different types of QPOs are discussed in detail in Casella et al. (2005). Using a similar model for the power spectra which were obtained from the observations evaluated in this work allows to compare the resulting parameters and correlations with the ones of Pottschmidt et al. (2003). For that reason the first fit model used was the sum of four Lorentzian profiles and a power law with exponential cutoff. As discussed in Sect. 3.3 light curves in different energy bands, namely the low (4.5–5.8 keV) and high (9.5–15 keV) energy band were available. Thus two power spectra were computed for each observation. They will be designated PSD_{low} and PSD_{high} in the following. As there were 78 observations, which had sufficient exposure time to calculate a PSD, 156 power spectra had to be fitted in total. At first each PSD was fitted with two different fit functions, namely four Lorentzians with and without the power law. Comparing the results revealed that the χ^2 was much smaller in the most cases if a power law was added, especially if the PSD had large values at low frequencies. For that reason only models including a power law were used from then on. A problem with the Lorentzians was their sequence. For the fitting of the power spectra a given set of model parameters is necessary to begin with. During the fitting process it can happen that two Lorentzians change their position. This would lead to a mismatch of the resulting fit parameters and the evaluation of these parameters would not make sense. For example if one wants to analyze the relation between the peak frequencies of the second Lorentzian ν_2 and the date of the observations, it is crucial that there are only peak frequencies included which correspond to the second Lorentzian and not to the third for example, as it would be the case if they had changed position. To prevent such permutations a constraint was implemented in the fitting process. The sequence of the Lorentzians was fixed by the condition that the peak frequency of L_3 has to be larger than the one of L_2 and so on. With this model good fits ($\chi^2_{\mathrm{red}} < 2$) for all PSDs were found. If necessary an additional narrow Lorentzian was used to

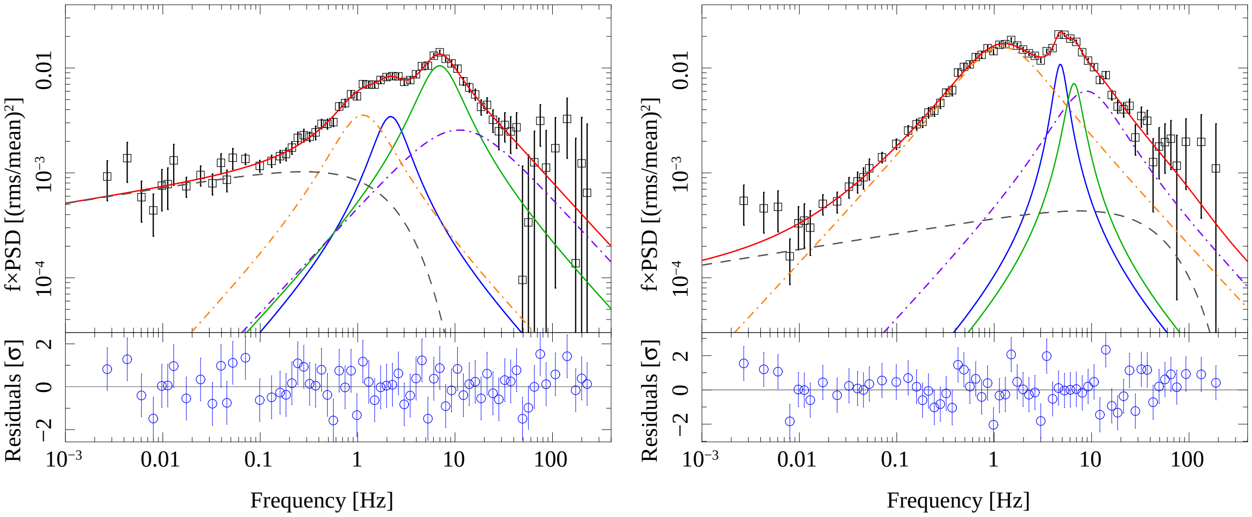

Figure 5.9: Four Lorentzians and a power law with exponential cutoff model the data quite well, due to the large number of free parameters. There are 3 parameters for each component, but the allocation of the Lorentzians is difficult. Only two Lorentzians could be clearly identified with characteristics of the power spectra, namely the two humps. For that reason the data were fitted with only two Lorentzians and a power law, and the other Lorentzians were excluded from the model.

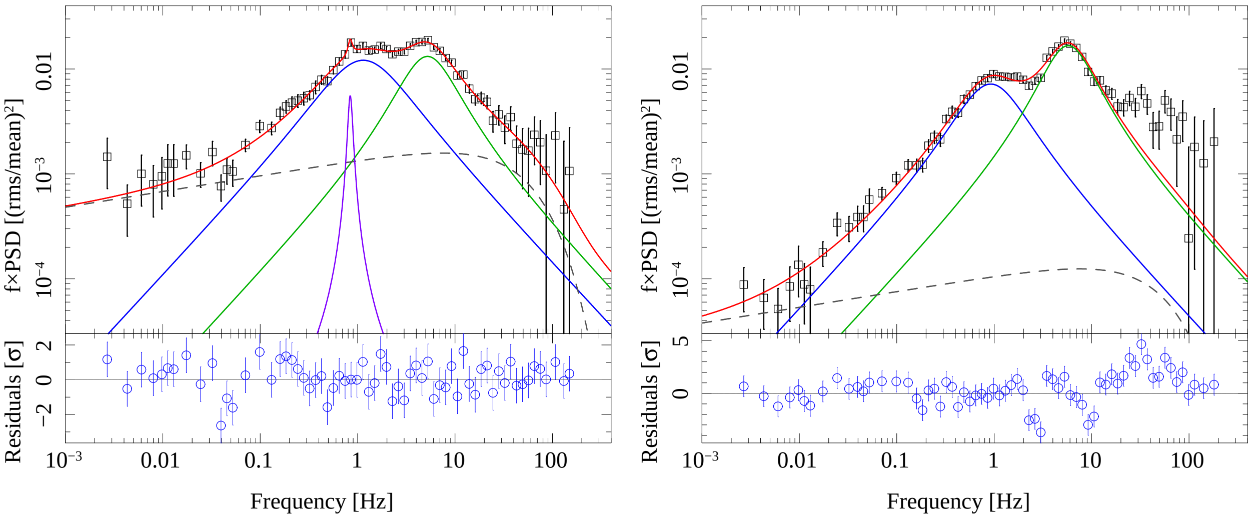

Figure 5.10: Effects that were not included in the fit model. The left plot shows a fit with a QPO. A narrow Lorentzian models the quasi periodic oscillation. On the right the power spectrum is shown, whose fit has the strongest indication of a third Lorentzian in this work. As both phenomena occur only in certain cases and do not change the analyzed parameters significantly, they were ignored in this work.

improve the χ^2 further by modelling a QPO. The evaluation of all fitted power spectra revealed that the fits were quite good in the sense that the difference between data and model was very small. But an interpretation of the best fit parameters was problematic, as they varied from one PSD to another. Lorentzians were shifted, even with a fixed frequency-dependent order. Figure 5.9 is a good example for this problem, which uncorrelates the parameters of a single Lorentzian and the power spectra. To get such a relation, each Lorentzian has to be identified with a certain characteristic of the power spectra, which is present in the majority of them. As most power spectra show two humps, it is obvious to identify each hump with a Lorentzian profile. Starting from the fits with fixed sequence, the Lorentzians were moved such that one Lorentzian was always located at the first hump and another one at the hump at higher frequencies. The analysis of the new results indicated correlations between the parameters of these two Lorentzians and for example spectral parameters. But there was still a problem with the two remaining Lorentzians. Without a special assignment they still moved around during fitting. In different PSDs they sometimes had completely different parameters. They could have low or very high peak frequencies, or were even found in one of the humps which was already modeled by another Lorentzian, if its shape could be modeled better with two Lorentzians. So their parameters were improper for analysis. If they were not taken into account, especially the last case was a problem, because here they strongly influenced the evaluated parameters, such as the rms, of the two important Lorentzians. For that reason the best solution was to exclude these Lorentzians completely from the fit model. All power spectra were fitted with the sum of two Lorentzians and the power law with exponential cutoff from then on. The χ^2 of the fits slightly changed to the worse only in certain cases. The reasons were that a few fits indicated a third Lorentzian with a peak frequency of about 10–100 Hz and a small number of power spectra showed evidence for quasi periodic oscillations. Examples of power spectra showing these features are given in Fig. 5.10. The application of additional components, to model these effects, improved the fits only slightly, as already mentioned, and there was no significant change of the other fit parameters, which were evaluated. Restricting oneself on two Lorentzians is a big difference to the work of Pottschmidt et al. (2003). In contrast to their long term observation, two broad Lorentzians in addition to a power law with an exponential cutoff describe the PSDs analyzed in this accurately enough. Comparing the underlying data gives a reason for that. The long term observation included a large amount of hard states, which can be characterized by the photon index Γ_1. Wilms et al. (2006) defined a hard state by $\Gamma_1 < 2.1$. It has turned out that power spectra of hard state observations have more than two humps, thus a larger number of Lorentzians is necessary for fitting. The data analyzed here, include no typical hard state, as Γ_1 is always larger than 2.0, furthermore the individual observations were shorter.

5.2.4 Fitting Results

As described above, all power spectra (both energy bands) were modeled using the sum of only two Lorentzian profiles in addition to a power law with exponential cutoff as a fit function. The available power spectra were computed from the single orbit observations, whose X-ray spectra were already analyzed in section 4 with the intention to find correlations between the spectral and the timing parameters.

Several interesting phenomena can already be seen by comparing the PSDs by eye. They were confirmed by the analysis of the fit parameters, which also revealed additional correlations among themselves. Each PSD is characterized by nine fit parameters. Three for the power law, namely its norm, the slope and the cutoff frequency. Each Lorentzian profile has another three, which are a norm, a peak frequency and a quality factor. These parameters are discussed in detail in section 5.2.2. The shapes of the power spectra of some observations differ significantly. It has turned out that the shape depends on the state of the source. A sequence of PSDs obtained for different states can be seen in Fig. 5.11. In the hard state typical power spectra of Cygnus X-1 show a double humped shape. Each hump can be modeled by a Lorentzian profile (as mentioned above, only two characteristic humps were observed in this work). The contribution of the low frequencies to the variability of the corresponding light curve is very small. $f \times \mathrm{PSD}(f)$ decreases strongly to low frequencies. If the X-ray spectrum of the corresponding observation becomes softer this shape changes. In the intermediate state, there is already a much larger contribution of low frequencies. In order to fit a power spectral density with increased values at low frequencies, the power law is used. Additionally the humps of the PSD shift to higher frequencies. This trend continues with increasing softness of the X-ray spectra. In a real soft state the power law with exponential cutoff is the most important component of the fit model. Another notable phenomenon is that the norm of the second Lorentzian L_2, which is located at higher frequencies, decreases. In several PSDs L_2

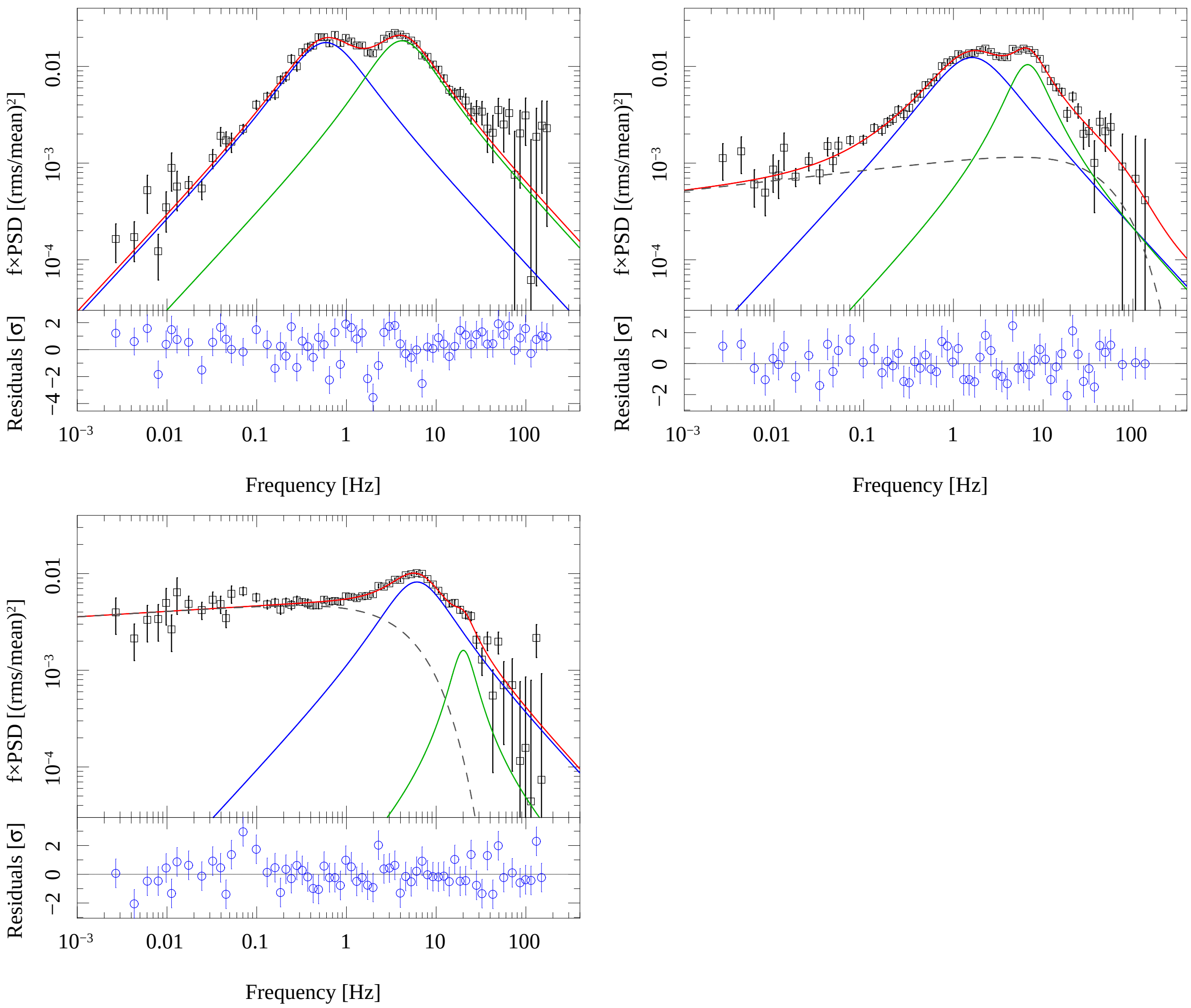

Figure 5.11: Examples of characteristic power spectra. The PSD plotted top left was extracted from an observation with one of the hardest spectra. The power spectral density vanishes for low frequencies and it shows a double humped shape. Two Lorentzians model the PSD quite well and no power law is necessary. The PSD slightly indicates a third Lorentzian profile with a peak frequency between about 40–80 Hz. To fit a PSD obtained from an intermediate state observation the power law becomes important (top right). Its contribution increases even further in the soft state (bottom left), where the low frequencies play an important role. Additionally the hump at higher frequencies decreases. In some PSDs it cannot be seen anymore at all. This sequence of power spectra also indicates that humps and thereby the peak frequencies of the Lorentzian profiles shift to higher frequencies as the X-ray spectrum gets softer.

cannot be seen. The dependence of the peak frequencies ν_i on the softness of the corresponding X-ray spectrum, can be illustrated by plotting ν_i as a function of the photon index Γ. For the spectral analysis a broken power law was used, hence there are two photon indices Γ_1 and Γ_2, but they are related via a linear function (Wilms et al., 2004). For that reason it is sufficient to restrict on Γ_1. A clear correlation between Γ_1 and the peak frequencies ν_1 and ν_2 of the two Lorentzians exists (Fig. 5.13). To quantify the correlations a correlation coefficient is introduced. The degree of linear correlation between two data sets x and y of equal length can be measured by the correlation

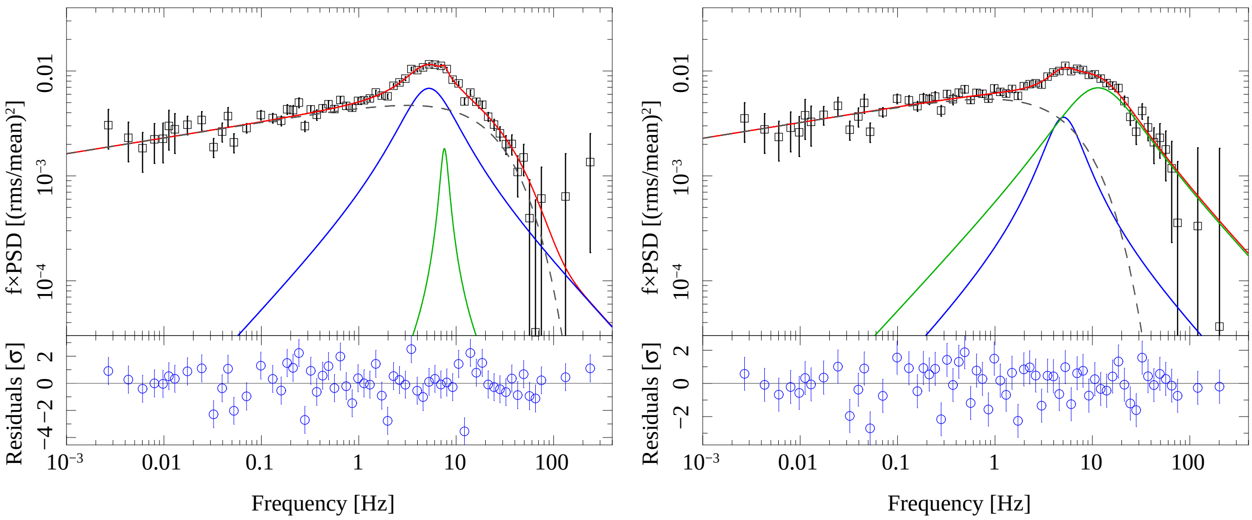

Figure 5.12: Exemplary power spectra that illustrate fitting problems for soft state observations. In the left panel the best fit to a low energy power spectrum is shown and on the right there is the corresponding fit in the high energy band. The parameters of a Lorentzian profile cannot be compared between the energy bands.

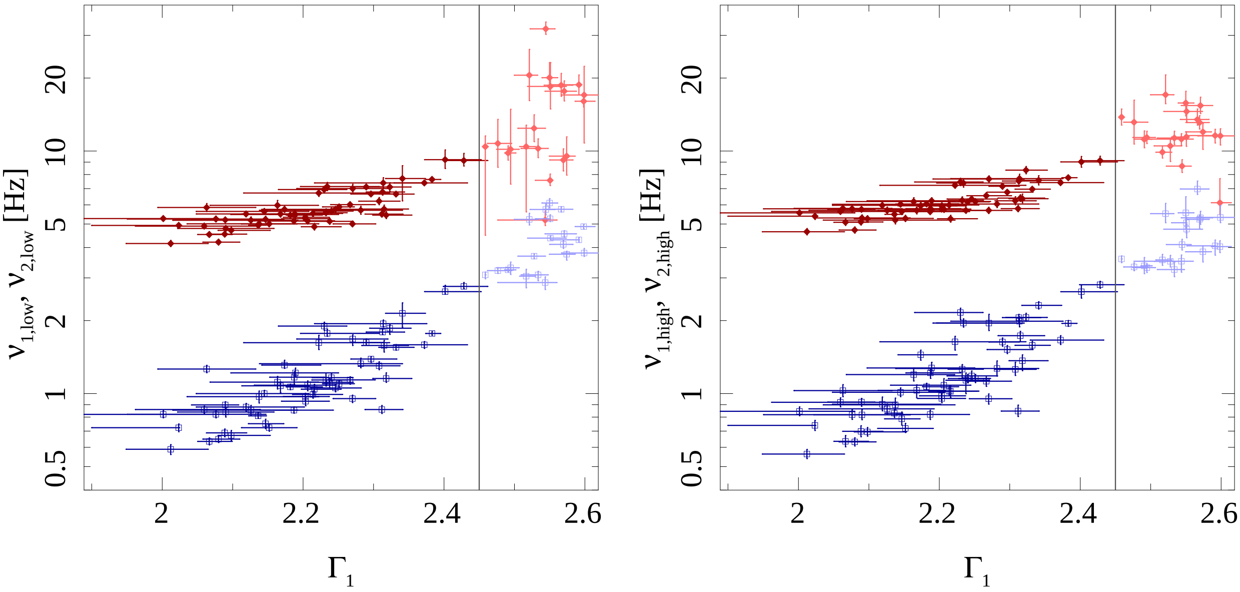

Figure 5.13: Between the photon index and the peak frequencies of the Lorentzian profiles there is a clear correlation. The left panel shows this relation in the low energy channel. The peak frequencies obtained for the PSD in the high energy channel (right panel) are identical to the ones in the low energy channel. The vertical line indicates the transition. After the transition the uncertainties of the peak frequencies are significantly larger than before due to the reasons illustrated in Fig. 5.12

coefficient (Bevington & Robinson, 1992, Eq. 11.17):

$$\rho(x,y) = \frac{\langle xy\rangle - \langle x\rangle\langle y\rangle}{\sqrt{\langle x^2\rangle - \langle x\rangle^2}\sqrt{\langle y^2\rangle - \langle y\rangle^2}} \in [-1,1] \tag{5.25}$$

where $\rho(x,y)$ is only defined if the standard deviations of x and y are nonzero. For a perfect linear correlation between x and y, which is increasing, $\rho(x,y)$ is equal to 1. If it is a decreasing relation, the correlation coefficient is equal to -1. $\rho(x,y)$ goes to zero, if x and y are independent data sets. Using this definition it is not possible to figure out non-linear relations between the data sets directly. Moreover errors of the data are not considered. To fit the data with a linear function, by taking the error bars into account, the method of Fasano & Vio (1988) is used.

The analysis revealed the following results:

- The peak frequency of the first Lorentzian in the high energy PSD is almost identical to the one in the low energy PSD. There is a quite good correlation between them.

  $$\rho(\nu_{1,\mathrm{high}}, \nu_{1,\mathrm{low}}) \approx 0.97 \tag{5.26}$$

  The linear relation between the data differs only slightly from the identity:

  $$\nu_{1,\mathrm{high}} = (-0.04 \pm 0.01)\,\mathrm{Hz} + (1.07 \pm 0.01)\nu_{1,\mathrm{low}} \tag{5.27}$$

  The fits yielded values for ν_1 between about 0.5 and 6 Hz.

- To get a similar relation for the second Lorentzian, the peak frequencies obtained for PSDs of soft states were neglected. As mentioned above, the second Lorentzian vanishes in the soft state. For that reason its peak frequency is no meaningful quantity during that state. This problem is discussed later on the basis of the rms correlations (see Sect. 5.2.5). Examples of fits, that illustrate this problem, are shown in Fig. 5.12. The correlation coefficient between the peak frequency of L_2 in the different energy ranges is:

  $$\rho(\nu_{2,\mathrm{high}}, \nu_{2,\mathrm{low}}) \approx 0.97 \tag{5.28}$$

  In contrast to the first Lorentzian, the peak frequencies seem to be not exactly identical for the two energy bands:

  $$\nu_{2,\mathrm{high}} = (0.96 \pm 0.04)\,\mathrm{Hz} + (0.91 \pm 0.01)\nu_{2,\mathrm{low}} \tag{5.29}$$

The two peak frequencies $\nu_{1,\mathrm{low}}$ and $\nu_{2,\mathrm{low}}$ do not increase independently with the softness of the spectrum, but are clearly correlated (Fig. 5.14). The corresponding correlation coefficient and a fit for the linear relation is given in Table (5.1). In addition it was tested if the peak frequencies are related via a power law, by searching a linear correlation between $\log(\nu_1/\mathrm{Hz})$ and $\log(\nu_2/\mathrm{Hz})$. The resulting correlation coefficients are comparable. In both cases the correlation improves if the soft state data are ignored. In the same way the relation between the peak frequencies and the photon index Γ_1 can be quantified. The results are listed in table 5.2 and the underlying data are shown in Fig. 5.13. In contrast to the relation between the ν_1 and ν_2, the correlation between ν_i/Hz or $\log(\nu_i/\mathrm{Hz})$ and Γ_1 improves if the soft state data are taken into account. This must not be overinterpreted, because the correlation coefficients are calculated without considering the errorbars. Also the available data do not allow to differentiate in which way they are correlated. Linear functions seem to fit the data as good as exponential relations or power laws, respectively. Probably more data have to be taken into account to figure out a better model. An important point is that the parameters obtained for the analyzed observations cover only a certain range of values. For example Γ_1 varies in the range $[2.0, 2.6]$ whereas values of Γ_1 between 1.6 and 3.4 were found in the long term observation of Cygnus X-1 (Wilms et al., 2006). Using maximal parameter ranges could clarify the relation between them. The relation between peak frequencies and can be visualized by plotting the product of power spectral density and corresponding frequency as a function of the photon index (Fig. 5.15). To get a two dimensional picture a color code is used. Large values of $\mathrm{PSD}(f) \times f$ are illustrated dark and smaller values are brighter. This image shows the humps of the PSDs as dark bands, which shift to higher frequencies with increasing Γ_1. In addition it can be seen clearly how the second hump disappears if the photon index exceeds a certain value. This value lies above 2.4, which is about the value where there the state transition took place. It looks like the two humps are equally dark in the low energy band, whereas in the high energy band the higher frequency hump is more distinctive as the other one. The differences between the two energy bands will be discussed in the following.

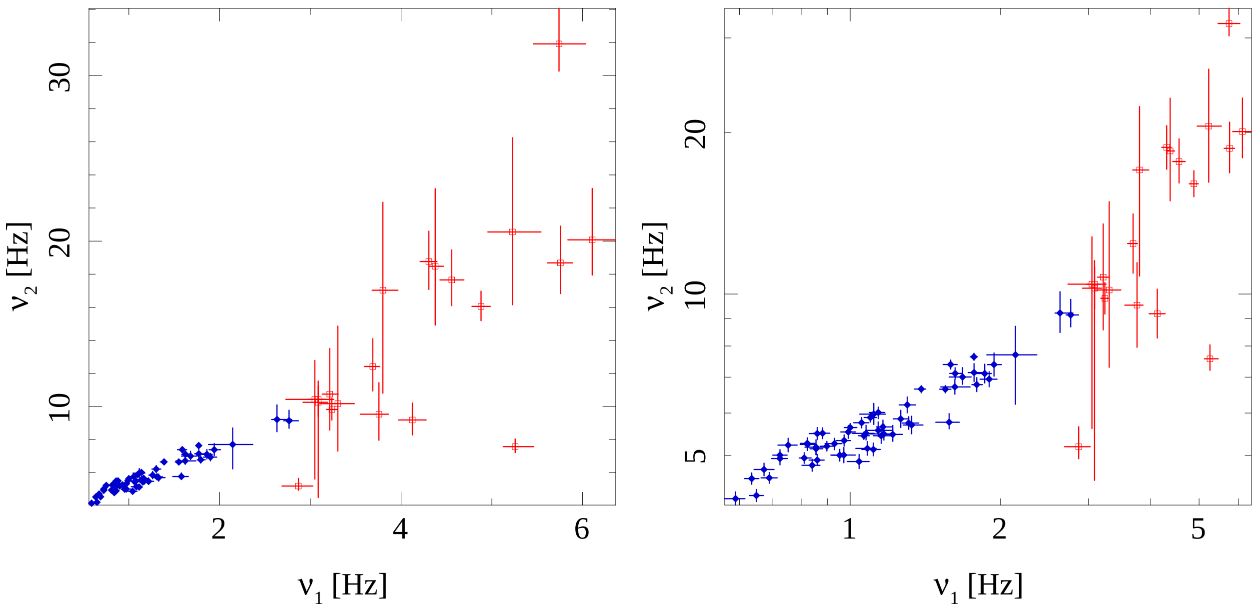

Figure 5.14: The peak frequency $\nu_{2,\mathrm{low}}$ of the second Lorentzian as a function of the one of the first one $\nu_{1,\mathrm{low}}$. The filled diamonds (blue) are the values of the peak frequencies for hard and intermediate state, whereas the empty boxes (red) correspond to the soft state data ($\Gamma > 2.43$). A linear plot is shown in the left panel and a logarithmic one on the right side. For the high energy data the relation looks quite similar.

Table 5.1: Correlations between the peak frequencies ν_1 and ν_2 in the low and in the high energy band. The fit parameters obtained for PSDs of soft states ($\Gamma_1 > 2.43$) were ignored in certain cases. This improves the correlation due to the fact that ν_2 is no reliable value for soft states. In this table the correlation coefficient ρ for the respective values is given, it is noted if the soft state data have been ignored and a linear fit to the data is presented. The expression $\log \nu_i$ corresponds to $\log(\nu_i/\mathrm{Hz})$. The logarithm was used to figure out if ν_1 and ν_2 are related via a power law.

values	with soft states	ρ	linear correlation
$\nu_{1,\mathrm{low}}, \nu_{2,\mathrm{low}}$	yes	0.88	$\nu_{2,\mathrm{low}} = (3.13 \pm 0.04)\,\mathrm{Hz} + (2.26 \pm 0.03)\nu_{2,\mathrm{low}}$
$\nu_{1,\mathrm{low}}, \nu_{2,\mathrm{low}}$	no	0.96	$\nu_{2,\mathrm{low}} = (2.95 \pm 0.04)\,\mathrm{Hz} + (2.45 \pm 0.04)\nu_{2,\mathrm{low}}$
$\log \nu_{1,\mathrm{low}}, \log \nu_{2,\mathrm{low}}$	yes	0.91	$\log \nu_{2,\mathrm{low}} = (0.74 \pm 0.00) + (0.55 \pm 0.02) \log \nu_{2,\mathrm{low}}$
$\log \nu_{1,\mathrm{low}}, \log \nu_{2,\mathrm{low}}$	no	0.94	$\log \nu_{2,\mathrm{low}} = (0.74 \pm 0.00) + (0.48 \pm 0.02) \log \nu_{2,\mathrm{low}}$
$\nu_{1,\mathrm{high}}, \nu_{2,\mathrm{high}}$	yes	0.92	$\nu_{2,\mathrm{high}} = (3.94 \pm 0.04)\,\mathrm{Hz} + (1.86 \pm 0.03)\nu_{2,\mathrm{high}}$
$\nu_{1,\mathrm{high}}, \nu_{2,\mathrm{high}}$	no	0.96	$\nu_{2,\mathrm{high}} = (3.86 \pm 0.04)\,\mathrm{Hz} + (1.94 \pm 0.04)\nu_{2,\mathrm{high}}$
$\log \nu_{1,\mathrm{high}}, \log \nu_{2,\mathrm{high}}$	yes	0.94	$\log \nu_{2,\mathrm{high}} = (0.77 \pm 0.00) + (0.43 \pm 0.01) \log \nu_{2,\mathrm{high}}$
$\log \nu_{1,\mathrm{high}}, \log \nu_{2,\mathrm{high}}$	no	0.95	$\log \nu_{2,\mathrm{high}} = (0.77 \pm 0.00) + (0.38 \pm 0.02) \log \nu_{2,\mathrm{high}}$

5.2.5 Energy Dependence

The peak frequencies of the Lorentzian profiles are similar in both energy ranges, despite that there are significant differences between the low energy PSD and the one for the high energy. Fig. 5.17 shows the shapes of two PSDs computed for the same observation but in different energy bands.

The most obvious disparity between the energy bands is the distinction of the first hump in the PSD. The contribution of the corresponding frequencies to the total variability of the low energy light curve is larger than to that of the high energy light curve. As power spectra are modeled

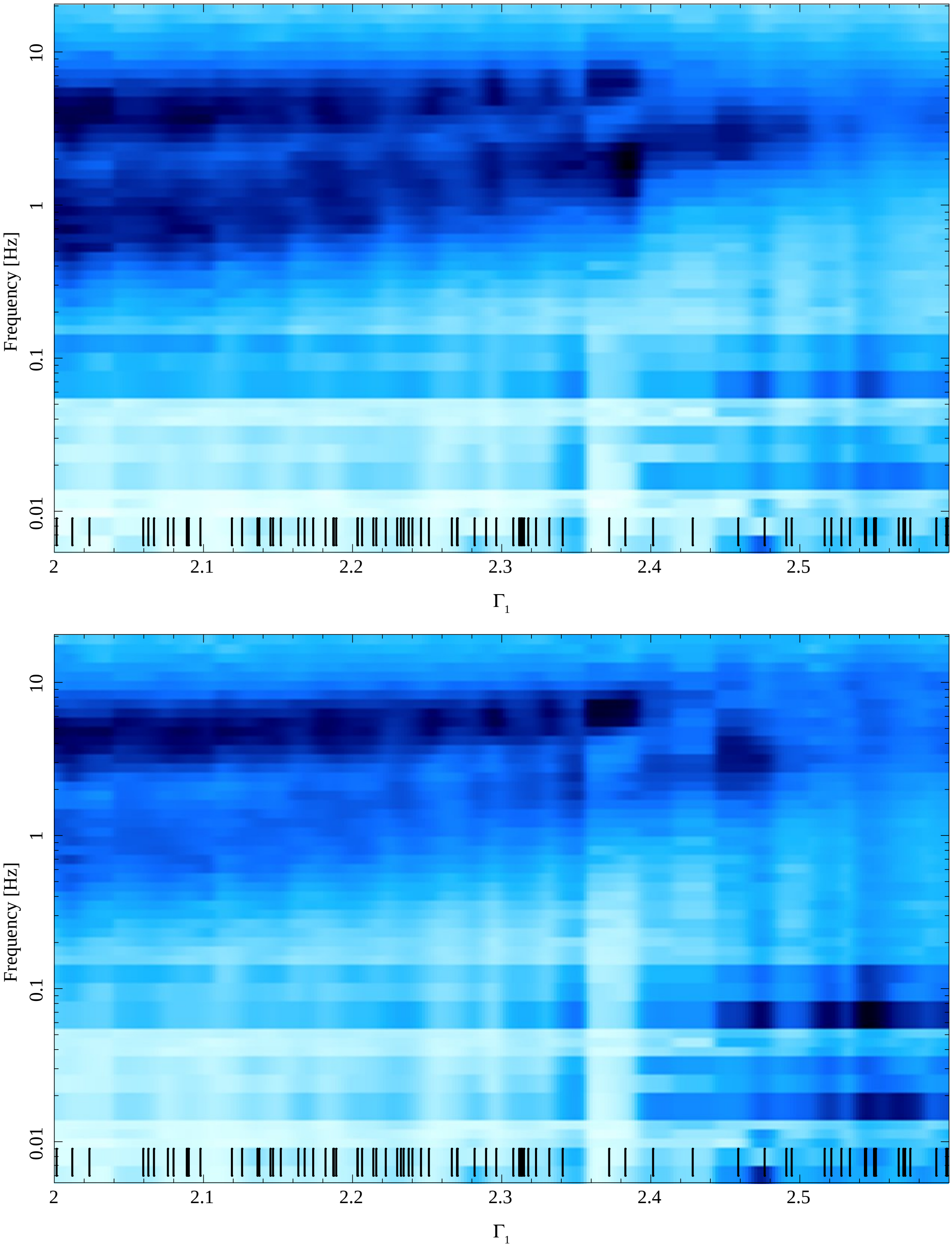

Figure 5.15: The power spectral density as a function of the photon index. For each observation the power spectrum multiplied with the frequency is plotted at the value of the corresponding photon index, which is indicated by a short line at the bottom. An interpolation was realized to get a continuous picture from the discrete values of the photon index. Larger values of PSD(f) × f are coded by a darker color. The two humps of the PSDs can be seen clearly. This was done for the low (top) and high energy band (bottom).

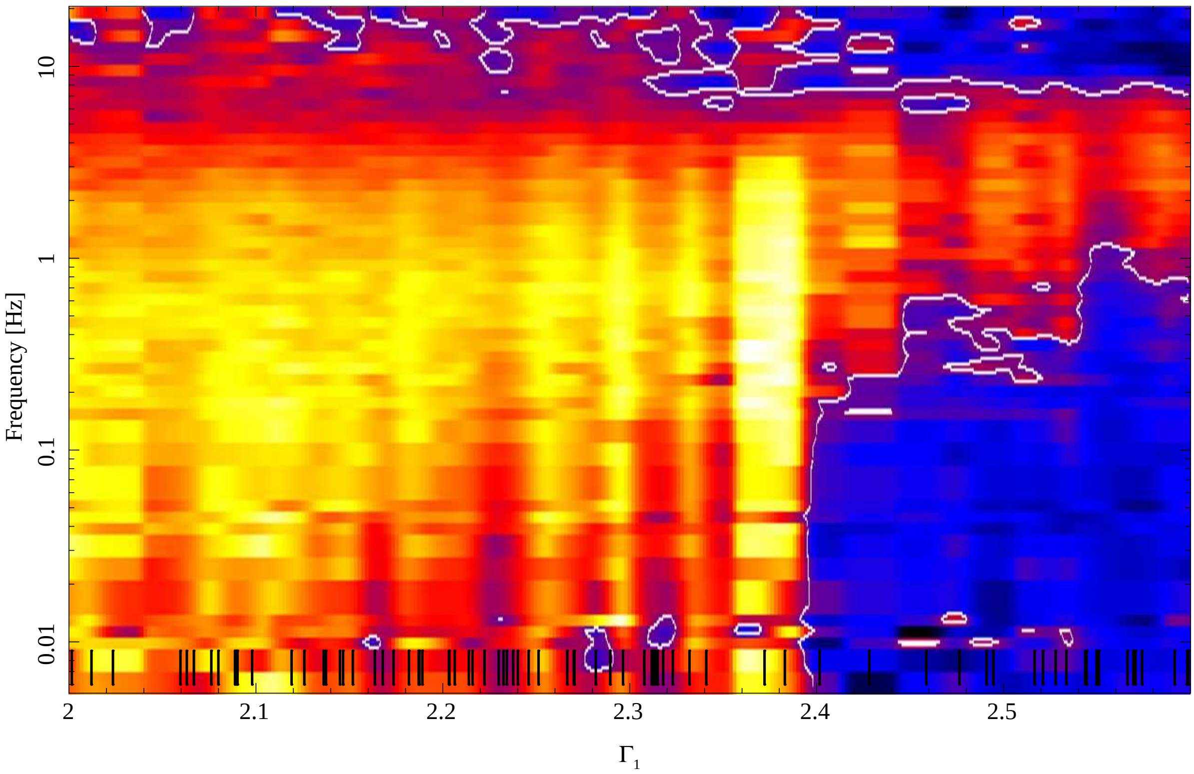

Figure 5.16: Color-coded relative difference between the PSDs in the low and high energy band, i.e. $(\mathrm{PSD}_{\mathrm{low}} - \mathrm{PSD}_{\mathrm{high}})/(\mathrm{PSD}_{\mathrm{low}} + \mathrm{PSD}_{\mathrm{high}})$, which is shown in the same format as Fig. 5.15. The white line is the $\mathrm{PSD}_{\mathrm{low}} = \mathrm{PSD}_{\mathrm{high}}$ contour. Yellow and red correspond to $\mathrm{PSD}_{\mathrm{low}} > \mathrm{PSD}_{\mathrm{high}}$. A comparison with Fig. 5.15 shows that the Lorentzian L_1 is larger in the low energy band, whereas L_2 obtains identical values in both energy bands.

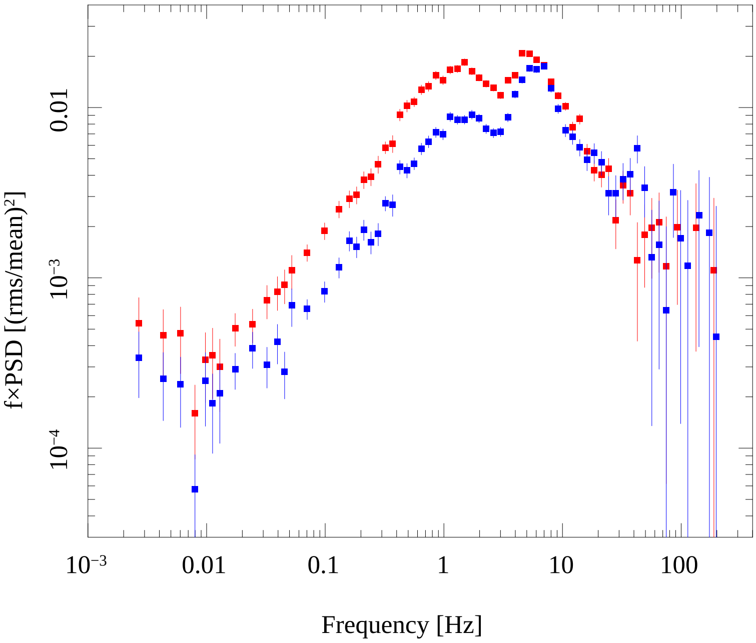

Figure 5.17: The power spectral density of the low energy band (red) compared to a PSD which was computed from the same observation but in the high energy band (blue). It attracts attention that the hump being located at lower frequencies is much less distinctive in the high energy band. This can be seen clearly in Fig. 5.15, too.

Table 5.2: Correlation coefficients and linear relations between peak frequencies and photon index Γ_1.

values	with soft states	ρ	linear correlation
$\nu_{1,\mathrm{low}}, \Gamma_1$	yes	0.89	$\nu_{1,\mathrm{low}}/\mathrm{Hz} = (-19.66 \pm 0.05) + (9.33 \pm 0.02) \times \Gamma_1$
$\nu_{1,\mathrm{low}}, \Gamma_1$	no	0.79	$\nu_{1,\mathrm{low}}/\mathrm{Hz} = (-10.19 \pm 0.04) + (5.11 \pm 0.02) \times \Gamma_1$
$\log(\nu_{1,\mathrm{low}}/\mathrm{Hz}), \Gamma_1$	yes	0.94	$\log(\nu_{1,\mathrm{low}}/\mathrm{Hz}) = (-4.16 \pm 0.01) + (1.89 \pm 0.00) \times \Gamma_1$
$\log(\nu_{1,\mathrm{low}}/\mathrm{Hz}), \Gamma_1$	no	0.82	$\log(\nu_{1,\mathrm{low}}/\mathrm{Hz}) = (-3.75 \pm 0.01) + (1.70 \pm 0.01) \times \Gamma_1$
$\nu_{2,\mathrm{low}}, \Gamma_1$	yes	0.90	$\nu_{2,\mathrm{low}}/\mathrm{Hz} = (-17.81 \pm 0.05) + (8.56 \pm 0.02) \times \Gamma_1$
$\nu_{2,\mathrm{low}}, \Gamma_1$	no	0.79	$\nu_{2,\mathrm{low}}/\mathrm{Hz} = (-11.73 \pm 0.04) + (5.83 \pm 0.02) \times \Gamma_1$
$\log(\nu_{2,\mathrm{low}}/\mathrm{Hz}), \Gamma_1$	yes	0.94	$\log(\nu_{2,\mathrm{low}}/\mathrm{Hz}) = (-4.06 \pm 0.01) + (1.85 \pm 0.00) \times \Gamma_1$
$\log(\nu_{2,\mathrm{low}}/\mathrm{Hz}), \Gamma_1$	no	0.82	$\log(\nu_{2,\mathrm{low}}/\mathrm{Hz}) = (-4.05 \pm 0.01) + (1.85 \pm 0.01) \times \Gamma_1$

Table 5.3: Quantification of the correlations and relations between the rms_i of each Lorentzian in the different energy bands.

values	with soft states	ρ	linear correlation
$\mathrm{rms}_{1,\mathrm{low}}, \mathrm{rms}_{1,\mathrm{high}}$	yes	0.23	Fit does not converge.
$\mathrm{rms}_{1,\mathrm{low}}, \mathrm{rms}_{1,\mathrm{high}}$	no	0.62	$\mathrm{rms}_{1,\mathrm{high}} = (-0.11 \pm 0.00) + (1.26 \pm 0.01)\mathrm{rms}_{1,\mathrm{low}}$
$\mathrm{rms}_{2,\mathrm{low}}, \mathrm{rms}_{2,\mathrm{high}}$	yes	0.75	$\mathrm{rms}_{2,\mathrm{high}} = (0.07 \pm 0.00) + (0.51 \pm 0.01)\mathrm{rms}_{2,\mathrm{low}}$
$\mathrm{rms}_{2,\mathrm{low}}, \mathrm{rms}_{2,\mathrm{high}}$	no	0.87	$\mathrm{rms}_{2,\mathrm{high}} = (0.05 \pm 0.00) + (0.66 \pm 0.01)\mathrm{rms}_{2,\mathrm{low}}$

with Lorentzians and each of them can be identified with an hump in the PSD, the difference of variability discussed above can be quantified directly. Using the fit parameters of the power spectrum, the rms_i of the Lorentzian L_i can be calculated directly according to equation 5.18. The relation between $\mathrm{rms}_{1,\mathrm{low}}$ and $\mathrm{rms}_{1,\mathrm{high}}$ is illustrated in Fig. 5.19. Fig. 5.18 shows the same for L_2.

The plots confirm that the second Lorentzian has a similar contribution to the total variability in the low and the high energy band, whereas it is different for the first Lorentzian, whose rms is larger in the low energy band. But in both cases the correlation between $\mathrm{rms}_{i,\mathrm{low}}$ and $\mathrm{rms}_{i,\mathrm{high}}$ is much better for hard and intermediate states than for soft states. Corresponding correlation coefficients and linear relation fits can be found in table 5.3.

A reason for the decline of the correlations of the rms after the state transition can be seen in Fig. 5.12. As there are two Lorentzians available for fitting, but in the most cases only one hump is found in the power spectra, similar problems, as described in section 5.2.3, occur. The rms is distributed between the Lorentzians. Also the partition of rms_1 and the rms of the power law can distort the relation between $\mathrm{rms}_{1,high}$ and $\mathrm{rms}_{1,low}$. As the second Lorentzian is not important for power spectra of soft state observations, using only the power law and one Lorentzian to fit these PSDs would probably be a possibility to improve the rms correlations for the first Lorentzian.

A hardness intensity diagram, which is colored according to the total rms of the corresponding observations is shown in Fig. 5.21. In the low energy channel the rms decreases with the hardness throughout hard and soft state, whereas there is different behavior of the rms in the high energy channel. Here, the largest rms is found during the soft state at high count rates.

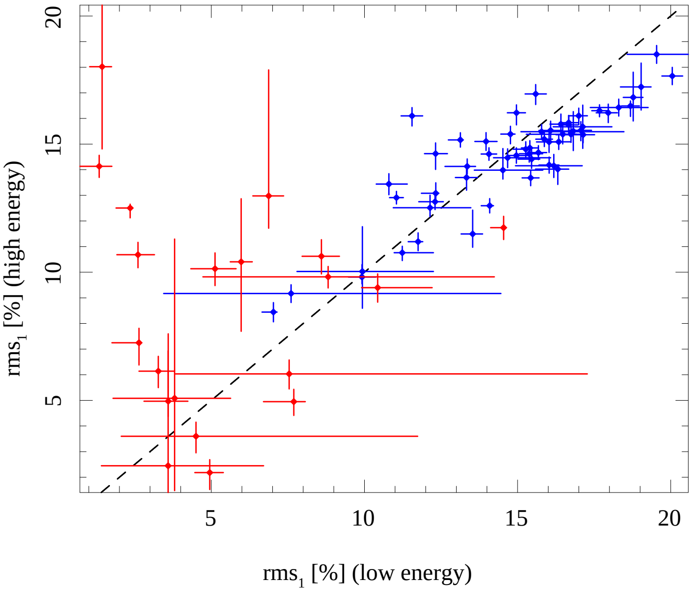

Figure 5.18: Energy dependence of the rms of the second Lorentzian. The dashed line is the identity, which corresponds to $\mathrm{rms}_{2,\mathrm{high}} = \mathrm{rms}_{2,\mathrm{low}}$. It indicates that rms_2 has a comparable value in both energy ranges. There is a better correlation for the hard and intermediate state data (blue symbols). This is again caused by the fact that the second Lorentzian component vanishes in soft states.

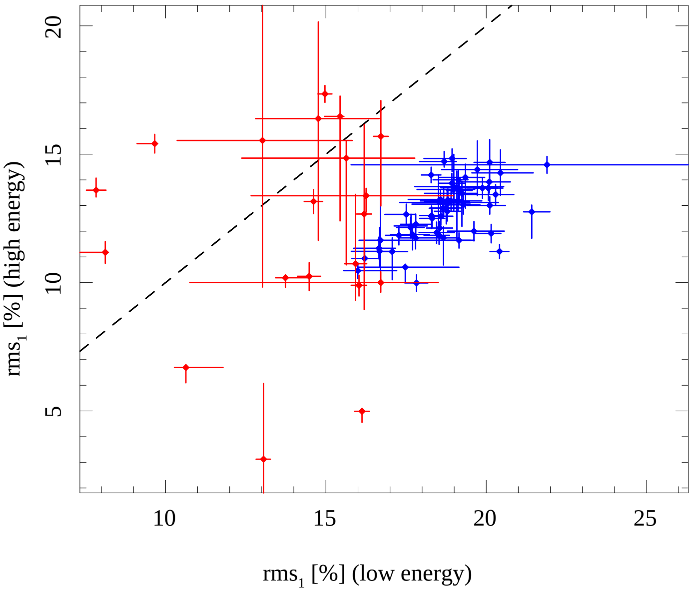

Figure 5.19: $\mathrm{rms}_{1,\mathrm{high}}$ as a function of $\mathrm{rms}_{1,\mathrm{low}}$. As in Fig. 5.19 the dashed line indicates the identity. The difference between soft state data (red) and the data obtained for hard and intermediate states (blue) is large for the rms of the first Lorentzian. During hard and intermediate states $\mathrm{rms}_{1,\mathrm{high}}$ is always smaller than $\mathrm{rms}_{1,\mathrm{low}}$, which was already mentioned in Fig. 5.17. One reason for the higher variability of the rms_1 values for soft states (red) is the cutoff power law, whose contribution to the total rms is large for soft states. As described below (Fig. 5.12) there is not always a reliable partition of the total rms between the components of the fit model in these cases. For that reason the values of rms_1, which were given by fit parameters, have only a small validity, consequently they are uncorrelated in the case of a soft state.

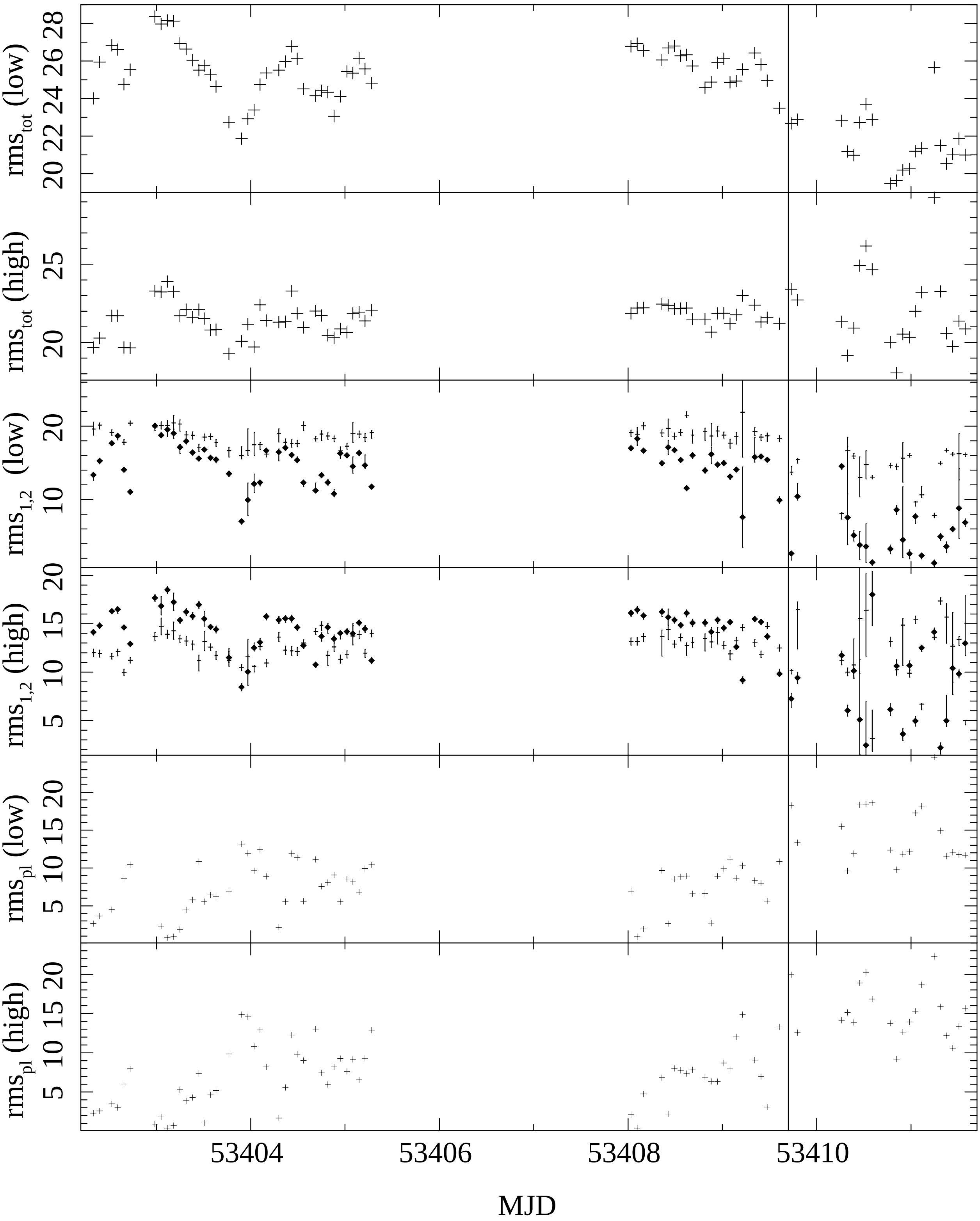

Figure 5.20: Summary of the total rms and the rms of the components in both energy bands. For the rms of the first Lorentzian crosses are used. The filled diamonds correspond to the rms of the second Lorentzian rms_2. After the transition to the soft state, which is indicated with a vertical line, the partition between the components is problematic.

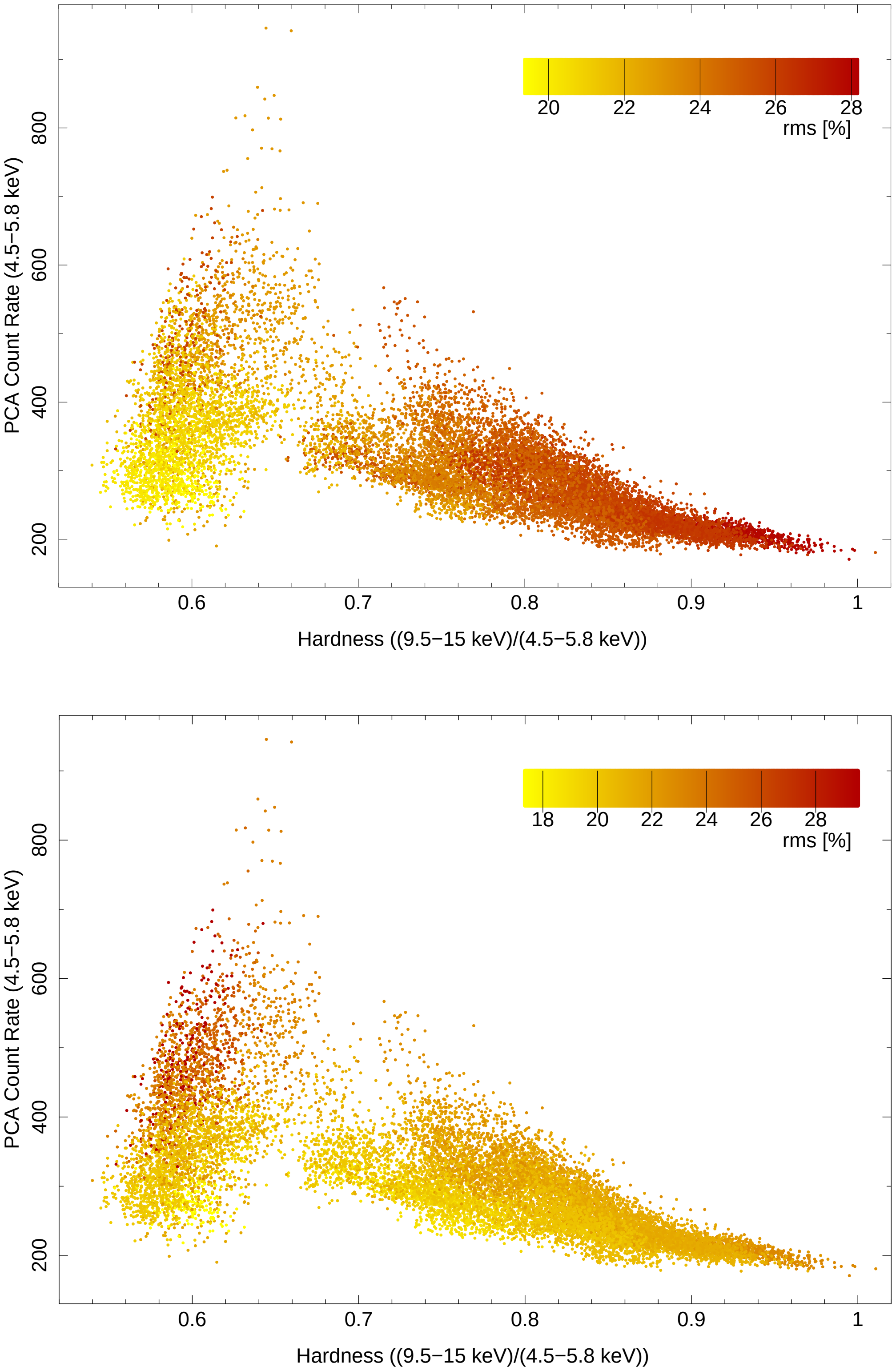

Figure 5.21: A hardness intensity diagram, which is color-coded by the values of the rms. The HID in the upper panel is colored by the rms in value in the low energy band and the color-code in the panel below corresponds to the rms in the high energy channel.

5.3 Coherence

Coherence is a degree of linear correlation between two processes. Here these processes are two time series $s(t)$ and $h(t)$. They were obtained simultaneously in different energy bands. For consistence the same bands as for the hardness intensity diagram and the power spectra were used. The low energy range was ~4.5–5.8 keV (PCA channels 11–13) and the high energy range ~9.5–15 keV (PCA channels 23–35).

As introduced by Vaughan & Nowak (1997), to describe the correlation between the two light curves, a correlation function $\gamma(f_j)$ depending on the Fourier frequency f_j (Eq. 5.11) is introduced. The correlation function is based on the cross power density C_j, which is defined by:

$$C(f_j) = S^*(f_j)H(f_j) \tag{5.30}$$

where S and H are the discrete Fourier transforms (Eq. 5.10) of s and h, respectively. Generally $C(f_j)$ is a complex quantity. Analogous to the computation of the power spectral density, $C(f_j)$ is calculated for several segments of the analyzed light curves and then averaged. The coherence function is defined by the absolute value of the averaged $C(f_j)$ normalized such that $\gamma(f_j) \in [0,1]$ (Vaughan & Nowak, 1997, Eq. (2)).

$$\gamma^2(f_j) = \frac{|\langle S^*(f_j)H(f_j)\rangle|^2}{\langle |S(f_j)|^2\rangle\langle |H(f_j)|^2\rangle} \tag{5.31}$$

The important point is averaging $C(f_j)$ over several segments. Using the definition of the coherence function (5.31) it is easy to see how perfect coherence ($\gamma^2(f_j) = 1$) can be obtained. Averaging over N segments, for a given Fourier frequency f_j, results in:

$$\gamma^2 = \frac{\left|\frac{1}{N}\sum\limits_{n=1}^{N} {S_n}^* H_n\right|^2}{\left(\frac{1}{N}\sum\limits_{n=1}^{N} |S_n|^2\right)\left(\frac{1}{N}\sum\limits_{n=1}^{N} |H_n|^2\right)} = \frac{\sum\limits_{n,k=1}^{N} {S_n}^* S_k H_n {H_k}^*}{\sum\limits_{n,k=1}^{N} S_n {S_n}^* H_k {H_k}^*} \tag{5.32}$$

Numerator and denominator are equal, and hence $\gamma = 1$, if the relation

$$H_n = aS_n \tag{5.33}$$

holds for each segment n with the same constant $a \in \mathbb{C}$. The coherence function therefore measures the degree to which a is constant for the different segments. a can, however, depend on the Fourier frequency, such that one has to introduce, in general, a function Tr(f):

$$H(f) = T_r(f)S(f) \tag{5.34}$$

T_r is the Fourier transformation of the transfer function t_r between the light curves s and h:

$$h(t) = \int_{-\infty}^{+\infty} t_r\,(t-\tau)\,s(\tau)d\tau \tag{5.35}$$

The coherence function can be deduced from such a transfer function. The mathematical derivation is described in more detail in Vaughan & Nowak (1997). It can be illustrated geometrically how the coherence function measures the degree of linear correlation. The complex quantity $C(f_j)$ can be considered as a vector in the complex plane.

$$C = S^*H = |S||H|e^{i(\Phi_H - \Phi_S)} \tag{5.36}$$

Averaging C over N segments of the light curve means by definition to sum up all vectors C and to multiply the resulting vector by $1/N$. The vector addition is shown in Fig. 5.22. The maximum

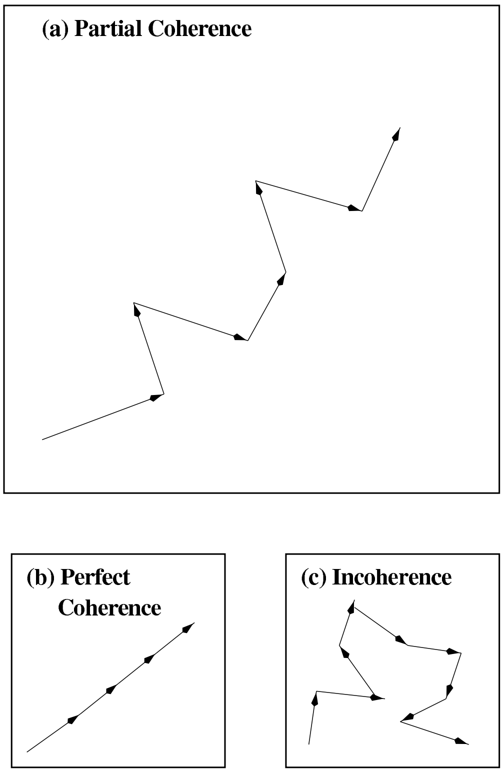

Figure 5.22: Geometrical illustration of the mean value of the cross power density $C(f_i)$. The complex quantity $C_n(f_i) = S_n{}^*(f_i)H_n(f_i)$ for each segment n corresponds to a vector in the complex plane. The sum over the segments can be visualized by a vector addition (a). Perfect coherence is shown in (b), where $\left|\sum_n C_n(f_i)\right| = \sum_n |C_n(f_i)|$ is valid. (c) is an example for incoherence. The phase of $C_n(f_i)$ varies strongly from one segment to another. (picture from Nowak et al. (1999a) Fig. 3)

absolute value of this sum, is obtained if each vector points in the same direction. This means mathematically that C has the same phase for each segment $n \in [1, 2, ..., N]$:

$$\Phi_{C_n} = \arg(C_n) = \Phi_{H_n} - \Phi_{S_n} \tag{5.37}$$

If H_n and S_n are related via a constant factor $a \in \mathbb{C}$ (5.33) for all n, the phase of the cross power density is constant: $C_n = \arg(S_n{}^* S_n a) = \arg(a)$

As discussed above, coherence is a function of the Fourier frequencies. The typical frequency dependence of the coherence function of a observation of Cygnus X-1 is shown in Fig. 5.23. To quantify the coherence between the low and the high energy light curve of a complete observation with a single value, the coherence function is averaged over the 3.2–10 Hz band. This frequency range is an appropriate choice, because on the one hand a crucial fraction of the variability of the analyzed light curves occurs between 3.2–10 Hz and on the other hand these are also meaningful frequencies to compute the time lags. The lags depend as well on the Fourier frequencies and will be discussed in the following. Calculating a time lag between two time series makes only sense if the series are correlated. For that reason time lags and coherence are evaluated in the same frequency range.

5.4 Time Lags

5.4.1 Definition

Between two correlated time series there can be a delay or time lag. Again the low and high energy light curves $s(t)$ and $h(t)$ are considered. The time lag depends on the Fourier frequency and can be obtained by computing the cross power density (5.30) of s and t. The time lag $\delta_t(f_i)$ is defined by:

$$\delta_t(f_i) = \frac{\arg[C(f_j)]}{2\pi f_i} = \frac{\arg[S^*(f_j)H(f_j)]}{2\pi f_i} = \frac{\Phi_{H(f_j)} - \Phi_{S(f_j)}}{2\pi f_i} \tag{5.38}$$

where $S(f_j)$ and $H(f_j)$ are again the discrete Fourier transformations of the light curves and where $\Phi_{S(f_j)}$ and $\Phi_{H(f_j)}$ are the corresponding phases. Obviously positive and negative lags are possible.

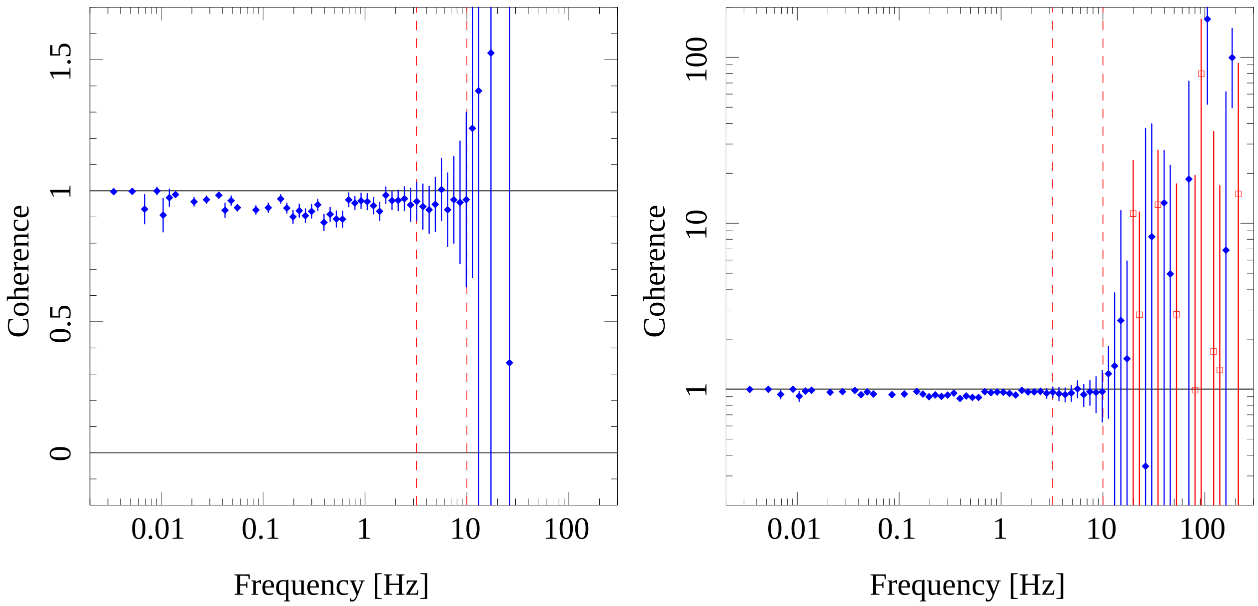

Figure 5.23: The frequency depending coherence of a Cygnus X-1 observation. The left panel shows a linear plot of the coherence. To describe the coherence of one observation with a scalar, the coherence function is averaged over the frequency range 3.2–10 Hz. This range is indicated by the two vertical dashed lines. Especially above 10 Hz several numerically calculated values of the coherence are located out of the interval [0,1]. The right plot shows the same data logarithmically. Here, the empty boxes, which are plotted in red, represent negative values. They were multiplied by -1 for the plotting.

By definition a positive lag means that events occurring in the light curve of the soft energy band are detected in the high energy light curve after a time delay.

A detailed description of the time lags, including the computation, the noise estimation and their statistical uncertainties is given by Pottschmidt (2002, Ch. 3.5).

For Cygnus X-1 it has turned out that the high energy band lags behind the soft energy band, thus positive time lags are measured. Analogous to the coherence, the time lags are average over the 3.2–10 Hz frequency band. This mean value will be called time lag of an observation in the following. The typical dependence of the time lags on the Fourier frequencies is shown in Fig. 5.24.

5.4.2 Behavior of the Lags

Using the time lag of each of the 78 observations, the behavior of the lags during the 10 days of observation can be analyzed. A corresponding plot is shown in Fig. 5.25. It includes the coherence and the light curve in the low energy band (4.5–5.8 keV), which was obtained with the PCA. The coherence is an important value to measure the reliability of the lag, as a lag makes only sense between two correlated light curves. To compare the lags with the light curve itself, is necessary to figure out if it is correlated with the count rate. Additionally Fig. 5.25 includes the peak frequencies of the Lorentzians and the total rms in the low energy light curve, in order to give an overview of the relations. It attracts attention that the behavior of the lag changes with the states. Whereas the variation is continuous and smooth before the transition, it seems to vary between about 2 ms and 11 ms chaotically after the transition to the soft state, at first sight. The results can be compared to the ones from long term observation by Pottschmidt et al. (2003). They calculated lags of about 2–3 ms for typical hard states and found that the lags increase with the count rate. Here, this effect can be seen clearly in the results before the transition. The lag is correlated with the mean count rate. In contrast to the results of the long term observation the lags are significantly larger

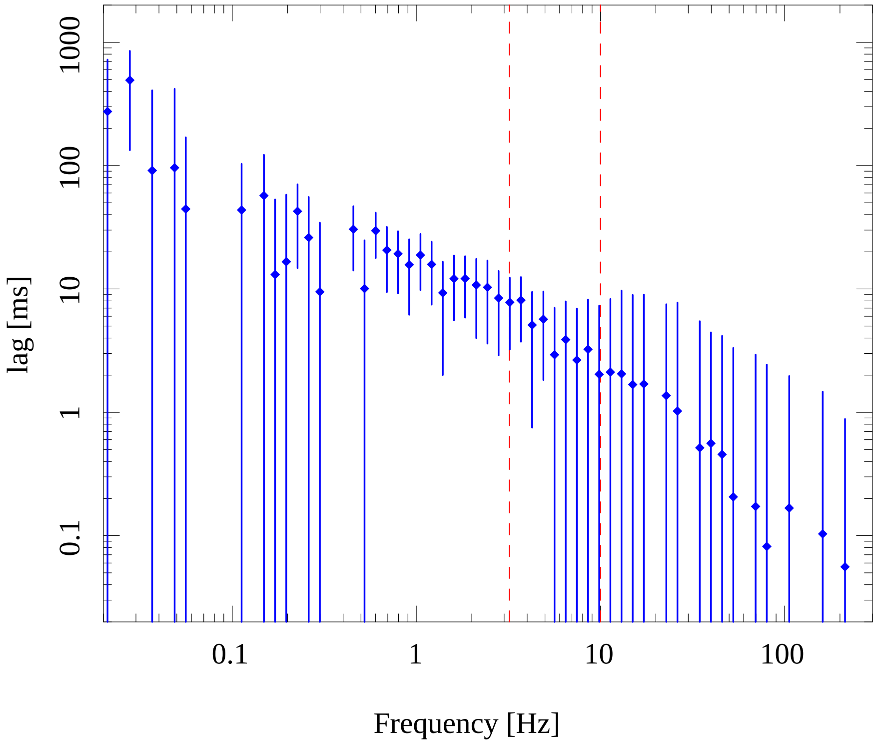

Figure 5.24: The typical lag spectrum of an observation of Cygnus X-1. The quantity being called time lag in the following, is the mean value between 3.2 and 10 Hz. In the plot these frequencies are highlighted by dashed lines.

than 2 ms, but that can be explained easily. There are no typical hard states included in the data analyzed here. As already mentioned the photon index varies between 2.0 and 2.6, which is the typical range for intermediate states. For these states there is more soft X-ray radiation than for hard states and thus it is expected that the time lags are also larger. The behavior of the lags changes essentially after the transition. Here, coherence changes rapidly and also the time lags vary strongly between 2 and 11 ms and the correlation between time lag and count rate seems to disappear. But a closer look on the results reveals that the variation of the time lags is not random. For the small time lags the coherence is quite close to one and exactly these cases are the observations with the highest count rates. This effect can be seen in Fig. 5.26. For the other soft state observations the lags are larger, namely up to 11 ms. In addition the corresponding coherence is lower in most cases. If the observations with these small lags would be excluded, the effect that the lags increase with increasing count rate would hold for the total data, at least within the errors. For that reason it had to be checked if the time lags are indeed that small, and not caused by a wrong calculation. The high coherence indicates that the time lags are well-defined in these cases. As a reason for the small lags also the phase of the cross power density was considered, which is used for the calculation of the time lags. A phase is only defined modulo 2π and adding 2π to the phase would increase the lags. Contemplating Eq. 5.38 points out that a shift of $\pm 2\pi$ of the phase would change the time lag by the value $\pm 1/f$. As the lag is averaged over the frequencies between 3.4 and 10 Hz, such a shift would change the time lag by about 100–300 ms. Thus phase shifts can be excluded as possible reasons for the behavior of the lags. The same is the case for effects caused by the detector. For example detector dead time was taken into account, as the small lags occur only at the highest count rates. But as dead time is a random effect, and the coherence is defined by averaging over segments of the light curve, dead time decreases the coherence significantly, and thus does not come into question as explanation. The behavior of the lags is obviously caused by

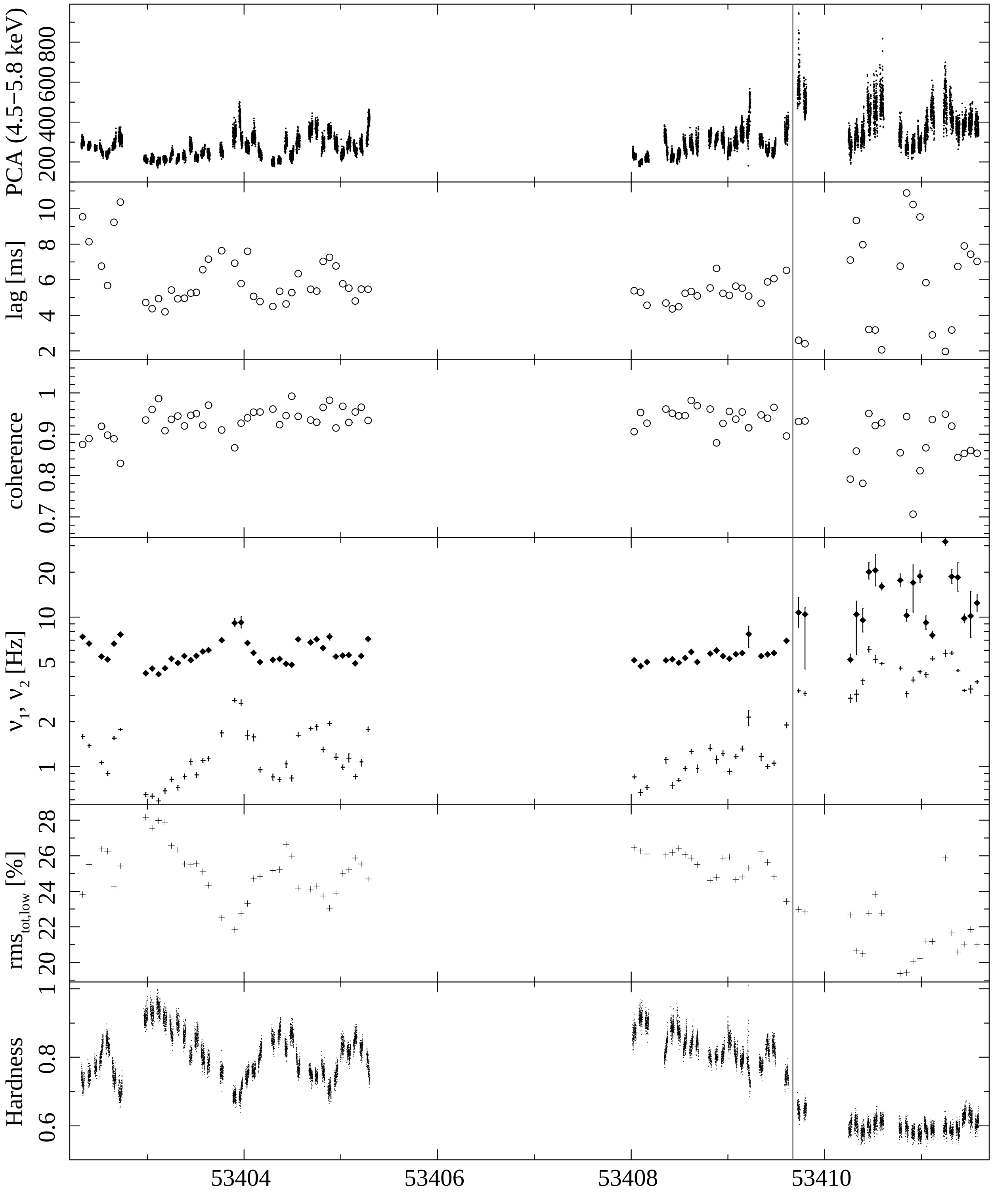

Figure 5.25: Summary of the behavior of the characteristic timing parameters during the total observation. The transition to the soft state is indicated by a vertical line. The light curve in the top panel shows the variability of Cyg X-1 in the low energy band. Time lags and coherence is plotted below. Additionally the peak frequencies $\nu_{1,2}$ of the Lorentzians are shown, where the crosses correspond to ν_1 and the filled diamonds to ν_2. The rms of the low energy channel is shown below and the hardness is plotted in the bottom panel.

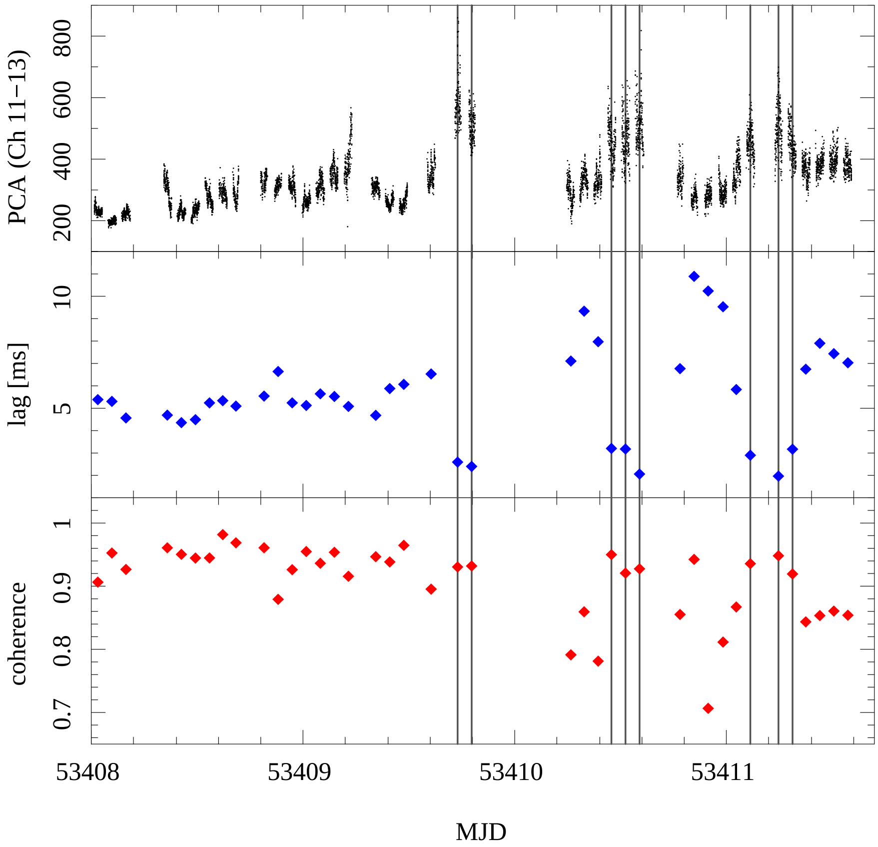

Figure 5.26: Detailed view of the low energy light curve, the time lags and the coherence. The strange behavior of the lags after the transition, at MJD $\sim$ 53409.7, which was already shown in Fig. 5.25, is not completely unpredictable but has a specific structure. If the count rate is high enough the lag drops to about 2–3 ms. As the two energy bands are highly coherent here, the time lag is a reliable value in these cases. For lower count rates, the coherence decreases and the time lags increase significantly. This happens within hours. All data being obtained after the transition were classified as soft state observations by the spectral analysis.

the source. Pottschmidt et al. (2003) also found that the time lags in typical soft states were quite small with values of 2–3 ms. In the long term observation photon indices which were larger than 3 were found, whereas $\Gamma_1 \approx 2.6$ was the largest photon index in the data analyzed here. The question arises, if it makes sense to subdivide the soft state. The behavior of the time lags indicates that something in the underlying emission processes of the black hole changes, whereas no difference in the spectral parameters is observed. After the transition the hardness ratio remained almost constant (Fig. 5.25) and the spectral fitting parameters did not change, too (Fig. 4.10). In the same period of time the lags showed the described behavior. A color-coded hardness intensity diagram is shown in Fig. 5.27. As discussed at Fig. 4.8 two states can be clearly distinguished. Plotting the data with colors characterizing the lag of the corresponding observation reveals that there is a fixed allocation of time lags in the hardness intensity diagram. In the accumulation of points at larger hardness, which is classified as hard or hard intermediate state, the time lags increase with decreasing hardness. It is completely different for the points which are associated with the soft state. Here the lags do not depend on the hardness, but vary with the count rate. This is just an illustration of the effect discussed above, namely that the lag drops to 2–3 ms at high count rates, whereas high time lags are observed for lower count rates in the soft state. A problem in this illustration is, that different time scales are used for the plotted data and their coloring. The

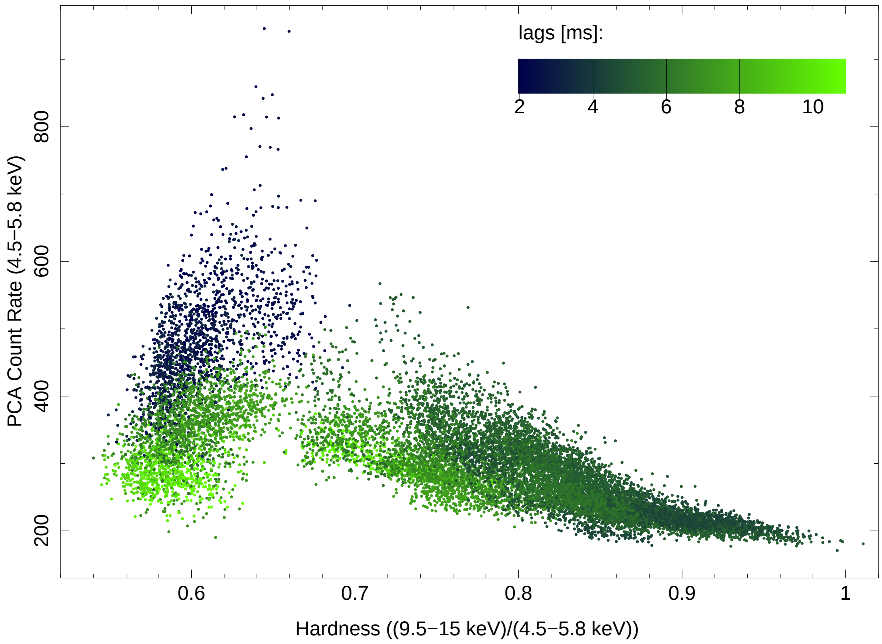

Figure 5.27: The hardness intensity diagram shown in Fig. 4.8 colored according to the lags.

time lags are calculated for a total observation with a mean exposure time of about 3 ks, whereas the time resolution of the used light curves is 16 s. For that reason several different points in the hardness intensity diagram are colored with the same color, this can cause an overlap of the colors. A more detailed allocation of time lags in this illustration could possibly be achieved by using the same time scale for the data in the diagram and the coloring, i.e. calculating the time lag for small segments of the light curves and then plotting only the mean hardness and count rate of each segment with the corresponding color. But the used illustration is still accurately enough to show a specific distribution of time lags in the hardness intensity diagram and thus confirms the idea to subdivide the soft state into two different states. Comparing Fig. 5.27 with a detailed overview of the different states (Fig. 2.10) conveys that the state with a soft spectrum, high count rate and small time lags can be identified with the soft intermediate state. The state which has also a soft spectrum, but a lower count rate and large time lags could then be considered as the soft state. The other observations analyzed in this work would then correspond to the hard intermediate state, as it was mentioned several times that no typical hard states were found in this work.

For a confident assignment of the states, it would be necessary to analyze more data. As indicated by the values of the photon indices, only a section of the states is covered by the data used here. Reproducing Fig. 5.27 including more data, especially with $\Gamma_1 < 2$ and $2.6 < \Gamma_1$, and comparing it with Fig. 2.10, would probably allow a good classification of the states of Cyg X-1.

5.4.3 Origin of the Time Lags

Time lags are a very helpful quantity to figure out the underlying processes, which cause the characteristic emission of X-ray binaries such as Cyg X-1. Models explaining their spectra must include a description for the behavior of the lags. The most important characteristics of the lags are the fact that the high energy has a delay versus the low energy and the dependence of the lags δ_t on the Fourier frequencies f_i, which is shown in Fig. 5.24. The relation between $\delta_t(f_i)$ and f_i can be approximated with $\delta_t(f_i) \propto f_i^{-\beta}$, where $\beta \approx -0.7$. Note that such a power law roughly describes the overall shape of the time lags as a function of the Fourier frequencies. This dependence shows substructures, which clearly differ from a power law relation. There are different models which roughly describe the spectrum and the time lags (Nowak et al., 1999b; Körding &

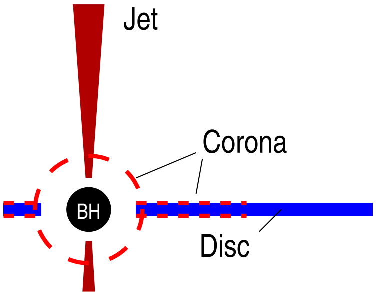

Figure 5.28: Possibly structure of the surrounding of an accreting black hole. The accretion disk and the spherical corona form the so called "sphere + disk" model. In addition a jet is illustrated here. (Wilms, priv. comm.)

Falcke, 2004). But none of the models is completely consistent with the total spectral and timing behavior of such sources. Up to now there is no commonly accepted explanation for that. It will be discussed in the following how the lags can be explained by using models that describe the spectral behavior (see Sect. 2.3). Several models are based on the so called "sphere + disk" geometry Compton corona model, consisting out of an accretion disk around a black hole, where the black hole is surrounded by a spherical corona. An illustration of this geometry is shown in Fig. 5.28. A first naive explanation of the $\delta_t(f_i) \propto f_i^{-0.7}$ relation of the time lags is found by considering the "sphere + disk" geometry and the Keplerian frequencies, which was described in Sect. 5.1.3. If soft X-rays are emitted from an area orbiting in the accretion disk at a certain radius r, a modulation with the Keplerian frequency could be observed in this radiation. A part of this radiation can be up-scattered in the Compton corona and thus be detected as hard X-rays. The scattering process itself takes time, which will obviously depend on the number of scatterings. If the corona is located close to the black hole, the photons emitted at radius r need a specific time to reach the corona. For that reason a delay between the observed soft and hard X-ray emission is expected. In this model the mean delay depends on the inclination of the accretion disk. But for a fixed inclination this delay increases linearly with the radius. There is a characteristic Keplerian frequency tied to r, which is given in Eq. 5.6. Using this formula one obtains:

$$\delta_t(f_i) \propto r_i \propto \left(\frac{c^3}{GMf_i} - a\right)^{\frac{2}{3}} = \left(\frac{c^3 - aGMf_i}{GMf_i}\right)^{\frac{2}{3}} \tag{5.39}$$

where the angular momentum of the black hole is again characterized by $a = cJ/(GM^2)$. It can be seen clearly that Eq. 5.39 yields the relation $\delta_t(f_i) \propto f_i^{-2/3}$ for small angular momenta $J \ll (GM^2)/c$. In this way the observed frequency dependence can be explained. As the PSDs measures the variability at different frequencies, it would then indicate how the emission is distributed over the radii, which correspond to these frequencies. The peak frequencies of the Lorentzians varied between about 0.5 and 30 Hz, which correspond to the radii 5.1×10^3 km and 3.3×10^2 km, respectively. It takes light about 1–17 ms to travel such distances. These time scales coincide with the observed time lags. But there are several arguments which prove that the time lags cannot originate from the discussed process. For example the behavior of the lags is one argument. As discussed in this work, the peak frequencies of the Lorentzians shift to higher frequencies if the photon index Γ_1 becomes larger, indicating that soft X-ray emission increases. Higher frequencies originate from smaller radii. According to this model, the time lags would decrease in this case but the contrary is observed. They increase, at least during the hard state. The biggest problem of this model are the energies of the X-rays. Here, it was assumed that the count rate, which was measured in the low energy band, was caused from emission in the accretion disk, whereas that in the high energy band was tied to processes in the corona. The low energy band covers the range 4.5–5.8 keV. These energies are quite high for the black body radiation of an accretion disk. Admittedly its temperature at the inner radius can reach up to 1 keV, but it decreases with the radius $T(r) \propto r^{-3/4}$ (Sect. 2.3.1). For that reason it is problematic to assume that the radiation showing a variability with a certain frequency was emitted at the corresponding radius with an energy of 4.5–5.8 keV. This model yields that the time lags occur only between specific energy bands. But Nowak et al.

(1999a) found that a delay was present between several energy bands. Obviously the model is wrong.

To figure out a model which describes all observed effects of the time lags, it is helpful to consider the origins of frequencies and lags as two different processes. This can be justified by the fact that the peak frequencies did not vary significantly during the soft and/or soft intermediate state of this observation, whereas the time lags changed strongly from one observation to the other (Fig. 5.25). The origin of the modulation of the observed frequencies, which was described above seems authentic. The values of the frequencies and corresponding radii are meaningful and there are no essential contradictions within the model of an accretion disk causing the observed modulations. For example Misra & Zdziarski (2008) describe how such a model can reproduce the typical PSDs of Cyg X-1 during a soft state. Several possible processes causing the time delays is discussed by Nowak et al. (1999b). They discuss the reprocession of the emission from the accretion disk in the corona, different diffusion times of hard and soft photons in the corona and the propagation of disturbances from the cold, outer disk into the hot, inner regions. However, they cannot determine which of their models is the most likely explanation of the lags. And there are even more other processes, which can in principle cause the observed time lags. Kylafis et al. (2008) introduce a jet model describing the time lags. In this model soft photons from the accretion disk are up-scattered in the jet, and several correlations, such as the relation between the time lag and the photon index Γ_1 can be reproduced.

All the models mentioned here do not explain the effect which was observed in this work, namely that the time lag drops to 2–3 ms for high count rates in the soft state. But neither for the presence of a Compton corona nor for that of a jet evidence can be found in this case, which is in coincidence with the assumption that the underlying process causing the time lag changes.

Chapter 6

Summary & Outlook

6.1 Summary

The X-ray source Cyg X-1 was observed quasi-continuously for 10 days in February 2005 with RXTE and the Ryle Telescope. The spectral analysis of the data revealed that a transition from the hard to the soft state occurred during this period of time. The two states are clearly separated in a hardness intensity diagram. The X-ray spectra in the energy range 4–200 keV were fitted with ISIS using different models, namely a phenomenological broken power law with exponential cutoff and a Comptonization model. Fits with similar quality were obtained with these models during the hard state, whereas the broken power law model fits the data better after the transition to the soft state. The temporal evolution of the resulting parameters and correlations between them were analyzed. The photon index Γ_1 of the broken power law increases with the count rate in the low energy light curve. In the soft state Γ_1 is larger than 2.4 and it does not vary significantly with the count rate. The two photon indices, which describe the spectral hardening above 10 keV, are clearly correlated. The correlation is identical to that, which was found in the long term analysis from 1999–2004 by Wilms et al. (2006). The photon indices vary strongly during the 10 days of observation, their values cover a large fraction of the total range which was obtained from the long-term analysis. The behavior of the source and its variability in time scale of days is similar to that in the time scale of years.

For the parameters obtained from the Comptonization fits no confidence intervals have been calculated due to computation time. The quality of the fits was however sufficient to state that the optical depth of the Comptonizing plasma is larger in the soft state than in the hard state and its temperature is smaller. This holds for both Comptonization components, which are a hot, optically thin plasma causing the continuum spectrum and a optically thick and cooler one. The first one corresponds to the corona and the second one represents a processed non-thermal disk radiation.

A self-consistent jet model, which yields a broad band spectrum from radio waves to hard X-rays, was applied to the observations with the hardest spectrum in this work, as this model was developed for a steady jet during the hard state. Radio and X-ray data can be fitted simultaneously with this model. It turned out that acceptable fits can be obtained.

As the spectra can be fitted with different models in a similar way, it is not possible to determine the underlying processes of the X-ray emission of the source only from spectral analysis. For that reason a timing analysis of the data was performed. Power spectral densities have been computed for each observation in two different energy bands. In a low energy band (4.5–5.8 keV) and a high energy band (9.5–15 keV). The power spectra were fitted with the sum of two Lorentzian profiles in addition to a power law with exponential cutoff. The Lorentzians are identified with two humps in the PSDs. It was found that the peak frequencies of the Lorentzians change and are strongly correlated with the photon index. There is also a correlation between the peak frequencies of both Lorentzians. The peak frequencies in the low energy PSD are almost identical to that in the high energy PSD, but there are significant differences between the two energy bands. The rms, which is related to the area under a Lorentzian profile, measures the contribution of the Lorentzian to the variability of the corresponding light curve. Whereas that of the Lorentzian L_2 located at high frequencies is identical in both energy bands, that of the first Lorentzian L_1 with a low peak frequency is larger in the low energy band than in the high one. Especially during the hard state this can be seen clearly. In the soft state only one hump remains in the PSDs, because L_2 decreases with increasing photon index. For that reason the assumption is justified, that the second hump in the power spectra is caused by frequencies originating from the corona. To compare the behavior of both energy bands further the coherence was introduced, which measures the degree of linear correlation between light curves in different energy bands. In addition a time lag between the light curves was analyzed. The light curve in the high energy band lags the one in the low energy band by a few milliseconds. Some possible reasons for this delay are Comptonization, geometrical reasons or an up-scattering process in a jet. But the behavior of the time lags is difficult to explain with these processes. During the hard state the lags increase continuously with increasing count rate in the low energy band and thus as well with Γ_1, whereas a different behavior is observed in the soft state. Here the lag drops to values of 2–3 ms at high count rates, while it is very large at low count rates. Obviously crucial changes in the emission process occur.

6.2 Outlook

In order to figure out if the correlations and transition parameters, which were found in this work, are generally valid for Cyg X-1, it is necessary to use more data. For example it would be very interesting to reproduce the hardness intensity diagram, which indicated the transition in this work, using all available PCA data of Cyg X-1. This would reveal if the transition always occurs at the same hardness. In addition there are much harder, but also much softer spectra available. For that reason such a hardness intensity diagram could be compared to the q-diagram (Fig. 2.10) allowing a more detailed classification of states. Color-coding such a diagram according to the time lags would simplify figuring out where changes in the underlying emission processes occur. Performing a timing analysis using all available PCA data is necessary in this case. This is in work at the moment at the Remeis observatory in Bamberg within the scope of another diploma thesis by Stefan Pirner. In his work the results and fit models of this work can be used. Combining the temporal with the spectral analysis of all available PCA data, it is possible to analyze how the PSDs change with the photon index Γ_1. Fig. 5.15 illustrated how the peak frequencies in the PSDs increase with increasing Γ_1 and how the second hump in the PSDs decreases. Here the photon index covered the range 2.0–2.6. Pottschmidt et al. (2003) used 4 Lorentzian profiles to fit PSDs of typical hard states as there were three clear humps in the power spectra. Therefore it would be interesting to see how this figure looks like at $\Gamma_1 < 2.0$ and for photon indices larger than 2.6 as well. Another important question is if the relation between Γ_1 and the peak frequencies is unvarying or it is time dependent. If it has changed since 1996, this could be an indication that temporary inhomogenities in the accretion disk cause the periodic modulations in the X-ray emission.

Good fits with a Comptonization model can be used to test if some of the resulting parameters are tied to the Lorentzian with a high peak frequency. This could reveal if the frequencies corresponding to this Lorentzian originate from a corona or not. Another interesting connection is that between peak frequencies, especially that of the Lorentzian with a low peak frequency and properties of the accretion disk. If the periodic oscillations are caused in the disk, parameters such as the inner disk radius should have a strong influence on the peak frequencies. To determine the inner disk radius more accurately better fits of spectra extending to lower energies are necessary. To obtain such data observations with other satellites are required.

Simultaneous observations with different satellites yield broadband spectra, which are very useful to figure out the physical mechanisms that cause the total emission covering electromagnetic waves from radio waves to γ-rays. Multiwavelength observations are necessary to test models that describe the total emission. Wilms, Nowak, et al. initiated a simultaneous observation with several satellites in April 2008. In total an energy range from 0.1 keV to about 2 MeV is covered. The data are currently analyzed.

The analysis of broadband spectra, especially with models covering the total range of frequencies, such as the jet model, combined with temporal and long-term analysis are essential to figure out the complex emission processes of X-ray binaries in detail, and probably that of AGN, too.

Bibliography

Abubekerov M.K., Antokhina E.A., Cherepashchuk A.M., 2004, Astronomy Reports 48, 550

Arnaud K., Dorman B., Gordon C., 2007, XSPEC Users Guide, HEASARC, NASA/GSFC `http://heasarc.gsfc.nasa.gov/docs/xanadu/xspec/`

Balbus S.A., Hawley J.F., 1998, Reviews of Modern Physics 70, 1

Begelman M.C., Blandford R.D., Rees M.J., 1984, Reviews of Modern Physics 56, 255

Benlloch S., Pottschmidt K., Wilms J., et al., 2004, In: Kaaret P., Lamb F.K., Swank J.H. (eds.) X-ray Timing 2003: Rossi and Beyond, Vol. 714. American Institute of Physics Conference Series, p.61

Bevington P.R., Robinson D.K., 1992, Data reduction and error analysis for the physical sciences, New York: McGraw-Hill, —c1992, 2nd ed.

Blandford R.D., Znajek R.L., 1977, MNRAS 179, 433

Bowyer S., Byram E.T., Chubb T.A., Friedman H., 1965, Sci 147, 394

Brocksopp C., Fender R.P., Larionov V., et al., 1999a, MNRAS 309, 1063

Brocksopp C., Tarasov A.E., Lyuty V.M., Roche P., 1999b, Astron. Astrophys. 343, 861

Cannon A.J., 1936, Annals of Harvard College Observatory 100, 1

Carvalho J.C., O'Dea C.P., 2002, ApJS 141, 371

Casella P., Belloni T., Stella L., 2005, Astrophys. J. 629, 403

Chandrasekhar S., 1931, MNRAS 91, 456

Charles P.A., Seward F.D., 1995, Exploring the X-ray universe, Cambridge, New York: Cambridge University Press

Coppi P.S., 1999, In: Poutanen J., Svensson R. (eds.) High Energy Processes in Accreting Black Holes, Vol. 161. Astronomical Society of the Pacific Conference Series, p. 375

Dotani T., Inoue H., Mitsuda K., et al., 1997, Astrophys. J. 485, L87

Dunn R.J.H., Fender R.P., Körding E.G., et al., 2008, MNRAS 387, 545

Fasano G., Vio R., 1988, Bulletin d'Information du Centre de Donnees Stellaires 35, 191

Fender R., 2002, In: Guthmann A.W., Georganopoulos M., Marcowith A., Manolakou K. (eds.) Relativistic Flows in Astrophysics, Vol. 589. Lecture Notes in Physics, Berlin Springer Verlag, p. 101

Fender R.P., Stirling A.M., Spencer R.E., et al., 2006, MNRAS 369, 603

Foellmi C., Petrucci P.O., Ferreira J., Henri G., 2008, ArXiv e-prints (arXiv:0810.0108)

Fragile P.C., 2008, ArXiv e-prints (arXiv:0810.0526)

Frank J., King A., Raine D., 1992, Cambridge Astrophysics Series 21

Gallo E., Fender R., Kaiser C., et al., 2005, Nature 436, 819

Ghez A.M., Salim S., Weinberg N., et al., 2008, In: IAU Symposium, Vol. 248. IAU Symposium, p.52

Giacconi R., Gursky H., Paolini F.R., Rossi B.B., 1962, Phys. Rev. Let. 9, 439

Gies D.R., Bolton C.T., 1986, Astrophys. J. 304, 371

Golian S.E., Krause E.H., Perlow G.J., 1946, Phys. Rev. 70, 223

Hanke M., 2007, *Master's thesis*, Dr. Remeis Observatory Bamberg, Germany

Hanke M., Wilms J., Nowak M.A., et al., 2008, ApJ in press (arXiv:0808.3771)

Hawley J.F., Krolik J.H., 2006, Astrophys. J. 641, 103

Heger A., Fryer C.L., Woosley S.E., et al., 2003, Astrophys. J. 591, 288

Herrero A., Kudritzki R.P., Gabler R., et al., 1995, Astron. Astrophys. 297, 556

Hjellming R.M., Wade C.M., 1971, Astrophys. J. 168, L21

Houck J.C., 2002, In: Branduardi-Raymont G. (ed.) High Resolution X-ray Spectroscopy with XMM-Newton and Chandra., `http://adsabs.harvard.edu/abs/2002hrxs.confE..17H`

Houck J.C., Denicola L.A., 2000, In: Manset N., Veillet C., Crabtree D. (eds.) Astronomical Data Analysis Software and Systems IX. ASP Conf. Ser. 216, p. 591

Hua X.M., Titarchuk L., 1995, Astrophys. J. 449, 188

Iben, Jr. I., Renzini A., 1983, ARA&A 21, 271

Jahoda K., Markwardt C.B., Radeva Y., et al., 2006, ApJS 163, 401

Jahoda K., Swank J.H., Giles A.B., et al., 1996, In: Siegmund O.H., Gummin M.A. (eds.) Proc. SPIE Vol. 2808, p. 59-70, EUV, X-Ray, and Gamma-Ray Instrumentation for Astronomy VII, Oswald H. Siegmund; Mark A. Gummin; Eds., Vol. 2808., p.59

Janksy K., 1933, Proc. IRE 21, 1387

Körding E., Falcke H., 2004, Astron. Astrophys. 414, 795

Kreykenbohm I., 2004, Ph.D. thesis, Eberhard-Karls-Universität Tübingen

Kylafis N.D., Papadakis I.E., Reig P., et al., 2008, Astron. Astrophys. 489, 481

Lachowicz P., Zdziarski A.A., Schwarzenberg-Czerny A., et al., 2006, MNRAS 368, 1025

Larwood J., 1998, MNRAS 299, L32

Levine A.M., Bradt H., Cui W., et al., 1996, Astrophys. J., Lett. 469, L33

Magdziarz P., Zdziarski A.A., 1995, MNRAS 273, 837

Maitra D., Markoff S., Brocksopp C., 2008, In: Bandyopadhyay R.M., Wachter S., Gelino D., Gelino C.R. (eds.) A Population Explosion: The Nature & Evolution of X-ray Binaries in Diverse Environments. American Institute of Physics Conference Series Vol. 1010, p.94

Makishima K., Maejima Y., Mitsuda K., et al., 1986, Astrophys. J. 308, 635

Markoff S., Nowak M.A., Wilms J., 2005, Astrophys. J. 635, 1203

McKinney J.C., 2006, MNRAS 368, 1561

Misra R., Zdziarski A.A., 2008, MNRAS 387, 915

Mitsuda K., Inoue H., Koyama K., et al., 1984, Publ. Astron. Soc. Jpn. 36, 741

Miyamoto S., Kimura K., Kitamoto S., et al., 1991, Astrophys. J. 383, 784

Ninkov Z., Walker G.A.H., Yang S., 1987, Astrophys. J. 321, 425

Nowak M.A., 2006, In: VI Microquasar Workshop: Microquasars and Beyond., PoS (MQW6) 001

Nowak M.A., Lehr D.E., 1998, In: Non-linear Phenomena in Accretion Disks around Black Holes., p.233

Nowak M.A., Vaughan B.A., Wilms J., et al., 1999a, Astrophys. J. 510, 874

Nowak M.A., Wilms J., Vaughan B.A., et al., 1999b, Astrophys. J. 515, 726

Pooley G.G., Fender R.P., 1997, MNRAS 292, 925

Pooley G.G., Fender R.P., Brocksopp C., 1999, MNRAS 302, L1

Pottschmidt K., 2002, Ph.D. thesis, Universität Tübingen

Pottschmidt K., Wilms J., Nowak M.A., et al., 2003, Astron. Astrophys. 407, 1039

Press W.H., Teukolsky S.A., Vetterling W.T., Flannery B.P., 1992, Numerical Recipes in C: The Art of Scientific Computing, Cambridge University Press, New York, NY, USA

Priedhorsky W.C., Terrell J., Holt S.S., 1983, Astrophys. J. 270, 233

Pringle J.E., 1981, ARA&A 19, 137

Roberts D.H., Wardle J.F.C., Lipnick S.L., et al., 2008, Astrophys. J. 676, 584

Rohlfs K., Wilson T.L., 2004, Tools of radio astronomy, Tools of radio astronomy, 4th rev. and enl. ed., by K. Rohlfs and T.L. Wilson. Berlin: Springer, 2004

Rothschild R.E., Blanco P.R., Gruber D.E., et al., 1998, Astrophys. J. 496, 538

Rybicki G.B., Lightman A.P., 1979, Radiative processes in astrophysics, New York, Wiley-Interscience, 1979. 393 p.

Schulz N.S., Cui W., Canizares C.R., et al., 2002, Astrophys. J. 565, 1141

Shakura N.I., Syunyaev R.A., 1973, Astron. Astrophys. 24, 337

Shapiro S.L., Teukolsky S.A., 1983, Black holes, white dwarfs, and neutron stars: The physics of compact objects, Research supported by the National Science Foundation. New York, Wiley-Interscience, 1983

Shaposhnikov N., Titarchuk L., 2007, Astrophys. J. 663, 445

Sunyaev R.A., Titarchuk L.G., 1985, Astron. Astrophys. 143, 374

Szostek A., Zdziarski A.A., 2007, MNRAS 375, 793

Thompson A.R., Moran J.M., Swenson, Jr. G.W., 2001, Interferometry and Synthesis in Radio Astronomy, 2nd Edition, Interferometry and synthesis in radio astronomy by A. Richard Thompson, James M. Moran, and George W. Swenson, Jr. 2nd ed.

Thorne K.S., 1974, Astrophys. J. 191, 507

Titarchuk L., 1994, Astrophys. J. 434, 570

Titarchuk L., Lyubarskij Y., 1995, Astrophys. J. 450, 876

Val-Baker A.K.F., Norton A.J., Negueruela I., 2007, In: di Salvo T., Israel G.L., Piersant L., Burderi L., Matt G., Tornambe A., Menna M.T. (eds.) The Multicolored Landscape of Compact Objects and Their Explosive Origins. American Institute of Physics Conference Series Vol. 924, p.530

van der Klis M., 1989, In: Ögelman H., van den Heuvel E.P.J. (eds.) Timing Neutron Stars., p. 27

Vaughan B.A., Nowak M.A., 1997, Astrophys. J., Lett. 474, L43

Webster B.L., Murdin P., 1972, Nature 235, 37

Wilms J., Nowak M.A., Pottschmidt K., et al., 2004, In: 35th COSPAR Scientific Assembly, Vol. 35. COSPAR, Plenary Meeting, p. 3810

Wilms J., Nowak M.A., Pottschmidt K., et al., 2006, Astron. Astrophys. 447, 245

Wilms J., Pottschmidt K., Pooley G.G., et al., 2007, Astrophys. J. 663, L97

Ziółkowski J., 2005, MNRAS 358, 851

Appendix

Online Material

Poster Results of this work were presented at the 7th Microquasar Workshop (1–5 September 2008) in Foça, Izmir Turkey. The presented poster can be found at: `http://www.sternwarte.uni-erlangen.de/~boeck/CygX-1/transition_CygX-1.pdf`

Movies An animated version of the hardness intensity diagram in Fig. 4.8 is available at: `http://www.sternwarte.uni-erlangen.de/~boeck/CygX-1/HID.avi` The time resolution of the data, which was used to create the movie, is 16s. In one frame 10 points in the HID are connected, in the next frame the last 5 of these 10 points are connected with the 5 following ones. The animation has 25 frames per second. Therefore 1 second in the movie corresponds to $16 \cdot 25 \cdot 5\,\mathrm{s} \approx 33\,\mathrm{min}$ in real time, if the gaps between the observations are not taken into account. There are also versions which are color-coded according to the time lags and the rms, respectively: `http://www.sternwarte.uni-erlangen.de/~boeck/CygX-1/HID_lags.avi` and `http://www.sternwarte.uni-erlangen.de/~boeck/CygX-1/HID_rms.avi`

Animated GIFs The temporal evolution of the time lags is animated:

- `http://www.sternwarte.uni-erlangen.de/~boeck/CygX-1/lag_lin.gif`
- `http://www.sternwarte.uni-erlangen.de/~boeck/CygX-1/lag_log.gif`

Here the total lag spectra are shown and the range from 3.2 to 10 Hz, over which the spectra are averaged to obtain a scalar value, is indicated by two vertical lines.

There are also several animations of the power spectra, which are very similar:

- `http://www.sternwarte.uni-erlangen.de/~boeck/CygX-1/data_time.gif` sequence of the PSD in both energy bands ordered by time
- `http://www.sternwarte.uni-erlangen.de/~boeck/CygX-1/time_low.gif` time-ordered sequence of the PSDs with the Lorentzian profiles in the low energy band
- `http://www.sternwarte.uni-erlangen.de/~boeck/CygX-1/time_high.gif` the same as above in the high energy band.

The following animations are ordered by Γ_1 instead of the time and thus correspond to a cutaway view through Fig. 5.15:

- `http://www.sternwarte.uni-erlangen.de/~boeck/CygX-1/low_all.gif`
- `http://www.sternwarte.uni-erlangen.de/~boeck/CygX-1/high_all.gif`

Online Data The fit parameters of the broken power law and the Comptonization model, which were obtained in this work, and that of the power spectra in both energy channels are available as FITS-files. Also are the values of the coherence and the time lags between different energy bands, including that between 4.5–5.8 and 9.5–15 keV.

- `http://www.sternwarte.uni-erlangen.de/~boeck/CygX-1/broken_pl.par`
- `http://www.sternwarte.uni-erlangen.de/~boeck/CygX-1/comptt.par`
- `http://www.sternwarte.uni-erlangen.de/~boeck/CygX-1/psd_low.par`
- `http://www.sternwarte.uni-erlangen.de/~boeck/CygX-1/psd_high.par`
- `http://www.sternwarte.uni-erlangen.de/~boeck/CygX-1/lag_coherence.fits`

List of Figures

Acknowledgements

To conclude I want to thank all those who supported me during the work on my diploma thesis. First of all I am very grateful to my advisor Jörn Wilms, who got me enthusiastic about the physics of black holes and X-ray astronomy and who gave me the opportunity to perform this work. I profited a lot from his knowledge. Despite his tight schedule he managed to maintain perfect support, was always willing to answer any question and helped at once if a problem occurred. Due to his friendly and approachable nature I liked to work under his guidance. He helped to establish contact to international scientists. Thanks to his efforts I could spend a week at the University of Amsterdam and I got the opportunity to present results of my work at the Microquasar Workshop in Foça (Izmir, Turkey).

I am much obliged to Manfred Hanke, with whom I shared an office. He introduced me in ISIS and the methods of analyzing data. I appreciate the programming, the Linux and the LaTeX tricks he explained to me. He was very helpful, always when I had a question he made a pause in his own work until the problem was solved. In addition the discussions with him contributed strongly to my understanding of astrophysics. Furthermore he and his green thumb provide an excellent office climate. Stefan Pirner, my second office colleague in the “Cygnus-room” was very helpful as well and discussed the computation of power spectra with me, among other things.

I want to thank Christian Schmid and Felix Fürst for proofreading the chapters of my thesis and giving useful comments and also for the fruitful discussions. Many thanks to Ingo Kreykenbohm for taking the time to answer my questions. The advice from Matthias Kadler was very helpful for me. I appreciate the discussions with Sonja Fritz about Comptonization fits and precessing accretion disks. Moreover I want to thank the entire team of the Dr. Remeis Sternwarte. Everybody contributed to the friendly and relaxed atmosphere at the observatory. I always enjoyed working there.

Concerning the timing analysis I am grateful for the collaboration with Victoria Grinberg. I yield many thanks to Katja Pottschmidt. With her experience in the analysis of Cygnus X-1 she was a great help for me, especially as far as the behavior of the time lags and the Lorentzian peak frequencies are concerned.

I really enjoyed the time I spent at the University of Amsterdam. I would like to thank the entire team of the Anton Pannekoek Institute, who made me feel welcome. Thanks to Sera Markoff I learned a lot during my visit. She took the time to explain the physics of jets and her jet model to me. In addition she gave me advice how to fit spectra with this model. Dipankar Maitra introduced me in the details of the model and helped to put it into operation on the computers in Erlangen.

I am grateful to the organizing committee of the Microquasar Workshop in Foça. I appreciate being allowed to present my work there. It was a great honor for me to come to know the scientists personally, whose names I already knew from the important papers.

Also I want to thank my fellow students, especially Matthias Aicher, Clemens Bauer, Melanie Pfeuffer and Christian Schmid. I could learn a lot from the conjoint discussions and had a lot of fun with them. Many thanks to my teachers, especially to the promoters of the “Elitestudiengang Physik”: Andreas Schäfer, Klaus Rith and Klaus Mecke. I owe a lot to them. Thanks to Christian Back I could spend an interesting lab course at the synchrotron in Trieste.

Neutron stars were not treated in this work, however I thank Stefanie Roth, Christian Grämer and the two project students Julia Schmid and Thomas Dauser for interesting discussions about these objects.

Last, but not least at all, I want to thank my family, on whose help I could always count on. My parents supported me not only financially, but also in all conceivable ways. It was always fruitful to apply to my brother for computer and scientific issues.

Hiermit erkläre ich, dass ich die Arbeit selbstständig angefertigt und keine anderen als die angegebenen Hilfsmittel verwendet habe.

Bamberg, den . . . .